

Evolution of Orogenic Blocking

by
Georg J. Mayr
Thomas B. McKee

Department of Atmospheric Science
Colorado State University
Fort Collins, Colorado

**Colorado
State
University**

**Department of
Atmospheric Science**

Paper No. 534

EVOLUTION OF OROGENIC BLOCKING

Georg J. Mayr

Thomas B. McKee

The research was supported by
the National Science Foundation under
grants #ATM-8713652 and #ATM-9113898.

Department of Atmospheric Science
Colorado State University
Fort Collins, CO 80523

March 1993

Atmospheric Science Paper # 534

EVOLUTION OF OROGENIC BLOCKING

Abstract

The evolution of low-level flow upstream of the Continental Divide (Rocky Mountains) from being blocked, i.e. unable to surmount the barrier, to becoming unblocked and blocked again is studied observationally and numerically. During two months in the winter of 1991/92 a transect of three wind profilers measured the wind field every few minutes. Three-dimensional numerical simulations with the Colorado State Regional Atmospheric Modeling System (RAMS) using realistic topography supplemented the observations with details of the blocked and unblocked flow.

The results confirm the theory that a mountain-induced mesoscale high above the upwind slopes causes the blocking. While previous research of idealized situations focused on changes of the cross-barrier wind and stability as determining variables to build that mesoscale high, this study found different mechanisms at work in the atmosphere.

The conceptual model proposed herein suggests that synoptic and radiative forcing drive the blocking evolution. An opposing synoptic cross-barrier pressure gradient can negate the mountain-induced mesoscale high. Therefore unblocking happens most frequently when the trough axis of a short wave is immediately upstream of the barrier, but synoptic pressure gradients caused by contrasts in vorticity and differential temperature advection on occasions are also strong enough to overpower the mesoscale pressure gradient. The flow returns to its blocked state when the ridge behind the trough approaches the barrier so that the synoptic cross-barrier pressure gradient reinforces the mesoscale gradient.

For a lower barrier or stronger solar insolation a well-mixed boundary layer can grow almost to the height of the barrier by afternoon and reconnect the blocked layer with the higher cross-barrier winds above the mountain. After sunset the radiative cooling stabilizes the lower atmosphere again and the transition back to the blocked state occurs.

The transition between the two states happened rapidly on the order of an hour with a minimum of 20 minutes and a maximum of four hours. A blocked flow event lasted on the average one and a half days but the duration varied widely from a few hours to eight days controlled by the synoptic situation. The depth of the blocked layer even during one blocking episode fluctuated considerably but never exceeded the height of the barrier.

The profiler approximately one radius of deformation upstream of the barrier observed the least amount of blocking. Numerical simulations confirmed that the Coriolis force limits the upstream extent of the layer deflected around the barrier to about that distance. The flow in the simulations was deflected northward and channeled with high speeds through a gap in southern Wyoming, which is known as one of the windiest places in the United States.

Acknowledgments

Vielen Dank and thanks to

Drs Steve Cox, Roger Pielke, and Bill Massman for helpful discussions,
Dr. Gene Wooldridge for many discussions and help with the field work,
John Kleist for his indispensable help with computers, programming and field work,
Dr. Paul Wolyn for his knowledge of RAMS and providing lots of his specially developed code and help with the field measurements,
Jeff Copeland for further assistance with RAMS,
Nolan Doesken for his immense knowledge of the Colorado Climate and participation in field measurements,
Odie Bliss for help with the editing the final version of this paper, lots and lots of help with word processing, conference and field work arrangements and for making the Colorado Climate Center such a great place to work at,
Judy Sorbie-Dunn for drafting the figures in chapter seven,
Clark King, Dr. Bill Neff, and Dan Wolff from NOAA's Wave Propagation Laboratory for loaning us a 915 MHz wind profiler and installing it in Tabernash,
the support staff of the CSU profiler: Chris Cornwall, Dr. John Davis, Paul Hein, and Dave Wood for their tremendous help in becoming familiar with the profiler and putting it in Meeker,
Dr. Al Astling for making the wind profiler data from Dugway Proving Ground available to us,
all the people helping with field work in snow and cold: Dr. Dave Changnon, Jon Cornick, Keith Foreman, Jimmy Keener, Steve London, and Matt Savoie,
the Golf Club in Tabernash and the Plant Center in Meeker for letting us use their property to set up the profilers and Garry Noler for his support,
and the National Science Foundation for providing financial support with grants ATM-8713652 and ATM-9113898.

Georg Mayr would like to extend a special thanks to his families and especially his wife, Lorena for their patience, encouragement and support without which he could not have finished this research. Thank you very much!

Table of Contents

1. Introduction	1
2. Literature review	5
2.1 Observations of blocking	5
2.1.1 Nature of flow deflection and stagnation at various mountain ranges	5
2.1.2 Momentum balance in blocked flow	6
2.1.3 Determination of blocking	7
2.1.4 Climatology	8
2.2 Theoretical analyses	8
2.3 Numerical simulations	11
2.4 Laboratory simulations	13
2.4.1 Two-dimensional obstacles	13
2.4.2 Three-dimensional obstacles	13
2.5 Summary	13
3. Data	15
3.1 Design of observational and modeling study	15
3.1.1 Design of the observational study	15
3.1.2 Purpose of the modeling study	17
3.1.3 Observational equipment and location	17
3.2 Principles of wind profilers and RASS (radio acoustic sounding system)	20
3.3 Quality control	22
3.3.1 SOP radiosoundings	22
3.3.2 NWS rawinsoundings	22
3.3.3 profiler winds	22
3.3.3.1 Error sources and remedies	22
3.3.3.2 quality control algorithms	23
3.3.4 RASS	25
3.4 Examples of wind profiler measurements	25
4. Local determination of blocking	28
4.1 Trajectories	28
4.2 Vertical profile of cross-barrier wind U	28
4.3 Vertical integral of cross-barrier massflux (CBMF)	28
4.4 Vertical integral of cross-barrier kinetic energy flux (CBEF)	29

4.5 Conserved variable diagram	29
4.6 Froude number	29
4.7 Contours of U/N	30
4.8 Intercomparison	30
4.9 Method used in this study	32
5. Observational results	33
5.1 Blocked periods	33
5.1.1 Determination of blocked flow	33
5.1.2 Statistics	33
5.1.3 Blocking depth	34
5.1.4 Transition between blocked and unblocked states	36
5.2 Vertical structure of horizontal wind field	38
5.2.1 Scatterplots	41
5.2.1.1 Tabernash	41
5.2.1.2 Meeker	42
5.2.1.3 Dugway	44
5.2.2 Wind matrices	44
5.2.2.1 Tabernash	46
5.2.2.2 Meeker	48
5.2.2.3 Dugway	50
6. Modeling results	59
6.1 Model description	59
6.1.1 Model domain and topography	59
6.1.2 Model initialization	61
6.2 The role of Coriolis force	61
6.2.1 Non-rotating system	61
6.2.1 Rotating system	63
6.3 The role of wind speed and stability	72
6.4 The role of initial wind direction	77
6.5 Summary	79
7. How is blocking formed and destroyed or: towards a conceptual model of blocking	82
7.1 Synoptic forcing	82
7.2 Radiative forcing	86
7.3 Classification of blocking events during the observational period	87
7.3.1 Unblocking	87
7.3.2 Blocking	90
7.4 Conceptual model of blocking evolution	92

7.4.1 Synoptically driven blocking evolution	92
7.4.2 Radiatively driven blocking evolution	93
8. Case studies	97
8.1 Synoptically driven blocking evolution	97
8.2 Radiatively driven blocking evolution	99
9. Summary	106
9.1 Conclusions	106
9.2 Future research	107
Appendix A	108
References	109

When a stream comes to some stones in its path,
it doesn't struggle to remove them,
or fight against them,
or *think* about them.
It just goes around them.
Water responds to What's There with
effortless action.
(Hoff: *The Te of Piglet*)

The Cartesian paradigm was based on the belief
that scientific knowledge could achieve
absolute and final certainty.

In the new paradigm, it is recognized
that all concepts, theories and findings
are limited and approximate.
(Capra and Steindl-Rast: *Belonging to the Universe*)

1

Introduction

A river might not *think* what it will do when it encounters an obstacle in its path nor will air approaching a mountain but atmospheric scientists have given that question a great deal of thought. Will the air flow over the obstacle, go around or become stagnant? For three decades Sheppard's (1956) answer that that will depend on whether an air parcel possessed enough kinetic energy to overcome the potential energy difference between its elevation and mountaintop, dominated the community's thinking especially since experiments and observations seemed to confirm his argument. Smith (1988) showed that that agreement was only "accidental" and the answer depends on how much denser (relative to far upstream) air is piled up at and above the upstream slope of the mountain thus producing a mesoscale high.

Air parcels encountering a small hill will diverge around it (Fig. 1.1a) but the center trajectory is still able to climb above the hill. For larger hills a stagnation point of the parcel trajectory can under certain conditions develop on the windward slope and the flow will split into two directions with the possibility of air recirculating before it flows laterally around the obstacle (Fig. 1.1b). The latter phenomenon is referred to as flow-splitting or blocking. For the rest of this study the word "blocked" will be used to describe a situation where air everywhere along the obstacle below a certain level, the so-called "dividing streamline", cannot surmount the obstacle but rather passes around it or becomes entangled in local recirculations. The depth of the blocked layer may vary depending on atmospheric conditions and shape of the obstacle. "Unblocked", on the other hand refers to a situation when - at least somewhere along the barrier - air can climb the mountain all the way. "Blocking" and "unblocking" refer then to a transition to and out of that state, respectively.

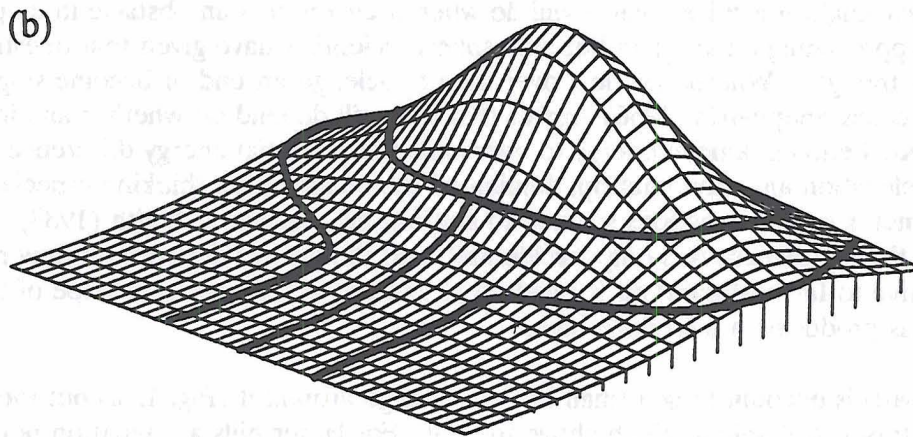
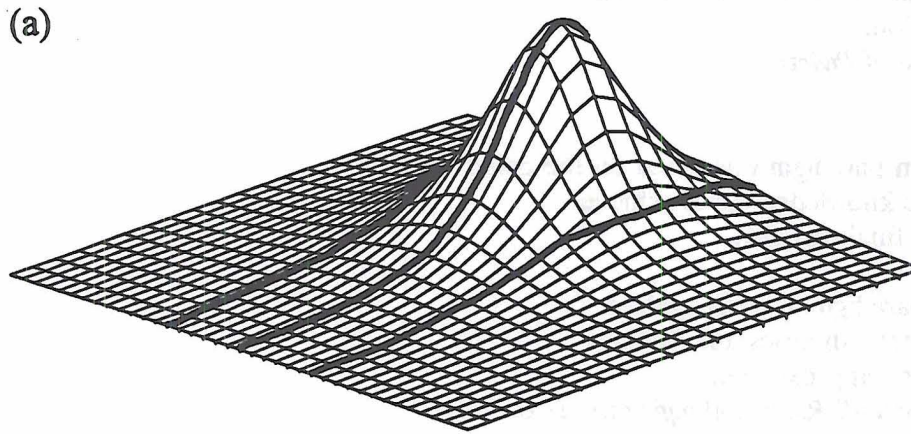


Fig. 1.1: Sketch of (a) unblocked and (b) blocked flow. The situation in (b) is also referred to as "flow splitting". Only streamlines whose far-upstream origin is near the surface are shown. Possible recirculating flows are not shown.

For the last decade researchers have tried to identify parameters controlling the behavior of the atmosphere in the presence of an obstacle. Smith (1989a) and Baines (1987) review that quest and its results. For uniform Boussinesq flow with a cross-barrier wind component U and constant buoyancy frequency N without friction and rotation the Froude number,

$$F = \frac{U}{Nh} \quad (1.1)$$

where h is the relative height of the obstacle, is the controlling parameter. The buoyancy frequency is defined as

$$N = \left(\frac{g}{\theta} \frac{\partial \theta}{\partial z} \right)^{1/2} \quad (1.2)$$

where g is the gravitational acceleration, θ the potential temperature, and z height. With rotation the Burger number B

$$B = \frac{Ro}{F} = \frac{Nh}{fL} \quad (1.3)$$

replaces the Froude number. The Rossby number, Ro , is defined as

$$Ro = \frac{U}{fL} \quad (1.4)$$

where f is the Coriolis parameter and L the halfwidth of the obstacle. With rotation the cross-barrier component no longer explicitly influences the behavior of the flow, which depends only on the stability of the air and the shape of the obstacle.

For sheared far-upstream flow the Richardson number

$$Ri = \frac{N^2}{\left(\frac{\partial U}{\partial z} \right)^2} \quad (1.5)$$

also controls the behavior of the atmosphere and in real situations friction is important, too.

While research efforts have focused mainly on theoretical analysis and numerical and laboratory simulations to identify the controlling parameters, observations have lagged far behind probably because they require more resources and the real-world conditions are not amenable to extracting the essence of the flow's behavior: the barriers are of complex shape, the flow rarely reaches a steady state, and other phenomena can mask the mountain-induced response.

Peppler (1928) examined measurements taken during hot air balloon ascents on the German side of Lake Constance during deep northerly flow (i.e. perpendicular to the Alps) and found a highly stable atmosphere below mountaintop and winds that were much weaker than farther upstream. New evidence of the upstream influence of the Alps surfaced during the Alpine Experiment (ALPEX) in the early eighties. Chen and Smith

(1987) and Binder et al. (1989), for example, observed the deflection of the flow around the Alps by examining data from a dense network of surface stations and six-hourly rawinsoundings, respectively.

Observational, theoretical, numerical and laboratory studies so far have only dealt with causes for blocking of low-level air by mountains but not attempted to explore the evolution of blocking, the whole cycle from an unblocked through a blocked state back to an unblocked one. How long does it take for the atmosphere to switch from one state to the other, how long are the blocked periods, how frequent is blocking, and what are the causes for un/blocking in the real atmosphere? These were the questions to be asked after looking at a climatology of thirty years of bidaily rawinsonde data from the Great Basin on the North American Continent and finding from a simple Froude number criterium that this area seems to be blocked frequently during the winter months.

While uncovering the answer to the above questions would have been impossible fifteen years ago, the advent of new observational instruments, especially the wind profiler, which allows nearly continuous measurement of the wind field, provides the atmospheric scientist with the observational power to tackle these questions.

This study presents the answers determined from observing the wind field with a transect of three profilers upstream of the Continental Divide in Colorado and Utah and from numerical simulations using the Colorado State RAMS (Regional Atmospheric Modeling System).

The area west of the Continental Divide has one of the largest oil shale reserves in the world. Since the extraction of the oil produces a lot of pollutants frequent blocking of the low-level air will then lead to high pollution.

Frequent blocking during winter also explains the high number of days with calm or light winds that are observed on the Western Slope. Additionally the formation of a blocked layer of air above the snow-covered surface that cools strongly explains in part why in winter temperatures west of the Continental Divide are lower than on the east side thus increasing the heating expenses.

The paper is organized as follows: Chapter two places the study within the previous body of knowledge. In chapter three the measurement campaign, observational instruments and methods, and the quality control of the data are described. Chapter four compares different methods to determine from a vertical sounding at one point whether the low-level flow is blocked or not. Chapter five includes an analysis of the observational results in more detail. What are the preferred wind directions for blocking to occur, how long and how deeply does the atmosphere become blocked? Chapter six seeks a more complete physical understanding of the observations from numerical simulations of the three-dimensional flow in the region upstream of the Continental Divide, especially what role rotation, stability, wind speed and direction and certain orographic features play. Chapter seven deals with the mechanisms that led to blocking and unblocking during the observational period and develops a conceptual model of the two archetypical blocking and unblocking mechanisms. Chapter eight shows wind profiler and synoptic data for three case studies. And the last chapter summarizes the findings about the evolution of blocking upstream of the Continental Divide during winter.

2

Literature review

In this chapter previous work is reviewed on the blocking and deflection of air by mountains. Since questions usually come before answers observations of upstream flow deflection and stagnation will be examined in section 2.1, then theoretical explanations (section 2.2) will be evaluated and finally numerical (section 2.3) and laboratory (section 2.4) simulations will be compared with the observational and theoretical results.

2.1 Observations of blocking

2.1.1 Nature of flow deflection and stagnation at various mountain ranges

Peppler (1928) reported one of the first thorough observations of upstream flow stagnation. He examined data from 119 hot air balloon ascents on the German side of Lake Constance during deep (up to 5000 m ASL) northerly (i.e. perpendicular to the Alps) flow during the years 1910 - 1925. The northerly flow originated mostly from anticyclones and brought very stable arctic air towards the Alps. The wind below mountaintop was very weak and frequently calm, a fact that Peppler correctly attributed to the weakening of the synoptic scale pressure gradient by adiabatic cooling of air during its orographically forced ascent. The slowdown of the impinging air affected also mountaintop stations, where the wind speed was considerably lower than farther upstream over the foreland, but the wind directions were similar thus not indicating any high-reaching flow deflection along the Alps. Surprisingly Peppler reported no deflected or return flow in lower levels either. Temperatures at mountain-top as contrasted with temperatures at the same elevation over the foreland were on the average only -0.16 K colder, so that the air reaching mountaintop could not have adiabatically ascended all the way from the foot of the mountain, in which case the difference would have been much bigger. Peppler frequently found temperature inversions (top of the cold dome) slightly below crest height so that the air at mountaintop would have been lifted only slightly.

More than half a century later the Alpine Experiment (ALPEX) provided a much higher spatial and somewhat higher temporal density of soundings. Binder et al. (1989) found from wind roses at the mandatory pressure levels during the two month long special observation period what had eluded Peppler: a penchant for flow-splitting. The deflected air extended less than 2 km vertically and between 200 and 300 km north of the barrier. They found large values of anticyclonic vorticity in the air above the deflected flow due to the lifting over the mountain.

The Alps are not the only mountain range on earth where blocking of low-level air has been documented. Skillful analysis of the few available data allowed Schwerdtfeger (1975) to attribute the strong along-barrier winds on the east side of the mountainous Antarctic Peninsula to blocking of cold easterly flow from the Weddell Sea to the east of the mountains. He argued that the adiabatic cooling of the orographically lifted air forms a cold dome near the mountain, which in turn causes a mountain-parallel thermal wind so that the flow deflects to the north. Surface friction assists that turning.

Similar barrier winds occur along the Sierra Nevada on North America's Pacific Coast. Aircraft observations detected barrier jets between 15 and 30 m/s that extended more than 100 km upwind of the barrier (Parish, 1981).

Farther north, on the east side of the Alaskan Peninsula, Lackmann and Overland (1989) found also along-barrier winds in the presence of synoptic northeasterly flow.

Mass and Ferber (1990) reported results from a network of eleven microbarographs around the Olympic Mountains in Washington, an isolated, ca. 1800 m high topographic feature. The excess pressure on the windward slope was on the order of one hPa and correlated best with incoming wind speed and not as well with the Froude number computed from an upwind radiosounding.

Blocking by the Appalachians usually occurs when cold air from the anticyclone behind a trough, whose axis is located over central New York, flows southward near the surface along the eastern side of the Appalachians and another upper level trough is located over Alabama. Then the surface low associated with the southern trough enhances the north-south pressure gradient and at the same time steers the shallow cold air from the northern anticyclone towards the mountains. This air forms a cold dome and flow is deflected along the mountains through the ridging within the dome (Bell and Bosart, 1988). A U-shaped ridge (trough) in the sea level pressure (temperature) pattern identifies the presence of such a cold dome.

The eastern Foothills of the Rocky Mountains also cause damming of cold air. Since such events can produce heavy snowfall, they have been studied intensely, a task that has been aided by a dense surface observation network in that area (PROFS). Typically the flow up to at least 700 hPa has a strong easterly component towards the Foothills and cold advection and adiabatic cooling due to lifting produce a shallow cold pool with mountain-parallel flow. Moist mid-level flow glides over the top of the cold pool and together with higher-level southwesterly flow triggers heavy snow falls (Wesley, 1991). Marwitz and Toth (1993) found latent heat release from melting precipitation to rapidly intensify the barrier jet.

Mayr and McKee (1990) used the Froude number computed from 30 years of bidaily rawinsoundings in Grand Junction, CO, and Salt Lake City, UT, to examine the frequency of blocking on the upwind side of the Rocky Mountains. The results were similar for both stations: the morning soundings (05 MST = 12 UTC) showed little seasonal variation of the blocking frequency whereas the maximum frequency of blocked events in the evening soundings (17 MST) occurred from November through February and the minimum in June.

2.1.2 Momentum balance in blocked flow

What are the dominating forces in flow that is deflected along a barrier? Very few researchers have tried to answer that question from observations.

Bell and Bosart (1988) computed a momentum budget from an analysis of rawinsoundings and surface observations for the evolution of a cold air damming event in the Appalachians. As the air is synoptically forced against the mountains adiabatic and evaporative cooling contribute each approximately a third of the total cooling within the forming cold dome. The presence of the mountains decelerated the flow so that it no longer was in geostrophic balance with the large scale pressure gradient force and an ageostrophic mountain-parallel flow developed. The Coriolis force acting on that flow

tried to force it towards the mountains adding to the mesoscale high caused by adiabatic and evaporative cooling. Finally the cross-barrier momentum budget consisted of geostrophic balance between the *mesoscale* pressure gradient and the Coriolis force on the along-mountain flow while in the along-mountain budget the *synoptic scale* pressure gradient force balanced the frictional force. At the top of the cold dome they observed a strong directional and speed shear.

Lackmann and Overland (1989) computed along- and cross-barrier momentum budgets in the Shelikof Strait east of the Alaskan Peninsula from aircraft measurements for a case with along-barrier wind. The along-barrier acceleration was up to 55% of the limit imposed by the ageostrophic (relative to the synoptic scale) pressure gradient with surface friction and entrainment at the top of the boundary layer retarding the flow. The mesoscale pressure gradient force caused by the adiabatic cooling due to the forced ascent over the barrier slopes and Coriolis force acting on the along-barrier flow roughly canceled out, i.e. the cross-barrier momentum budget was geostrophically balanced.

2.1.3 Determination of blocking

From the spatially and temporally coarse measurements routinely available it is not easy to determine whether a barrier blocks low-level air or not and several methods have been used, which will be reviewed in this section.

Binder et al. (1989) determined blocked low-level air for individual stations based on the Froude number, F , defined in (1.1). The ratio U/N has dimensions of length and can be conceived as a measure of the height an air parcel can be raised in an ambient uniformly stratified environment by transforming its kinetic completely into potential energy. They classified the parts of a time-height cross section of U/N and the wind vector as blocked when- and wherever the height of the mountain, h , was higher than U/N and the wind was weak. Nonlinear two-dimensional numerical simulations (see section 2.2) and laboratory simulations (see section 2.4.2) confirmed the validity of this method. In non-dimensional form (normalized by h) this method predicts a blocked layer of depth $1 - F$ whenever F is less than 1. Due to the decoupling between the blocked layer and the flow above, the vertical profile of the wind vector marked the top of the blocked with strong shear.

Aircraft observations of gravity waves above the Antarctica (Bacmeister et al., 1990) could only be reproduced by a linear three-dimensional model after blocking of low-level air had been accounted for by artificially filling up the terrain so that U/N exceeds the new barrier heights anywhere in the modeling domain, which is not conclusive but at least circumstantial evidence for the validity of this method to determine local blocking depth.

Other investigators used different methods to determine whether the flow was blocked or not, and sometimes reached contradictory conclusions. Chen and Smith (1987) computed trajectories on a material surface immediately above the boundary layer, whose pressure field they assumed to be identical to the surface pressure field reduced to sea level. Consequently they could exploit the much higher spatial and temporal resolution of the surface pressure observations compared with upper air soundings. However, their method classified a period of a frontal passage along the Alps on April 29, 1982 as blocked whereas Binder et al. (1989) diagnosed it as unblocked. Since surface pressure observations are strongly influenced by the structure of the boundary layer the pressure

field on a material surface above the boundary layer need not necessarily be similar. In addition the low wind speeds at low levels during blocked situations are not amenable to trajectory calculations.

Steinacker (1984) used trajectories along isentropic surfaces to show the deflection of the air around the Alps during ALPEX. While his analysis did not suffer from the assumption about the pressure pattern as in Chen and Smith's method, the lower spatial and temporal (6-12 hours) resolution aggravated the problem caused by low wind speeds during blocked situations.

2.1.4 Climatology

Climatologies of orographic blocking of low-level air exist for the Alps, the Appalachians and the Rocky Mountains. The shortest climatology comprises just the two months during the special observation period of ALPEX from March through April 1982 (Binder et al., 1989). While they did not provide the number of blocked events for that period, wind roses and scattergrams of wind direction at the mandatory levels showed a predilection of flow deflection around the Alps.

Using contingency tables derived from five years worth of rawinsoundings in Payerne in the Swiss Alps, Furger (1992) found a preferred veering of the wind with height indicative of the deflection by the Alps. However, he did not try to identify the individual blocked events and list their frequencies.

Bell and Bosart (1988) examined 50 years of surface maps for the presence of pressure troughs and thermal ridges east of the Appalachians, which is the signal of cold air damming there (see section 2.1.1). They found cold air damming by the southern Appalachians to occur year-round with the highest frequency, intensity and duration of damming events in winter from December through March. The minimum (in frequency and intensity) is in July.

2.2 Theoretical analyses

While there has been great improvement in the theoretical treatment of orographic upstream flow deflections especially over the past two decades the evolution will not be retraced but rather the results of the current theoretical understanding presented with one exception: despite his own cautioning about "an extreme oversimplification" Sheppard's (1956) explanation of airflow speed variations exclusively in terms of their kinetic and potential energy (like the mechanical analogue of a ball rolling up a hill) dominated the minds of many atmospheric scientists until very recently and was convincingly disproved only lately by Smith (1988; 1989b). Both researchers started with the Bernoulli equation for a streamline in steady, inviscid, Boussinesq flow coinciding with a line of constant density $\rho = \rho_0$ as given in (2.1).

$$U_0^2 = U^2 + N^2 \eta^2 + \frac{2}{\rho_0} p^* \quad (2.1)$$

The subscript 0 denotes far-upstream values, η the displacement of the streamline from its far-upstream height, and p^* the deviation of pressure at each point on the streamline from its value far upstream. While Sheppard neglected the pressure term (the last term on the right side of (2.1)) Smith found it to be of the same magnitude as the other terms and expressed it - using the hydrostatic assumption - through the integral of the displacements

$$I_\eta = \int_{z_0}^{\bar{z}} \eta dz_0 \quad (2.2)$$

as

$$p^* = \rho_0 N^2 \left(I_\eta - \frac{\eta^2}{2} \right) \quad (2.3)$$

Thus the potential energy terms (the ones involving η^2) cancel between (2.1) and (2.3):

$$U_0^2 = U^2 + 2N^2 I_\eta \quad (2.4)$$

Therefore the excess pressure at a point on the streamline in the vicinity of the mountain compared with far upstream determines the behavior of the flow for a given U_0 and N . Stagnation ($U = 0$) occurs where

$$I_\eta = \frac{U_0^2}{2N^2} \quad (2.5)$$

As a consequence of the condition that wave energy has to propagate away from its source, i.e. the obstacle, the crests of the streamlines tilt upstream. Therefore the upwind slope has the strongest region of positive displacement and stagnation on the lower boundary begins there. As the streamlines lift over the mountain air cools adiabatically and - depending on the vertical pattern of the streamlines - denser air piles up above the upwind slope and produces that mesoscale high.

Smith computed the vertical displacement integral for linear flow in isosteric (constant specific volume) coordinates for ellipsoidal obstacles (Smith, 1988) assuming the flow was hydrostatic, Boussinesq, inviscid and incompressible. The regime diagram in Fig. 2.1 best summarizes the results:

- For constant upstream speed and stability and cross-flow dimension of the obstacle being larger than the flow-parallel one (aspect ratio > 1) stagnation begins aloft (curve A is below curve B), whereas for an aspect ratio smaller than one the stagnation occurs on the windward slope.
- With the presence of shear an additional parameter, the Richardson number, controls the behavior of the flow. In the case of forward shear the windspeed aloft, where flow stagnation occurred first in the unsheared case, is now higher and therefore the displacement integral, I_η , needs to be bigger for the flow to stagnate there. Hence in a sheared flow of reasonable Richardson number (less than 20) stagnation will always occur first on the upwind slope (curve B is below curve A for $Ri < 20$ in Fig. 2.1 for all aspect ratios).

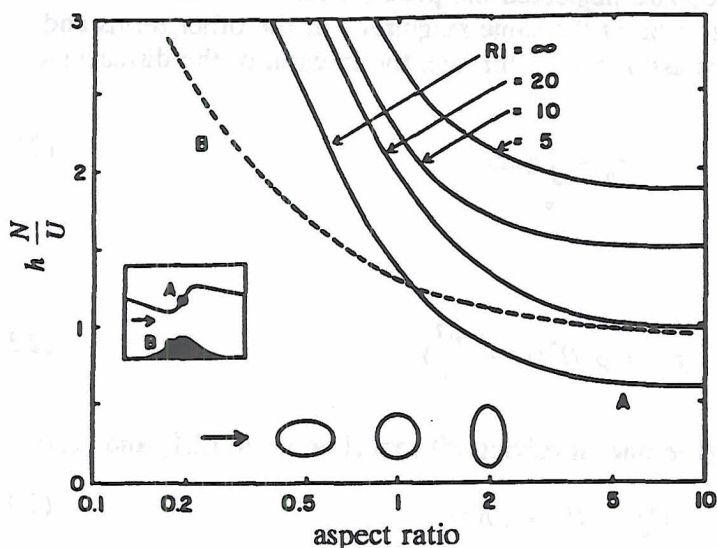


FIG. 2.1: Regime diagram for the flow of incompressible, inviscid, Boussinesq, and non-rotating fluid over ellipsoidal hills as a function of nondimensional mountain-height and horizontal aspect ratio of the obstacle (adapted from Smith, 1989b). The mountain height h is normalized by buoyancy frequency N over cross-barrier speed U . The shape of the hill is shown for aspect ratios of 0.5, 1, and 2. Stagnation occurs first on the upwind slope when curve B is below curve A. With shear ($Ri < 20$) flow stagnates first at the upwind slope independent of aspect ratio.

Smith (1985) incorporated wave breaking into a local hydraulic model and found solutions only when U/N exceeded the barrier height and speculated on an effective modification of the obstacle to that limit by the formation of blocked air upstream of the obstacle. His hypothesis agrees both with observations (section 2.1), numerical (section 2.3) and laboratory simulations (section 2.4).

Pierrehumbert and Wyman (1985) performed an in-depth scale analysis of a rotating, inviscid, and incompressible flow with constant stability and speed far upstream over an infinite ridge. With the addition of rotation the Rossby number, Ro , enters as a controlling parameter. For small Rossby numbers the mountain-parallel flow adjusts to geostrophic balance after an adjustment time of $O(Ro)$, just as observed by Bell and Bosart (1988) and Lackmann and Overland (1989) (compare section 2.1.2), and semigeostrophic theory becomes valid. The deceleration of the impinging flow is between $O(Ro/F)$ for small mountains and $O[(Ro/F)^2]$ for high mountains so that whenever $Ro/F \geq O(1)$ the flow near the mountain greatly deviates from its far upstream characteristics but is nearly undisturbed by the mountain if $Ro/F \ll 1$. During the initial adjustment the flow deceleration scales similar to the balanced state even though the adjustment is ageostrophic.

For large Rossby numbers the deceleration scales like $O(1/F)$ for small mountains and $O(1/F^2)$ for tall mountains - at least initially since given enough distance over which to act terms of $O(1/Ro)$, which have been neglected in the scaling, can become important and the resulting flow never might become steady.

Xu (1990) showed that only the inclusion of friction can make the mountain-parallel flow steady in such a situation. He formulated a two-layer, hydrostatic, viscous, rotating two-dimensional model for an infinitely long mountain to study the Appalachian cold air damming theoretically. In his analysis he also included a mountain-parallel far-upstream geostrophic flow which in addition to Rossby and Froude number controlled the

flow behavior and the shape of the cold dome that formed on the mountain slope. Friction, though necessary to balance the along-mountain geostrophic pressure gradient force, exerted weaker control over the flow than the other three parameters.

2.3 Numerical simulations

Several authors attempted to alleviate the restriction of linearity found in many theoretical treatments of upstream influence by numerical simulation while still focusing on the essentials of the flow behavior by using hydrostatic, inviscid or non-rotating constraints.

A prime example is Pierrehumbert and Wyman (1985). Besides the scale analysis discussed in section 2.2 they ran a two-dimensional, dry and hydrostatic primitive equation model with a vertical diffusion parameterization to be able to realistically incorporate wave breaking. Gravity waves could radiate through the lateral and top boundaries. For the non-rotating case they found wave breaking and excitation of upstream influence at a Froude number of $4/3$. Air began to stagnate near the obstacle if the Froude number was decreased to $2/3$ and for Froude numbers below $1/2$ the stagnant region travelled infinitely far upstream. The critical Froude number for the onset of blocking depended on the mountain shape: for a Gaussian shape it was $2/3$ but $4/7$ for a bell shape.

Wave breaking excited non-dispersive gravity waves of zero horizontal wavelength, which are termed "columnar disturbances", that propagate horizontally away from the source without losing energy to $z = \infty$. Upstream propagation occurred only when the mountain could excite vertical waves of considerable amplitude and lengths between zero and U/N . They also speculated that the stagnant air upstream of the barrier forms as an "orographic adjustment" so that the obstacle appears to the impinging air to have only a nondimensional height Nd/U of 1.5 for the Gaussian-shaped infinitely long mountain, where d is the dimensional thickness of the unblocked air below crest height.

Adding rotation arrested the upstream propagation of the stagnant layer at a distance of one radius of deformation,

$$L_R = \frac{Nh}{f} \quad (2.6)$$

The slowdown of the impinging flow leaves the large scale along-mountain pressure gradient unbalanced, which makes the along-barrier flow component positive, which in turn creates a Coriolis force in the cross-barrier direction trying to accelerate the cross-barrier component back to geostrophy. In the ageostrophic limit ($Ro > 1$) a steady state was never reached because of the absence of friction. Semigeostrophic theory and the model simulations agreed well for $Ro < 1$, in which case a steady state was reached when the decelerated layer had retreated from its maximum extent of L_R to $(L L_R)^{1/2}$, where L is the mountain halfwidth.

Bacmeister and Pierrehumbert (1988) investigated the effects of a non-uniform wind with height. Their wind profile had a critical level (zero wind speed) and a flow reversal above mountaintop. When the critical level was close to mountaintop a strong upstream surge formed that drastically decelerated the low-level flow and lifted the critical

level. Stagnation of low-level air with such an initial wind profile occurred for a Froude number (based on low-level far-upstream wind speed) twice the critical Froude number for uniform flow ($4/3$ instead of $2/3$).

Smolarkiewicz and Rotunno (1990) extended Pierrehumbert's and Wyman's inviscid, non-rotating simulations to three dimensions for bell-shaped obstacles. The results depended greatly on the horizontal aspect ratio, r (along-stream over cross-stream dimension) of the barrier. Only for $r > 1$ did they find flow reversal in the lower layers. In that case two singular points were present on the upwind slope: the first one near the top of the obstacle was a nodal or attachment point from which the flow emanated. Snyder et al. (1985) called it the "height of dividing streamline". Below this point incoming air flowed down the upwind slope as far as the saddle point before flowing laterally around the mountain. The second singular point was a saddle or separation point at the upstream base of the obstacle towards which the flow converged. With increasing Froude number the saddle point moved farther towards the mountain, which is contrary to laboratory results by Castro et al. (1983). These laboratory simulations, however, had a frictional boundary layer of a depth comparable to the obstacle height. Smolarkiewicz and Rotunno therefore conjectured that inviscid effects and in particular wave breaking over the lower upwind side dominate the flow behavior for taller mountains.

As the aspect ratio increased ($r > 4$) horizontally oriented vortices besides the one at the saddle point appeared. The amplitude and area of flow reversal pulsated possibly due to the constant building and breaking of the wave over the mountain, which kept the flow from ever attaining a steady state.

Pierrehumbert and Wyman (1985) found upstream propagating columnar disturbances to cause the flow stagnation for $r \rightarrow \infty$. Columnar modes were absent, however, in Smolarkiewicz and Rotunno's simulations for an aspect ratio $r = 1$ and the flow stagnation was caused by the piling up of denser air on the upwind side. However, as the aspect ratio increased, columnar modes were the second mechanism contributing to the stagnation.

Linear theory (Smith, 1988, as discussed in section 2.2) predicts the onset of stagnation especially well for $r \leq 1$, even though it underestimates the slow-down and becomes invalid after onset of stagnation. This agreement of linear theory with the nonlinear simulation confirms the correctness of identifying the piling-up of denser air as the cause of blocking.

Neither of the above numerical simulations studied the effects of thermal forcing on blocking. Bossert (1990) simulated thermally forced circulations over the Great Basin during summer season. With the high solar insolation and sensible heat fluxes during daytime in that area a mixed boundary layer comparable with the depth of the mountains builds so that the Froude number approaches infinity and no blocking occurs. During nighttime radiative cooling of the slopes produces a current down the upwind slope (see also Bader and McKee, 1992), which could increase the strength and amplitude of flow reversal induced by dynamic mechanisms.

Lee et al. (1989) simulated the effects of a stagnant shallow cold pool east of the Rocky Mountains on severe (westerly) downslope windstorms. Neither turbulent mixing by the westerlies on top of the cold pool nor a forced mountain wave could efficiently erode the stagnant air mass. Only a synoptic pressure gradient at the surface that forced the cold air away from the barrier towards the east could flush out the cold pool.

2.4 Laboratory simulations

2.4.1 Two-dimensional obstacles

Baines and Hoinka (1985) carried out towing experiments with two-dimensional obstacles of various shapes in a continuously stratified tank without rotation and a radiative upper boundary (i.e. vertically propagating waves were not reflected back into the tank). Their results agreed qualitatively with the numerical simulations of Pierrehumbert and Wyman (1985) although the values of the thresholds differed somewhat: linear theory and Long's model described the upstream flow well for Froude numbers > 2 , columnar disturbances propagated infinitely far (without friction) upstream for $0.5 \leq F \leq 2$, wave breaking with the formation of a stagnant well-mixed layer above the mountain occurred for $F < 2/3$, and blocked fluid appeared upstream of the obstacle for $F \leq 0.5$. All the thresholds varied somewhat depending on the exact obstacle shape.

Baines (1987) reviews also laboratory studies of interactions of single and double layer fluids with obstacles. These finite-depth studies, however, are not as important in the atmosphere as the previously described, stratified and unbound case.

2.4.2 Three-dimensional obstacles

With a model setup where the fluid could pass around the obstacle on one side, Baines (1979) found upstream blocking for $F \leq 0.5$, just as in the pure two-dimensional case. The depth of the blocked layer increased roughly linearly to the depth of the mountain as the Froude number approached zero.

For an axisymmetric cone (Snyder et al., 1985) blocked fluid of a depth $1 - F$ formed, just as in two-dimensional towing tank (section 2.4.1) and numerical (section 2.3) simulations and as predicted by Smith's (1985) nonlinear hydraulic theory (section 2.2). This result, however, did not hold for a triangularly shaped ridge. A horizontally oriented vortex formed in that case (just as deep as in Smolarkiewicz and Rotunno's (1990) numerical simulations) on the upstream slope and the non-dimensional depth of the separated lower layer exceeded $1 - F$.

Snyder et al. (1985) also investigated the dependence of the flow structure on the angle of incidence of the upstream flow on a sinusoidal ridge. For angles between 45° and 90° the non-dimensional blocked depth was still approximately $1 - F$, but was larger for angles less than 45° since more of the fluid went around the obstacle in that case instead of over it.

2.5 Summary

Deflection and stagnation of low-level air have been observed upstream of many mountain ranges. However, it is not trivial to determine whether a location is blocked or not and different researchers have reached opposite conclusions for the same case. The flow deflected along barriers large enough for the Coriolis force to be important shows a balance of synoptic scale pressure gradient and frictional force in the along-mountain

direction and geostrophic (relative to the mountain-induced mesoscale high) balance in the cross-mountain direction.

Theoretical studies as well as numerical and laboratory simulations identified the piling-up of denser air on the windward slope of the barrier and upstream propagating columnar disturbances produced by wave breaking as the cause for orogenic blocking. The mountain-induced mesoscale high has a relative magnitude of one hPa. Stability, wind speed and shear, and shape and height of the obstacle control the behavior of the flow and the appropriate nondimensional control parameters are the Froude, Rossby and Richardson numbers. Friction seems to be important for obstacles of a height comparable to the depth of the frictional boundary layer but plays only a modifying role, eg. by making a steady state possible, for higher mountains.

Previous studies established the "why" and "where" of blocking and thus set up the base for looking into the question of the evolution of a blocking cycle, which will be pursued in the remaining part of this study.

3 Data

3.1 Design of observational and modeling study

Previous observational studies of blocking were mostly interested in the flow characteristics during a blocked period but their temporal resolution did not suffice for a look on how a whole cycle from blocked to unblocked and back to blocked flow evolved. No numerical or laboratory studies with the exception of Lee et al. (1989) have investigated the effects of a temporally varying large scale flow on blocking. This study, on the other hand, set out to explore the blocking evolution.

3.1.1 Design of the observational study

Previous work reviewed in chapter two revealed several characteristics of blocked flow:

- possibility of a flow reversal zone on the upwind slope
- deflection
- horizontal limitation of upstream extent of blocking due to Coriolis effects
- significant wind shear (directional and speed) at the top of the blocked layer
- upstream influence extends to approximately one radius of deformation

To observe these features it seemed necessary to measure winds to well above mountaintop for at least three locations on the upwind slope: one close to the crest where flow reversal could be expected, the second close to one radius of deformation away from the barrier to detect the horizontal extent of the blocked layer, and the third farther away to get undisturbed upstream conditions. To find the exact upstream extent of the blocked flow additional measurements up- and downstream from the radius of deformation would be needed.

The Continental Divide was chosen for the barrier since it is large enough for Coriolis effects to be important and also for practical reasons (proximity). Its average crest height is approximately 3500 m ASL but some summits extend above 4000 m. However, in southern Wyoming the barrier dips down to approximately 2500 m ASL, forming a gap through which air deflected at the barrier can escape. The terrain far west of the Continental Divide is relatively flat with the exception of the Wasatch and Uinta Mountains, which form another high barrier (Fig 3.1a). The barriers tower high over the lower elevations, which the three-dimensional view of the topography used for the numerical simulations (Fig. 3.1b) shows nicely.

To discover how blocking evolves, observations of many blocking events are needed. Since a preliminary climatological study on the west side of the Continental Divide had identified winter as the season with the most and deepest blocking events (Mayr and McKee, 1990), a period from December 20, 1991, through February 25, 1992, was chosen. No other observational platform but the wind profiler fulfilled the requirements of frequent, high-reaching, unattended wind measurements in complex terrain over a long period.

NOAA's Wave Propagation Laboratory, Colorado State University and the US Army provided three wind profilers at the desired locations: close to the barrier, one radius of deformation away, and far upstream.

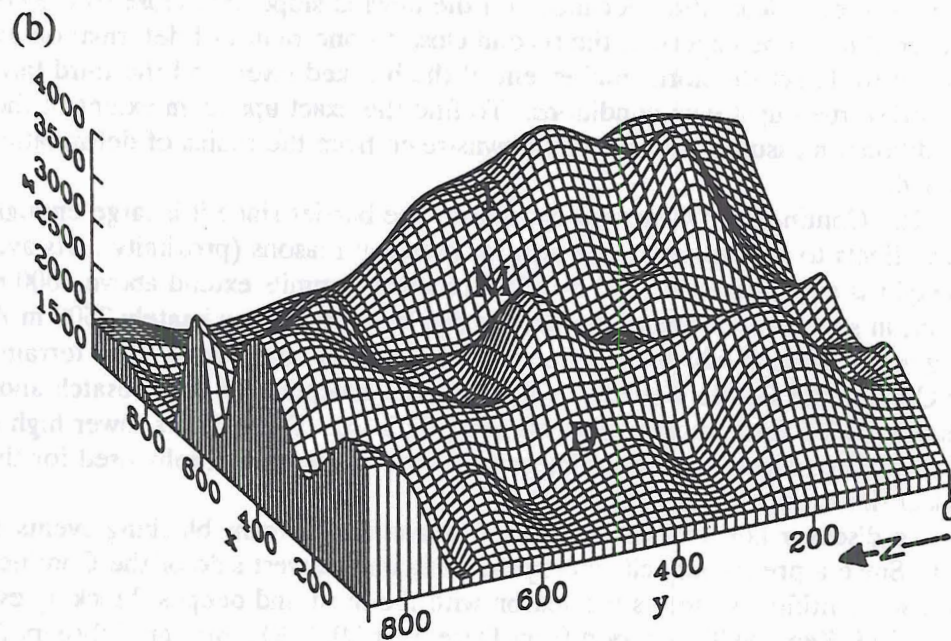
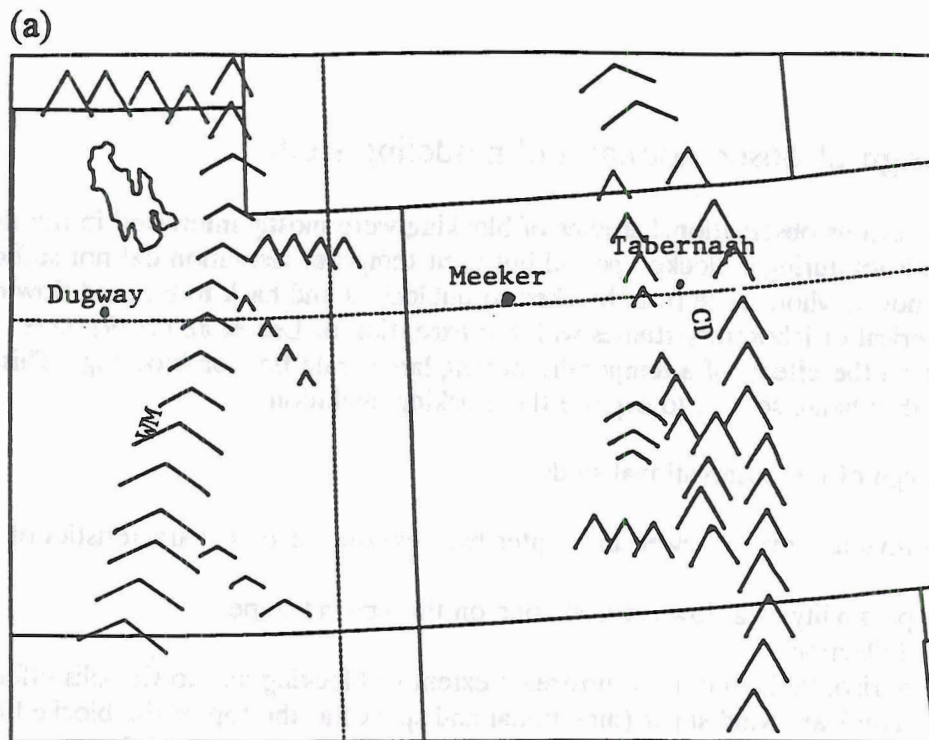


Fig 3.1: (a) location of profiler sites; (b) silhouette-averaged topography used for the numerical simulations in chapter six with the profiler locations (D=Dugway, M=Meeker, T=Tabernash). The Wasatch Mountains are marked *WM*, the Continental Divide *CD*. The arrow denotes north.

Most of the methods to determine whether the flow is blocked use the wind and temperature field. However, the radio acoustic sounding system (RASS), an add-on part to the wind profiler measuring virtual temperature, was available in only one location for only part of the experiment. To compare methods based on wind and temperature with purely wind-based ones three special observations periods (SOP) employing radiosondes were also carried out at the two locations closest to the Continental Divide on February 8-9, 9-10 and 21, 1992. The additional temperature and humidity information gave a more complete picture of the state of the atmosphere. Appendix A contains the launch times and lowest pressures reached for all soundings during the SOPs.

Since Mayr and McKee (1990) found blocking evolution to be tied to synoptic events the bidaily soundings from the regular rawinsonde network needed to be incorporated into the study. The 00 UTC and 12 UTC soundings for December 1991 through February 1992 were obtained from the National Center for Atmospheric Research (NCAR) archives for an area from 30° N, 125° W to 50° N, 87° W.

3.1.2 Purpose of the modeling study

Computing power and sophistication of numerical models now allow the realistic simulation of flow in a large mountainous domain making it possible to achieve the three goals of the modeling part of this study:

- i) to examine the effect that Coriolis force has on blocked flow upstream of the Continental Divide
- ii) to investigate the characteristics of the three-dimensional flow field in that area during both a blocked and unblocked situation thus complementing and adding to the observational data along a transect, and
- iii) to find out whether due to the low point of the Continental Divide in Northern Colorado and southern Wyoming the behavior of the blocked flow differed depending on the direction of the impinging wind.

3.1.3 Observational equipment and location

a) Tabernash

At 2620 m ASL at 39°58'53" North and 105°53'52" West this location was just 15 km west of and 900 m below the Continental Divide and thus expected to observe the most blocked periods of all sites and also flow reversals. NOAA's 915 MHz boundary layer profiler (Ecklund, 1990) was ideally suited for this site because of its small range bins of 100 m. The fact that it reached only 2-4 km above ground was no significant drawback for this experiment since that range extended well above mountaintop.

With the exception of two hours needed to pull collected data off the computer on Jan 21, 1992, the profiler operated continuously from December 19, 1991 through February 13, 1992. It sat on the roof of the club house of the golf course in Tabernash, Colorado. Table 3.1 lists the profiler specifications.

b) Meeker

A snow covered field at the Meeker Plant Center in Colorado hosted the 14x14 m five-beam phased antenna array of CSU's 404 MHz profiler manufactured by Tycho

Table 3.1 : Specifications of 915 Mhz profiler in Tabernash. The velocity resolution for all beams was 0.32 m/s. The column with in/coherent averages gives the number of power spectra and signals, respectively, that are averaged together during signal processing (compare section 3.2). The pulse repetition period is *PRP*.

beam	azimuth angle [deg]	elevation angle [deg]	height of first gate [m AGL]	gate length [m]	number of gates	in/coherent avg.	PRP [μ s]
1	260	75	152	101	20	320/35	25
2	167	75	152	101	20	320/35	25
3	0	90	157	105	20	320/35	25
4	260	75	203	203	25	134/35	60
5	167	75	203	203	25	134/35	60
6	0	90	210	210	25	134/35	60

(Winston, 1990). Table 3.2 lists its technical specifications. Its exact location was determined from a USGS 7.5 minute topographical map as $40^{\circ}17'11''N$, $107^{\circ}51'23''W$ at 1989 m ASL, which is 185 km west of and 1500 m below the average elevation of the Continental Divide. Assuming a buoyancy frequency, N , of 0.01 s^{-1} , (2.6) yields a radius of deformation of 150 km and for $N = 0.015 \text{ s}^{-1}$, L_R becomes 225 km. The profiler in Meeker was therefore on the edge of the area in which scale analysis and numerical simulations predict blocking to be noticeable.

Due to ground clutter usually only data to approximately 6 km ASL were usable.

RASS measured virtual temperature January 15 - 18, 1992, January 20 - 24, 1992, and February 16 - 25, 1992 every 30 or 120 minutes. Usually it did not reach higher than to one gate above the average height of the Continental Divide (3739 m ASL).

c) Dugway

The U.S. Army operates a five-beam 404 MHz wind profiler manufactured by TYCHO (Winston, 1990) at the Dugway Proving Ground in Utah. Its position as determined by satellites is $40^{\circ}12'N$ and $113^{\circ}10'48''W$ at 1293 m ASL, 635 km west of and 2200 m below the average elevation of the Continental Divide. The Wasatch Range forms a 1700 m high barrier about 100 km east of the profiler location so that although the location is far enough removed from the Continental Divide to not feel its blocking influence the flow there is not undisturbed but subject to blocking effects from the Wasatch Mountains.

Table 3.3 lists the technical specifications of the profiler. Dr. Al Astling provided us with data from December 19, 1991 through February 19, 1992, when lightning knocked the profiler out. Data from December 24, 1991 through January 6, 1992 are missing.

Table 3.2: Specifications of 404 MHz profiler in Meeker; the center of the first gate is 500 (6913) m above the ground, and each of the 36 gates is 250 (500) m long in low (high) mode. The column with in/coherent averages gives the number of power spectra and signals, respectively, that are averaged together during signal processing (compare section 3.2). The pulse repetition period is *PRP*.

beam	azimuth angle [deg]	elevation angle [deg]	height of first gate [m AGL]	velocity resolution [m/s]	in/coherent averages	PRP [μ s]	comments
1	90	75	6913	0.25	46/24	240	high mode
2	90	75	500	0.17	26/88	100	low mode
3	0	75	6913	0.25	46/24	240	high mode
4	0	75	500	0.17	26/88	100	low mode
5	0	90	6913	0.25	26/24	240	high mode
6	0	90	500	0.17	28/80	110.5	RASS
7	270	75	6913	0.25	46/24	240	high mode
8	270	75	500	0.25	26/88	100	high mode
9	0	90	500	0.04	6/368	100	low mode
10	180	75	500	0.17	26/88	100	low mode

Table 3.3: Specifications of the 404 MHz profiler in Dugway; the center of the first gate is 500 m above the ground, and each of the 36 gates is 250 m long. The column with in/coherent averages gives the number of power spectra and signals, respectively, that are averaged together during signal processing (compare section 3.2).

beam	azimuth angle [deg]	elevation angle [deg]	in/coherent averages
1	90	75	35/64
2	270	75	35/64
3	0	75	35/64
4	180	75	35/64
5	0	90	22/104
6	0	90	22/104

3.2 Principles of wind profilers and RASS (radio acoustic sounding system)

The meteorological community first used radars to observe hydrometeors. Sometimes, however, they received echoes from seemingly clear air. While insects and birds caused some of these mysterious echoes, another mechanism, the Bragg scatter, could explain the remaining cases. After that discovery specially designed radars observed echoes from the clear air (eg. Kropfli et al., 1968; Richter, 1969). The basic antenna array design and signal processing techniques for present-day wind profilers stem from early ionospheric radar observations (Woodman and Guillen, 1974). In the late 1970s and early 1980s the Wave Propagation Laboratory of NOAA pressed hard for the development of operational wind profilers.

Most of the modern wind profilers use a phased antenna array to produce beams of a series of coherent electromagnetic pulses with wavelengths between 0.3 and 6 m. Some of the energy in such a pulse is scattered from turbulent refractive index inhomogeneities of the size of half the wavelength (Doviak and Zrnic, 1984, pp374-375) into all directions ("Bragg scatter"), some of it back to the radar. Turbulent eddies that are carried along by the mean wind generate the inhomogeneities in the refractive index, which is a function of humidity (strongest in the lower atmosphere), temperature (important above the mid-troposphere) and pressure (Fairall, 1991). Due to the finite length of an electromagnetic pulse and the finite width of the beam, the received signal carries information from many eddies within a certain volume. From the travel time the distance between scatterers and radar can be detected, and from the phase shift from one pulse to the next the Doppler shift and thus the radial velocity of the refractive index inhomogeneities. For a 404 MHz profiler that shift is less than 100 Hz, i.e. only 10^{-7} the original frequency! The sampling frequency is up to two magnitudes higher (1000 - 10000 Hz) to allow a coherent integration (i.e., vector sum of N pulses) of the signal, which improves the signal-to-noise ratio by a factor directly proportional to N . This is called "coherent averaging" since it preserves the phase information of the signal.

After a transformation of the signal from the time into the frequency domain by a Fast Fourier Transform the resulting power spectra are averaged again ("incoherent averaging") to smooth out the noise "floor", increase the signal-to-noise ratio (proportional to the square root of number of averaged spectra) and make the peak of the signal better defined. The zeroth moment of the resulting spectrum gives the signal strength, the first moment the radial velocity of the scatterers, and the second moment the spectral width, i.e. the spread of radial velocities of the scatterers within the sampling volume.

Most commonly a wind profiler sequentially creates three to five beams, one pointing vertically and the others tilted slightly away from the zenith (Fig. 3.2). The horizontal and vertical wind components contribute to the radial velocities (positive towards the profiler) for a profiler arrangement as depicted in Fig. 3.2 as follows: The subscripts N , E , S , W denote the north, east, south and west antenna beams, V_r is the radial velocity and θ the zenith angle of the tilted beams. From (3.1) the wind components are

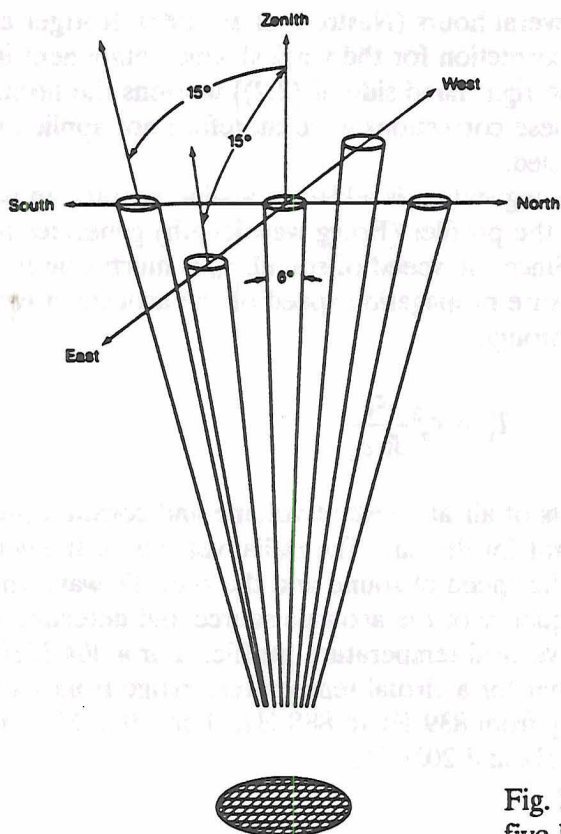


Fig. 3.2: Antenna configuration of the five-beam wind profilers used in Meeker and Dugway.

$$\begin{aligned}
 V_{rN} &= -v \cos \theta + w \sin \theta \\
 V_{rE} &= -u \cos \theta + w \sin \theta \\
 V_{rS} &= +v \cos \theta + w \sin \theta \\
 V_{rW} &= +u \cos \theta + w \sin \theta \\
 V_{rZ} &= w
 \end{aligned} \tag{3.1}$$

$$\begin{aligned}
 u_E &= -\frac{V_{rE}}{\cos \theta} + V_{rZ} \tan \theta \\
 v_S &= +\frac{V_{rS}}{\cos \theta} - V_{rZ} \tan \theta \\
 u_W &= +\frac{V_{rW}}{\cos \theta} - V_{rZ} \tan \theta \\
 v_N &= -\frac{V_{rN}}{\cos \theta} + V_{rZ} \tan \theta
 \end{aligned} \tag{3.2}$$

The accuracy of the vertical wind measurements is usually not good enough for reliable estimates of vertical wind in non-convective, non-precipitating situations unless the

measurements are averaged over several hours (Nastrom et al., 1990; Röttger and Larsen, 1990). Under such conditions the correction for the vertical wind component in the tilted radial velocities (second term on the right hand side of (3.2)) worsens the horizontal wind estimates (Strauch et al., 1987). These corrections were therefore not applied in this study nor was the vertical velocity used.

When a radio acoustic sounding system is added to a wind profiler an acoustic signal of half of the wave length of the profiler (Bragg wavelength) generates the refractive index inhomogeneities. Since the speed of sound, c_s , is much slower than the speed of light, the profiler can measure propagation speed of the acoustic wave and thus virtual temperature of the air, T_v , through

$$T_v = c_s^2 \frac{c_v}{R c_p} \quad (3.3)$$

where c_v and c_p are the specific heats of air at constant volume and constant pressure, respectively, and R is the gas constant for dry air. The radial velocity of the vertical beam is then the speed of sound. Since the speed of sound and the acoustic wavelength change with temperature, changing the frequency of the acoustic source and detecting the altitude of the backscattered signal yields a vertical temperature profile. For a 404 MHz profiler the Bragg wavelength is 38 cm so that for a virtual temperature range from -20°C to 10°C the acoustic frequency needs to vary from 839 Hz to 888 Hz. For a 915 MHz profiler these numbers are 16 cm and 1945 Hz and 2058 Hz.

3.3 Quality control

3.3.1 SOP radiosoundings

After ensuring that the pressure of the sounding decreased monotonically with time, the data was put through a hydrostatic check. In a second pass the soundings were plotted, examined manually and bad data points were eliminated/corrected.

3.3.2 NWS rawinsoundings

NCAR archives upper air soundings that the NMC checked extensively using the Comprehensive Quality Control (CQC) algorithm (Collins and Gandin, 1990) so that no further quality control was necessary.

3.3.3 profiler winds

3.3.3.1 Error sources and remedies

a) ground clutter

Once the radar backscatter signal has been transformed into spectral space an algorithm picks what it thinks is the meteorological signal. Unfortunately there is usually more than one peak in the whole radial velocity spectrum for various reasons. The phased array antennae cannot create one perfect beam but rather spread the energy into a main lobe and several sidelobes of considerable intensity. Even though the sidelobes are

weaker the signal backscattered from a hard target will be much stronger than the one produced by refractive index inhomogeneities in the main lobe. Hard targets like terrain (ground clutter) are usually stationary. Thus eliminating the peak around zero radial velocity eradicates that contamination with two exceptions: 1) trees and grass can move in the wind; a wider window around zero alleviates that problem but also discards some good measurements of very weak wind, or 2) a sidelobe might hit a moving target such as a vehicle or airplane.

Especially at distances of more than approximately 4-5 km from the profiler in Meeker, ground clutter by hills prevented the software from detecting the atmospheric peak.

b) precipitation

Notably the 915 MHz profiler but also the 404 MHz profilers are sensitive to precipitation. While the vertical contribution to the radial velocity in the tilted beams can usually be neglected in clear sky situations the fall speed of precipitation (approximately 5 m/s for rain, less than 1 m/s for snow (Rogers and Yau, 1989)) must be taken into account to avoid horizontal wind measurements being off by several to tens of meters per second (Wuertz et al., 1988).

Since the quality control routine easily detects errors of that magnitude the vertical velocities were not correct in the tilted beams in order to not degenerate the data quality during clear conditions (Wuertz et al., 1988).

c) receiver recovery noise

Both the TYCHO and NOAA profilers have collocated transmitters and receivers. Electronic noise generated by switching from transmitting to receiving takes a few microseconds to ebb so that any backscatter signals received during that time will be contaminated. The time interval from the switch to the first measurement was chosen long enough to avoid that problem.

d) aliasing

When the profiler receives echoes from more than one pulse at a time, range aliasing occurs. Choosing a pulse repetition rate, PRP , greater than $2 r_{max}/c$, where r_{max} is the greatest altitude for which a strong enough backscattered signal is received and c the speed of light, circumvents range aliasing. On the other hand one has to sample the signal at least as often as the Nyquist frequency of the maximum expected radial velocity so as to not alias high velocities into lower ones. Mathematically put: $PRP * NCOH < \lambda$, where $NCOH$ is the number of coherently (i.e. time-domain) averaged signals and λ the profiler wavelength.

Again, the profiler PRP and $NCOH$ were appropriately chosen.

3.3.3.2 quality control algorithms

Since even a carefully chosen site never completely eliminates clutter problems and the currently used peak-picking software still has potential for improvement, a significant amount of erroneous radial velocity data remains and has therefore to be detected. A wide variety of quality control schemes have been devised and are currently in use. A median check compares a datum with the median of its neighboring (temporal and vertical) data and rejects it if it exceeds a threshold (Brewster, 1989). In a vertical consistency check data are eliminated if the shear between gates surpasses a threshold

(Brewster, 1989). Statistical interpolation (eg. Daley 1991 for an excellent introduction) assigns weights to observed data; therefore flagging data below a threshold turns the method from an analyzing into a quality control tool (Brewster 1989). Hayden and Purser (1988) designed a recursive filter, which is used as a successive correction method. Consensus averaging (Fischler and Bolles, 1981), which is widely used to obtain hourly averages from profiler wind measurements, can also be used to flag the data that did not fit the chosen sample consensus.

All these methods use only part of the information provided by the signal processing routine, namely the radial velocity, but neglect signal and noise strength and the spectral width.

The quality control algorithm consists of two passes through the data. The first one is a threshold check for signal-to-noise ratio, absolute minimum value of signal strength, minimum of the modulus of the radial velocity, how close to zero the radial velocity is, and an absolute and relative minimum spectral width. The latter is the only objective threshold, the others are subjective. The spectral width of a backscattered signal is always finite, i.e. more than one radial velocity is measured, due to the finite width of the profiler beam, turbulence and shear of the mean wind within the sampling volume. Thus the spectral width always has to be at least the amount caused by the finite beam width σ_{beam} , which is

$$\sigma_{beam} = \frac{V_0 \theta_2}{\sqrt{8 \ln 2}} \quad (3.4)$$

(Nathanson, 1991), where V_0 is the radial velocity at the beam center, and θ_2 the two-way, half-power antenna beamwidth in radian. Any datum with a measured spectral width lower than the one computed from (3.4) with the measured radial velocity was discarded.

In the second pass a robust regression was used to detect the remaining outliers. Following Rousseeuw and Leroy (1987) the widely used least squares (LS) regression is very vulnerable to outliers. The concept of a "breakdown point" describes the sensitivity of a regression to outliers. The breakdown point is defined as the smallest fraction of contamination that can cause an estimator to take on values arbitrarily far from the "truth". For the LS regression it is proportional to $1/n$, n being the number of points towards which the regression is fitted. For a large sample size this goes to zero, which means that one single outlier can cause havoc as Fig. 3.3 shows! Instead of minimizing the *sum* of the squares of the residuals (the difference between the observed and regression-estimated value), Rousseeuw and Leroy (1987) suggest minimizing the *median* of the squares of the residuals. This least median of squares estimator (LMS), as they call it, has a breakdown point of 50%, the theoretical maximum for any estimator. For a linear regression with intercept the LMS solution geometrically corresponds to finding the narrowest strip covering half of the observations (Fig. 3.3).

The only drawback of the LMS method is that its calculation unlike the LS is not straightforward but rather computationally expensive.

Analogous to the standard deviation for the LS a robust scale estimator can be defined. If the residuals are normally distributed, then roughly 98% of the normalized (with the scale estimator) residuals will lie in the interval $[-2.5, 2.5]$.

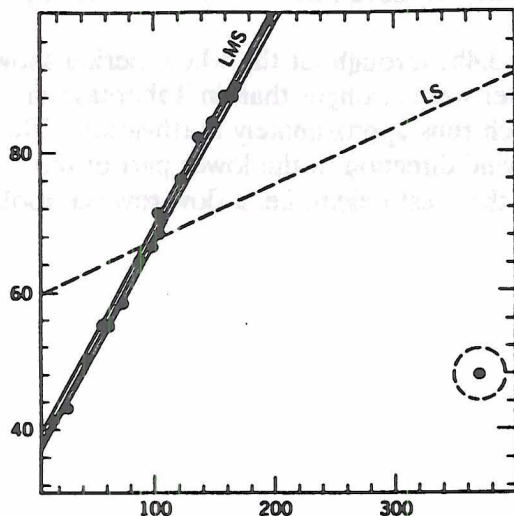


Fig. 3.3: Comparison of least median of squares (LMS) and least sum of squares (LS) for a data set with one outlier. The two lines around the LMS-fit show its geometrical explanation as the narrowest strip covering half of the observations.

An LMS regression was computed both temporally and vertically and data was flagged whose normalized residuals were outside the interval $[-2.5, 2.5]$. A linear change of wind can only be a good approximation for limited time and height intervals. Six datapoints were used for both regressions, which timewise corresponds to about an hour for the TYCHO profilers in Meeker and Dugway, and fifteen minutes for the NOAA profiler in Tabernash, and heightwise to 1500 m (TYCHO), 600 m (NOAA low mode), and 1200 m (NOAA high mode), respectively. Since wind in such height intervals can be quite non-linear (eg. a jet), an LMS regression was calculated first from gate 1 to 6, then from gate 2 to 7, etc up to the top, and a datum rejected only if it had been flagged by more than half of the LMS regression passes that used this datum. This procedure was chosen quite pragmatically as the one out of several others tested whose results compared most favorably with a thorough subjective quality control.

3.3.4 RASS

The amount of RASS data was small enough to allow a subjective quality control. Gross outliers were eliminated by examining time series of virtual temperature, T_v , for each range gate and then the remaining data subjected to a vertical gradient check, discarding data causing a greater than dry adiabatic lapse rate: $-dT_v/dz > g/c_p$, where g is gravitational acceleration and c_p the specific heat for dry air under constant pressure.

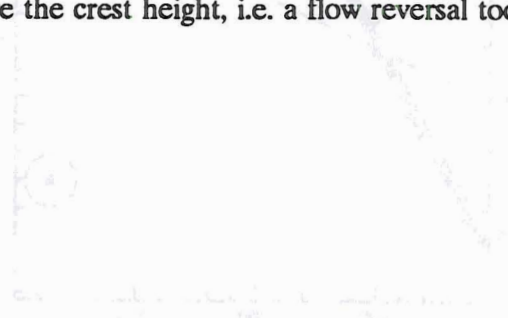
3.4 Examples of wind profiler measurements

As the concluding part of this chapter, a time-height cross section of horizontal wind vectors measured by the profilers in Tabernash and Dugway on January 16-17, 1992 is shown. Initially a blocked layer is present both in Tabernash and Dugway.

The winds in the blocked layer in Tabernash (Fig. 3.4a) were very weak, generally less than 1 m/s. At 13 LST Tabernash became unblocked and the stronger winds from

above the barrier made their way down to the surface. Seven hours later the blocking formed again.

A blocked layer existed in Dugway (Fig. 3.4b) throughout the whole period shown, although its depth varied. The winds in that layer were stronger than in Tabernash and were mostly directed parallel to the barrier, which runs approximately north-south. This indicates flow deflection. Around 17 LST the wind direction in the lower part of the blocked layer was opposite from the one above the crest height, i.e. a flow reversal took place.



The flow reversal in the lower part of the blocked layer was observed at 17 LST. This is shown in Fig. 3.4b. The wind direction in the lower part of the blocked layer was opposite from the one above the crest height, i.e. a flow reversal took place.

The flow reversal in the lower part of the blocked layer was observed at 17 LST. This is shown in Fig. 3.4b. The wind direction in the lower part of the blocked layer was opposite from the one above the crest height, i.e. a flow reversal took place.

The flow reversal in the lower part of the blocked layer was observed at 17 LST. This is shown in Fig. 3.4b. The wind direction in the lower part of the blocked layer was opposite from the one above the crest height, i.e. a flow reversal took place.

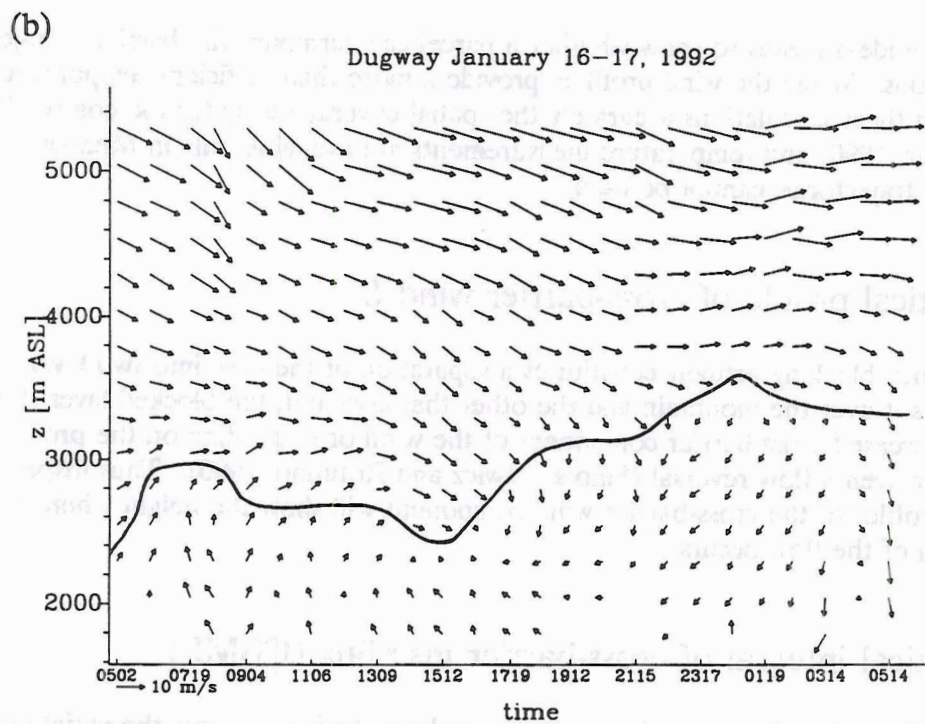
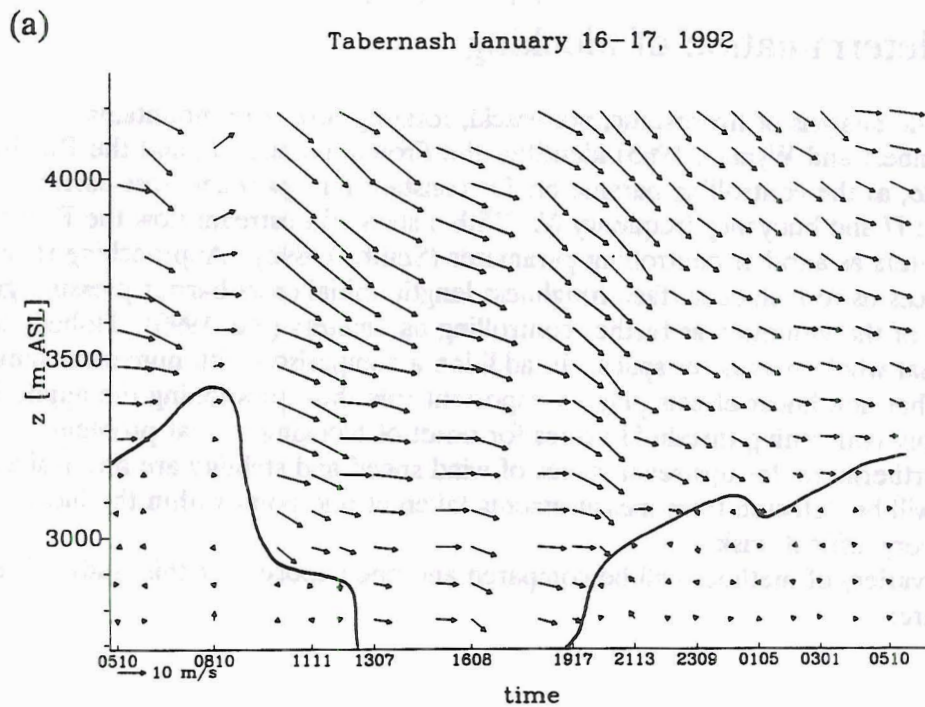


Fig. 3.4: Time-height cross-section of horizontal windvectors in (a) Tabernash and (b) Dugway from January 16, 1992, 05 LST through January 17, 1992, 05 LST. Time is in hours and minutes. The reference wind vector shows a 10 m/s wind from W. A bold line marks the top of the blocked layer defined as a quasi-discontinuity in the vertical profile of the cross-barrier component.

Local determination of blocking

Scale analysis of hydrostatic, non-viscid, rotating flow over mountains (Pierrehumbert and Wyman, 1985) identifies the Froude number, F , and the Rossby number, Ro , as the controlling parameters for constant far-upstream cross-barrier component U and buoyancy frequency N . With a sheared upstream flow the Richardson number enters as another controlling parameter (Smith, 1989b). Approaching reality more closely forces us to include surface roughness length, initial cross-barrier pressure gradient and shape of the mountain as further controlling parameters (Xu, 1990). Nobody has yet mapped that whole parameter space. In addition a comparison with numerical simulations indicates that non-linear effects play an important role thus questioning the applicability of linear theory concerning threshold values for onset of blocking to that problem.

Furthermore, far upstream values of wind speed and stability are not available. Blocking will be detected from measurements taken at one point within the blocked region, a very difficult task.

A variety of methods will be compared and one chosen for this study. The methods are:

4.1 Trajectories

The ideal means to show whether a parcel can surmount the barrier is trajectory computations. While the wind profilers provide a more than sufficient temporal resolution to perform these calculations accurately the spatial coverage is by far too coarse (Rolph and Traxler, 1990) and temperature measurements are available only in Meeker. Therefore trajectories cannot be used.

4.2 Vertical profile of cross-barrier wind U

Since blocking actually constitutes a separation of the flow into two layers, one that makes it over the mountain and the other that does not, the blocked layer should have a decreased cross-barrier component of the wind or depending on the proximity to the barrier even a flow reversal (Smolarkiewicz and Rotunno, 1990). Thus inspecting the vertical profiles of the cross-barrier wind component will show the height where the separation of the flow occurs.

4.3 Vertical integral of cross-barrier massflux (CBMF)

This method improves the previous one by including not only the variation of the cross-barrier wind component with height but also the density variations. In addition the vertical integral

$$CBMF = \int_0^z \rho u dz \quad (4.1)$$

where ρ is the density of air and u the cross-barrier wind component, smooths out small scale variations.

4.4 Vertical integral of cross-barrier kinetic energy flux (CBEF)

Since u appears squared in the kinetic energy the separation between unblocked and blocked layers shows up even better in vertical integrals of cross-barrier kinetic energy flux

$$CBEF = \int_0^z \rho \frac{u^2}{2} dz \quad (4.2)$$

4.5 Conserved variable diagram

Equivalent potential temperature and total mixing ratio (or mixing ratio in absence of clouds), which are conserved for adiabatic processes without precipitation, together with pressure or height completely determine the thermodynamic state of a parcel (Betts, 1982). By plotting a diagram of equivalent potential temperature and mixing ratio several atmospheric processes can be identified (Betts and Albrecht, 1987) as shown in Fig. 4.1: precipitation leaving the parcel ($A \rightarrow B$) reduces its total water mixing ratio but not its equivalent temperature. Radiative cooling ($C \rightarrow D$) affects θ_e but not the mixing ratio. Mixing between two different air parcels located at E and F results in a mixture parcel that falls on a mixing line, a straight line connecting the thermodynamic states of the two original parcels. The fraction of each original parcel in the mixture determines its position (G) on the mixing line.

After separation of the atmosphere into two layers by blocking one would expect at least two mixing lines on a conserved variables diagram, one within the blocked part and the other for the layer surmounting the barrier. However, advection by valley and plateau circulations within the blocked layer complicate the structure of the conserved variables diagram. Generally the kink in the conserved variables diagram closest to the barrier coincides with the top of the blocked layer.

4.6 Froude number

As mentioned above the Froude number is the controlling parameter in uniform flow without friction and rotation impinging on a mountain. It should be calculated from far upstream values. Computing it from values within the blocked region is questionable but the only method possible with the available data. Since the actually observed flow is

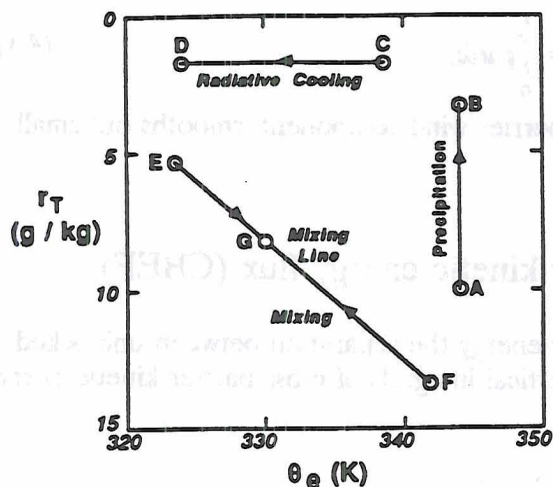


FIG 4.1: Conserved variable diagram: Precipitation (A→B) decreases the total water mixing ratio, r , but not the equivalent potential temperature θ_e ; radiative cooling (C→D) only decreases θ_e ; an air parcel at point G is made up of two parts of air from E and one part from F.

never uniform the outcome of the computation will very much depend on how the average cross-barrier component and buoyancy frequency are determined. In this study the integral average cross-barrier component in the layer 500 m below to 200 m above barrier top and the integral average of the buoyancy frequency between surface and crest are used.

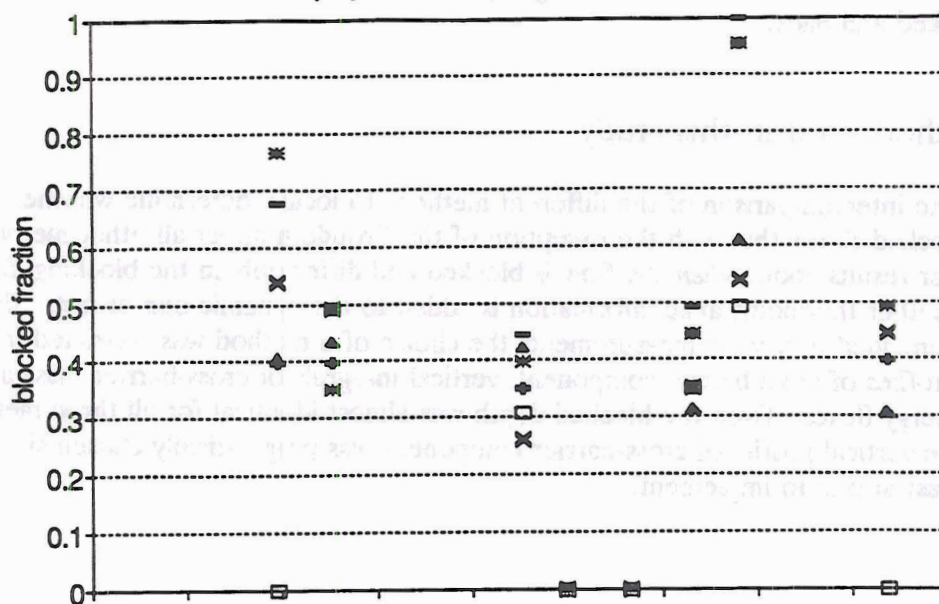
4.7 Contours of U/N

The ratio of U/N can be regarded as the maximum height to which a parcel could be lifted if all its kinetic energy were converted into potential energy. Since the parcel instead is lifted gradually as it approaches the mountain where there is a positive pressure anomaly due to piling up of denser air (Smith, 1989b) this method only provides a lower limit for the blocked depth.

4.8 Intercomparison

Fig 4.2 shows the fraction of barrier height estimated to be blocked by the different methods in Tabernash and Meeker during the second SOP from February 10-12, 1992. A short wave disturbance had just passed the region before the SOP began, and initially both places were blocked. The passage of a second short wave with the help of diurnal heating managed to unblock Tabernash but only reduced the depth of the blocked layer in Meeker, whose barrier height is 600 m taller. Generally, mass and kinetic energy flux integrals, profiles of U/N, conserved variable diagram, and (not as good) U-profiles yield similar results. The Froude number in Meeker, however, always shows extreme values compared with the other methods probably due to the use of one single barrier height for different wind directions despite a highly directionally varying barrier profile. It works better in Tabernash, closer to the barrier, but still falsely indicates two partially blocked situations as unblocked, highlighting the problems of having to use average buoyancy frequency and wind speed values and how to form these averages.

(a) Tabernash



(b) Meeker

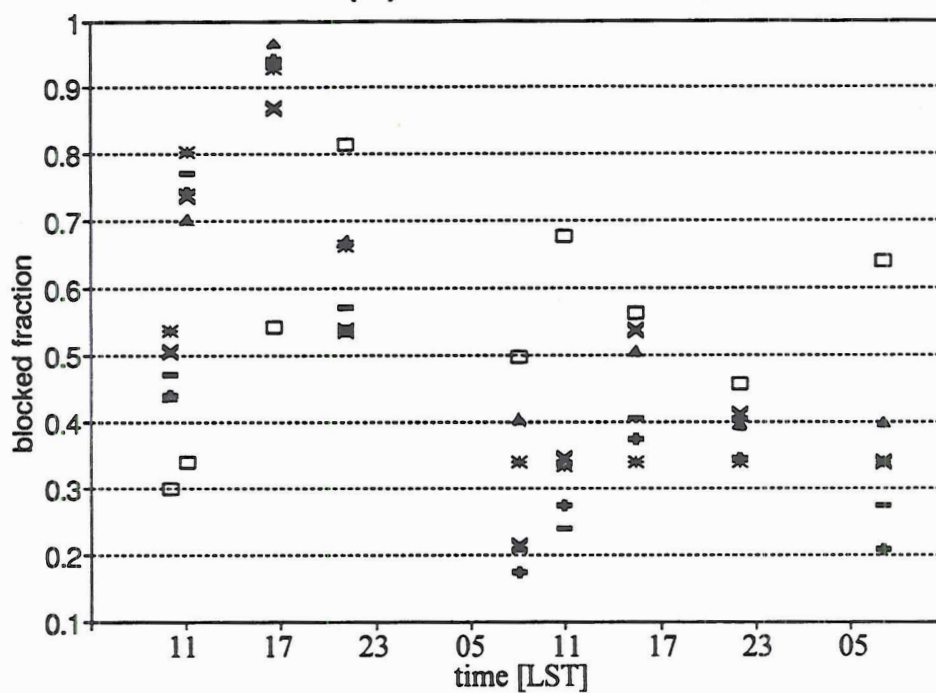


FIG 4.2: Comparison of different methods to determine depth of blocked layer (as a fraction of barrier depth) for (a) Tabernash and (b) Meeker: vertical integral of cross-barrier massflux (+), vertical integral of cross-barrier kinetic energy flux (-), conserved variable diagram (x), profiles of U/N (Δ), profiles of U ($*$), and Froude number (\square).

Notice the change of the blocking depth and also the rapid transition from blocked to unblocked and back.

4.9 Method used in this study

The intercomparison of the different methods to locally determine whether the flow is blocked shows that with the exception of the Froude number all other methods give similar results about *when* the flow is blocked and differ only in the blocking *depth* no matter whether thermodynamic information is added to the dynamic one or not. Since the profilers provided only wind measurements the choice of a method was restricted to the vertical profiles of cross-barrier component, vertical integrals of cross-barrier mass and kinetic energy fluxes. Even the blocked depth was almost identical for all three methods so that the vertical profile of cross-barrier component was pragmatically chosen since it was the easiest one to implement.

Observational results

5.1 Blocked periods

5.1.1 Determination of blocked flow

As discussed in chapter four the vertical profile of the cross-barrier wind component was used to determine whether a blocked layer existed since this method detected the duration of blocked flow as well as other, more complicated methods, and the blocking depth differed only slightly from the more complicated methods.

Since previous studies were not interested in the blocking evolution it was not known from the beginning how rapidly the transition from blocked to unblocked flow and vice versa would occur. To capture the details of these transitional periods, the individual profiler soundings with one vertical profile were used every two minutes in Tabernash, eleven minutes in Meeker, and six minutes in Dugway, instead of the hourly averaged data commonly used. The twelve hour interval between soundings of the regular rawinsonde network was too long to even capture all the blocked periods.

5.1.2 Statistics

Tables 5.1 - 5.3 contain the beginning and ending times of a blocked period (to the nearest hour) and the transition time. The transition time from unblocked to blocked is the time from the onset of blocking in the lowest gate until the time the depth of the blocked layer becomes quasi-stationary. The opposite holds for the transition from blocked to unblocked.

From the profiler measurements 23 blocking periods were identified in Tabernash, 12 in Meeker and 12 in Dugway. The average blocked period lasted one and a half days (Table 5.4): 32 hours in Tabernash, 29 in Meeker and 50 in Dugway. The duration, however, varied greatly from 3 to 187 hours.

With westerlies above mountaintop the station farthest away from a major barrier, Meeker, had the least blocking. Since the distance from Meeker to the Continental Divide is roughly one radius of deformation, Meeker is on the edge of the upstream influence of the Divide. And since the depth of the blocked layer decreases with the distance from the barrier some shallow blocking events might have been missed when the blocking extended only up to the first gate of the wind profiler (500 m above ground).

During the winter of 1991/92 a large number of cut-off lows was located upstream of the Continental Divide. Eight periods, mostly at the end of December and the beginning of February, without a westerly component of at least 2 m/s above crest height occurred in Tabernash and Dugway, and seven were observed in Meeker (Table 5.5).

Despite the similar number of occurrences, the duration of these periods as a fraction of total observation time in Dugway doubled those at Tabernash and Meeker. In Dugway westerlies above ridge crest of more than 2 m/s occurred only slightly more than half of the time. When they blew the flow was almost always blocked.

Overall low level air could not flow eastwards over the mountains between 63% and 92% of the time (depending on the location), which means that although air might exchange on a local level among valleys, the regional replenishing of the low-level air is

Table 5.1: Periods of blocked flow in Tabernash. Beginning and ending dates are in months, days and hours, relative to LST.

start [MM/DD hh]	formation [hr]	end [MM/DD hh]	destruction [hr]
12/20 05	-	12/22 15	-
12/23 02	-	12/23 17	-
12/24 11	-	12/25 06	-
12/27 12	-	12/30 08	-
12/30 21	-	12/31 06	1
01/01 09	1	01/04 13	0.5
01/04 23	1	01/06 11	-
01/08 03	-	01/08 23	0.5
01/09 05	0.3	01/09 13	0.3
01/09 18	1	01/11 14	-
01/15 05	0.5	01/16 12	2
01/16 20	1	01/17 13	4
01/18 00	1	01/21 14	1
01/22 19	0.5	01/23 02	3
01/24 00	0.5	01/24 13	0.5
01/25 02	0.5	01/26 13	0.5
01/26 17	1	01/27 13	1.5
01/27 18	0.5	01/28 14	1
01/28 18	0.3	01/31 23	-
02/07 18	0.3	02/08 14	2
02/09 23	1.5	02/11 11	0.5
02/11 18	0.2	02/12 05	0.5
02/12 20	0.5	02/13 08	-

infrequent. Therefore the implementation of large pollution sources in that region could result in the accumulation of a high concentration of pollutants.

5.1.3 Blocking depth

The depth of the blocked layer varied greatly during the observational period (Fig. 5.1). A steady state was never achieved; even within one blocking event the depth of the blocked layer varied rapidly. Most frequently, however, the blocked layer reached at all three sites to at least half the barrier height but rarely up to mountaintop. As expected, the blocked layer never extended above the height of the crest. The transition between the blocked and unblocked states also happened quickly (compare section 5.1.4).

Table 5.2: Periods of blocked flow in Meeker. Beginning and ending dates are in months, days and hours, relative to LST. No profiler data were available for the time indicated with *.

start [MM/DD hh]	formation [hr]	end [MM/DD hh]	destruction [hr]
01/15 12	-	01/18 00	-
01/22 20	0.5	01/24 14	0.5
01/24 20	0.5	01/26 02	0.5
01/26 13	0.3	01/29 08	-
01/30 05	-	01/31 13	-
02/09 09	1	02/09 14	0.5
02/13 07	0.3	*	*
02/18 04	0.5	02/18 18	1
02/19 13	0.5	02/19 16	-
02/21 09	0.5	02/21 17	1
02/23 01	0.3	02/23 08	-
02/24 08	-	02/24 22	-

Table 5.3: Periods of blocked flow in Dugway. Beginning and ending dates are months, days and hours, relative to LST.

start [MM/DD hh]	formation [hr]	end [MM/DD hh]	destruction [hr]
12/18 17	-	12/18 23	-
01/10 05	-	01/11 07	-
01/13 05	1	01/14 13	3
01/15 14	-	01/17 09	-
01/21 02	-	01/28 21	-
01/30 10	-	01/31 16	-
02/01 00	-	02/02 01	-
02/07 00	-	02/10 16	0.5
02/11 04	1	02/11 09	0.3
02/11 11	0.3	02/14 01	0.3
02/14 10	2	02/15 23	2
02/17 16	0.5	02/19 10	-

Table 5.4: Number of blocking events, their minimum, average and maximum duration for the three profiler sites. "No westerly flow" is defined as no westerly wind component of at least 2 m/s between mountaintop and 500 hPa.

	Tabernash	Meeker	Dugway
blocking events	23	12	12
minimum, average, and maximum blocking duration [hours]	7 32 86	3 29 80	5 50 187
no westerly flow [%]	23.4	24.7	44.4
blocked when westerly [%]	72.2	51.3	85.4
no low-level easterly flow [%]	78.7	63.3	91.9

Table 5.5: Periods without a westerly wind component of at least 2 m/s in the layer between mountaintop and 500 hPa for the three profiler sites in Tabernash, Meeker and Dugway. Beginning and ending dates are in months, days and hours, relative to LST. The last period without westerlies in Meeker ended by the take down of the profiler and is marked by "**".

Tabernash		Meeker		Dugway	
start	end	start	end	start	end
12/19 17	12/20 05	01/15 04	01/15 12	12/18 23	12/23 07
12/22 16	12/23 02	01/18 00	01/20 14	01/06 13	01/10 05
12/23 17	12/24 11	01/29 08	01/30 05	01/11 17	01/13 05
12/25 06	12/27 12	01/31 13	02/01 02	01/15 03	01/15 14
12/30 08	12/30 21	02/02 04	02/05 11	01/17 09	01/21 02
01/06 11	01/06 22	02/23 08	02/24 08	01/28 21	01/30 10
01/11 14	01/12 22	02/24 22	*	01/31 16	02/01 00
01/31 23	02/07 18			02/02 01	02/08 00

In the afternoons and evenings of January 26, 27, and 28, and February 11 the atmosphere in Tabernash flipped quickly out of and back into a blocked state. The daytime heating and growth of the boundary layer and the nocturnal cooling seem to have influenced the state of the impinging flow on these days.

5.1.4 Transition between blocked and unblocked states

Tables 5.1-5.3 show that blocking forms very rapidly - within 15 minutes to 2 hours (an average of 40 minutes for all sites) and gets destroyed almost as rapidly - within 20 minutes to 4 hours (average 1 hour for all sites). Since no observations with such a high temporal resolution have been available previously this result comes as quite a surprise.

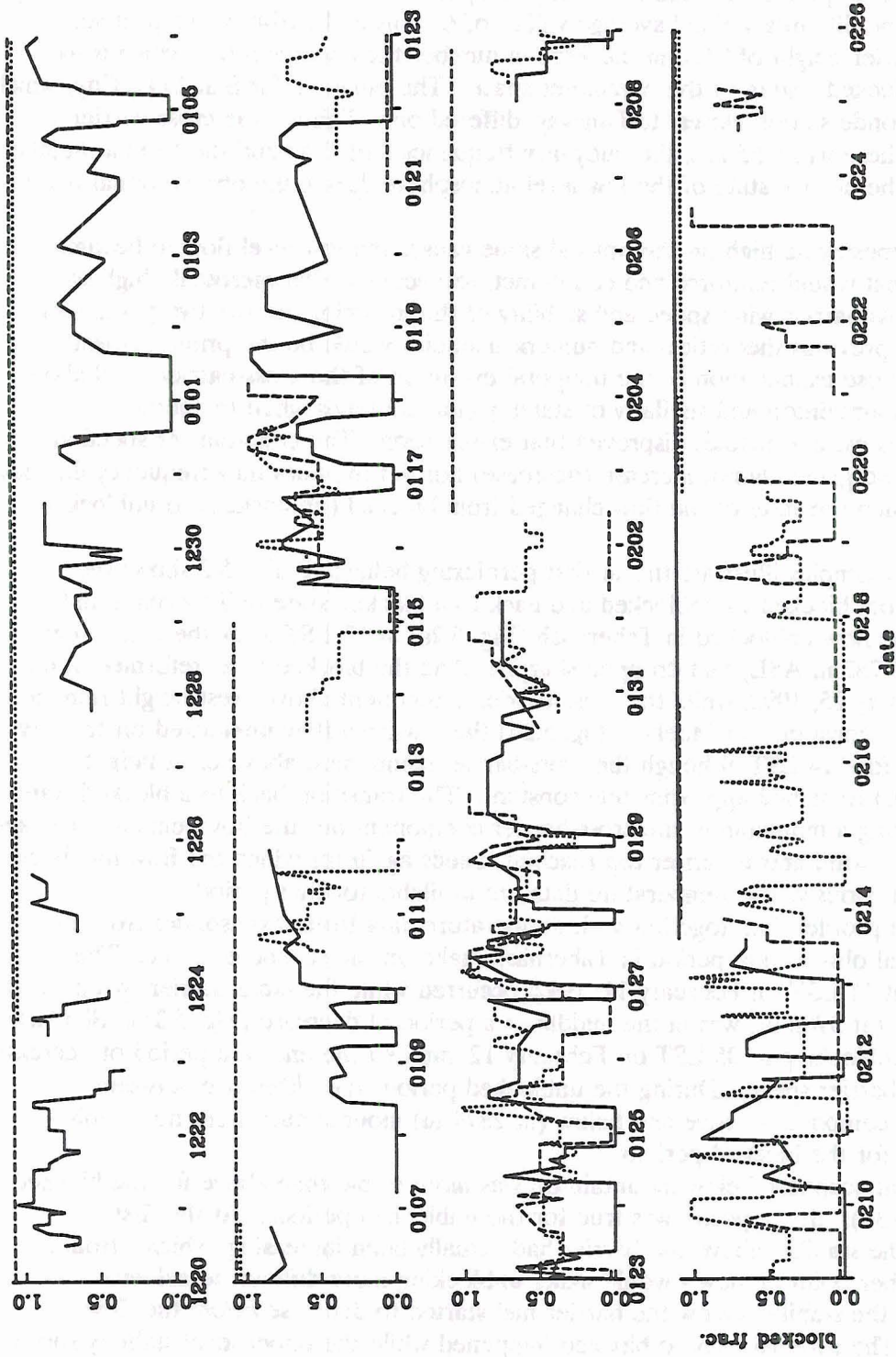


Fig. 5.1: Time series of the depth of the blocked layer as fraction of the blocked layer for Tabernash (solid), Meeker (dashed) and Dugway (dotted). A break in the line means no westerly wind of at least 2 m/s between mountain top and 500 hPa. A horizontal line above 1 denotes missing data. Unblocked periods in Meeker and Dugway are slightly offset from zero for better legibility of the graph. Dates (in months and days) are relative to UTC, which is 7 hours ahead of the local time.

A climatology of the cross-barrier component at crest height and buoyancy frequency below from the rawinsoundings in Grand Junction for those soundings during the observational period that had a westerly component of at least 2 m/s between average barrier top and 500 hPa yielded average values of 6.3 m/s and 0.0149 s^{-1} , respectively. With the barrier height of 2100 m the Froude number then becomes 0.2, which is well within the blocked region of the parameter space. The numbers for Salt Lake City, which is the rawinsonde station closest to Dugway, differed only slightly: the cross-barrier component there was 6.55 m/s, the buoyancy frequency 0.0153 s^{-1} and the Froude number 0.19. Thus the normal state of the low-level atmosphere during the observational period was blocked.

The mesoscale high on the upwind slope causes the low-level flow to become blocked. What would reinforce and counteract, respectively, that mesoscale high so rapidly? Cross-barrier wind speed and stability of the incoming air, the two parameters examined by previous theoretical and numerical studies would be the prime suspects. However, a close examination of the temporal evolution of the cross-barrier wind above and below mountaintop and similarly of stability (for the times when temperature measurements were available) disproved that explanation. The cross-barrier speed above crest height did generally not increase (decrease) nor did the buoyancy frequency decrease (increase) when the state of the flow changed from blocked (unblocked) to unblocked (blocked).

Two examples illustrate this at first perplexing behavior: Fig. 5.2 shows the transitions from blocked to unblocked and back to a blocked state in Tabernash and Meeker. The flow unblocked in Tabernash (Fig. 5.2a) at 13 LST after the wind above barrier top (3782 m ASL) had dropped sharply! And the blocked layer reformed at 02 LST on January 25, 1992, while the cross-barrier component above crest height remained approximately constant. In Meeker (Fig. 5.2b) the low-level flow unblocked on January 24 shortly before 14 LST although the cross-barrier component above crest height (4739 m ASL) remained approximately constant. The transition back to a blocked state occurred during a minimum in the cross-barrier component but the flow remained blocked even after the wind above barrier top reached speeds again for which the flow had been unblocked previously. No temperature data are available for that period.

Wind profiler data together with temperature data from rawinsondes from the second special observation period in Tabernash make up the second example. The first unblocking at 11 LST on February 11, 1992, occurred while the cross-barrier speed above mountaintop (at 3782 m) was in the middle of a period of decrease (Fig. 5.3a). Similarly, the second unblocking at 05 LST on February 12, marked the end of a period of decrease of the cross-barrier speed. During the unblocked periods the difference between the cross-barrier component above and below (at 2874 m) mountaintop were noticeably smaller than for the blocked periods.

The atmosphere below mountaintop was more stable than above for the blocked times (Fig. 5.3b); the opposite was true for the unblocked periods. At the first unblocking the stability above the barrier had actually been increasing, which - from a Froude number point of view - would make unblocking more difficult to achieve. Interestingly the stability below the barrier had started to decrease *before* the flow unblocked. The reversal back to blocked happened while the upper level stability showed little change but *after* the low-level air had started to become more stable.

In chapter seven two mechanisms are proposed which are different from a change in stability or cross-barrier speed to modify the mesoscale high on the upwind slope. One

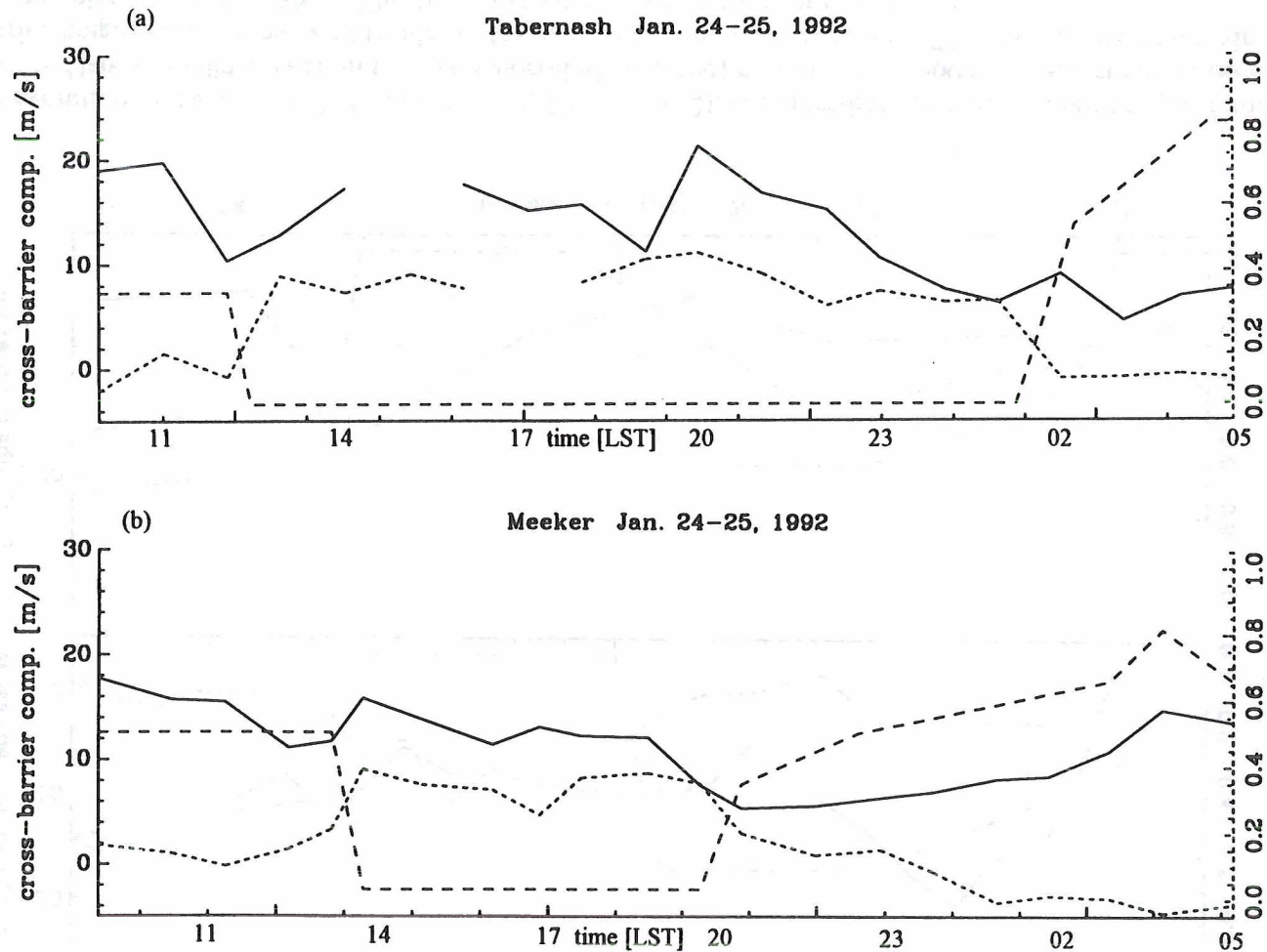


Fig. 5.2: Cross-barrier wind speed above (solid curve) and below (short dashes) mountaintop (3600 m ASL) in (a) Tabernash and (b) Meeker, superimposed on the fraction of the barrier height that was blocked (scale on the right side; long-dashed curve) on January 24 - 25, 1992. The gate above mountaintop is at 3782 m ASL in Tabernash and at 4739 m ASL in Meeker; the one below at 2772 m ASL in Tabernash and at 2874 m ASL. The time is in hours relative to local time [LST].

Tabernash Feb. 11-12, 1992

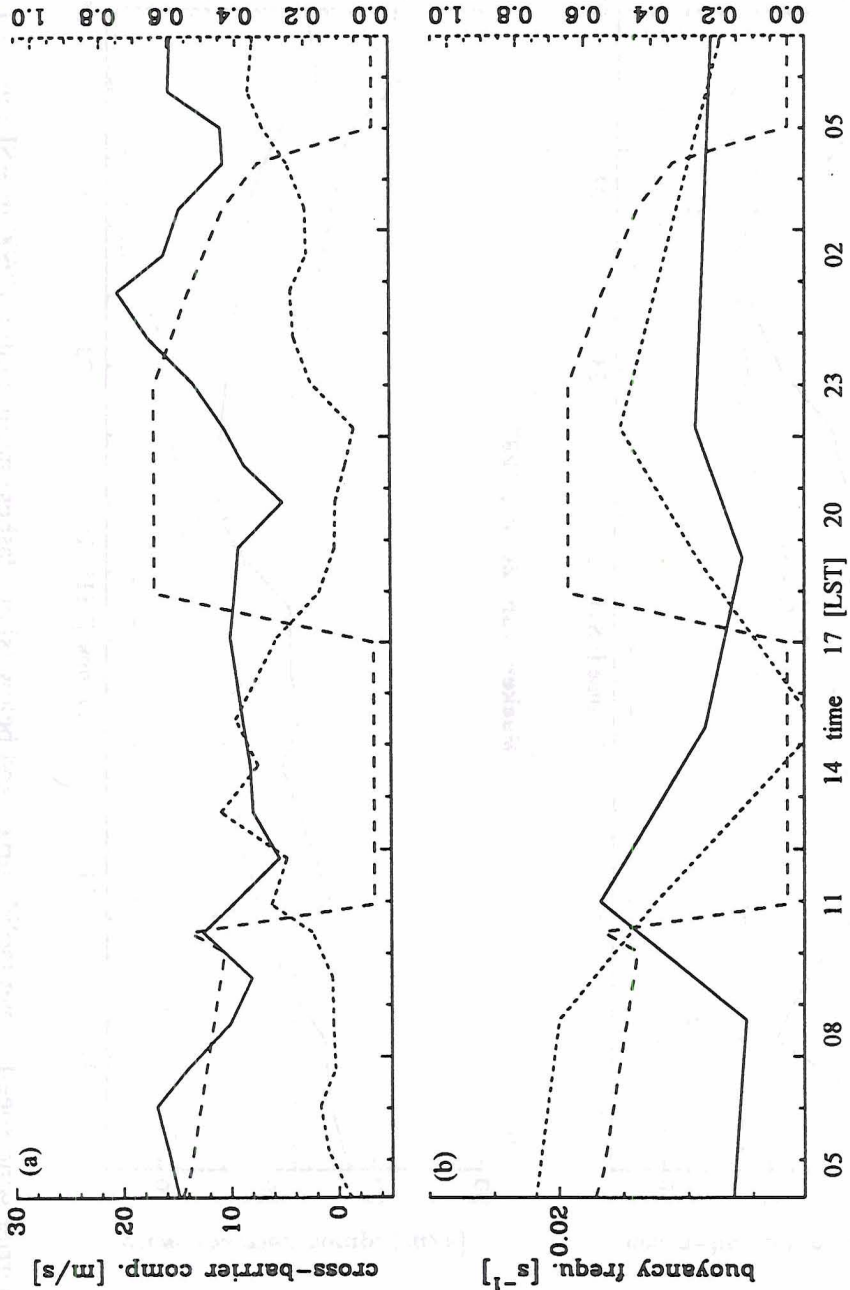


Fig. 5.3: Blocking evolution in Tabernash, February 11 - 12, 1992 (SOP 2): (a) cross-barrier wind component [m/s] and (b) buoyancy frequency [s⁻¹] above (solid curve) and below (short-dashed curve) mountaintop (3600 m ASL) superimposed on the fraction of the barrier height that was blocked (scale on the right side; long-dashed curve). The level above mountaintop is at 3782 m ASL, the one below at 2772 m ASL. The time is in hours relative to local time [LST].

will explain the unblocking events on January 24-25, 1992 (Fig 5.2), the other the events on February 11-12, 1992 (Fig. 5.3).

5.2 Vertical structure of horizontal wind field

Did the vertical profile of the horizontal wind indeed fall into three categories: blocked, unblocked with westerlies above and unblocked without westerlies as the previous discussion indicates? This section seeks an answer to that question by looking at scatterplots of the whole data set in section 5.2.1 and wind matrices in section 5.2.2.

5.2.1 Scatterplots

The first exploration of the profiler data is with scatterplots of wind direction, cross-barrier component, and along-barrier component, respectively, at a reference gate above barrier height versus a lower gate affected by blocking. Whiteman and Doran (1993) also used this method to deduce the coupling between the flows in a valley and aloft. Since the wind measured above the mountain range is not slowed down by blocking this method allows a first look at the effects of blocking. Marginal distributions, i.e. the frequency of a certain direction or speed at one gate independent of the values at the other gate, are included at each gate for additional information. The scatterplots encompass data from all the individual soundings taken every few minutes. Wind direction plots span from 0° to 450° for better readability (data from 360° to 450° are identical to the ones from 0° to 90°). To remove the ground clutter from the profiler data, the data within a small window around zero radial velocity was ignored, which accounts for the missing directions (0° , 90° , 180° , and 270°) and speeds ($u = 0$, $v = 0$) in the scatterplots.

5.2.1.1 Tabernash

Due to the lower height coverage of the NOAA profiler, gate 9 at 3580 m ASL had to serve as reference gate. This is unfortunately only at the average barrier height.

a) wind direction

Fig 5.4a shows scatterplots of wind direction for gate 1 at 2772 m ASL versus the wind direction at the reference gate. At the "undisturbed" level (gate 9) the wind blew mostly from the SW to N with a maximum at WNW while the lower-level wind covered the whole wind rose. Yet there are two distinct clusters: one in a narrow range around SE and the other more spread out at W. The first indicates a reversal in flow direction relative to the reference gate and belongs to the blocked flow situations. The second shows only a slight turning of the wind with height characteristic of unblocked flow. Less pronounced but still visible are the times without a strong westerly component above the barrier when the flow there was from the NE to SE with a low-level wind from the SE.

b) cross-barrier component

The cross-barrier component spread over a wide range of speeds at the reference gate but remained centered around zero at gate 1 (Fig. 5.4b). Blocked flow situations

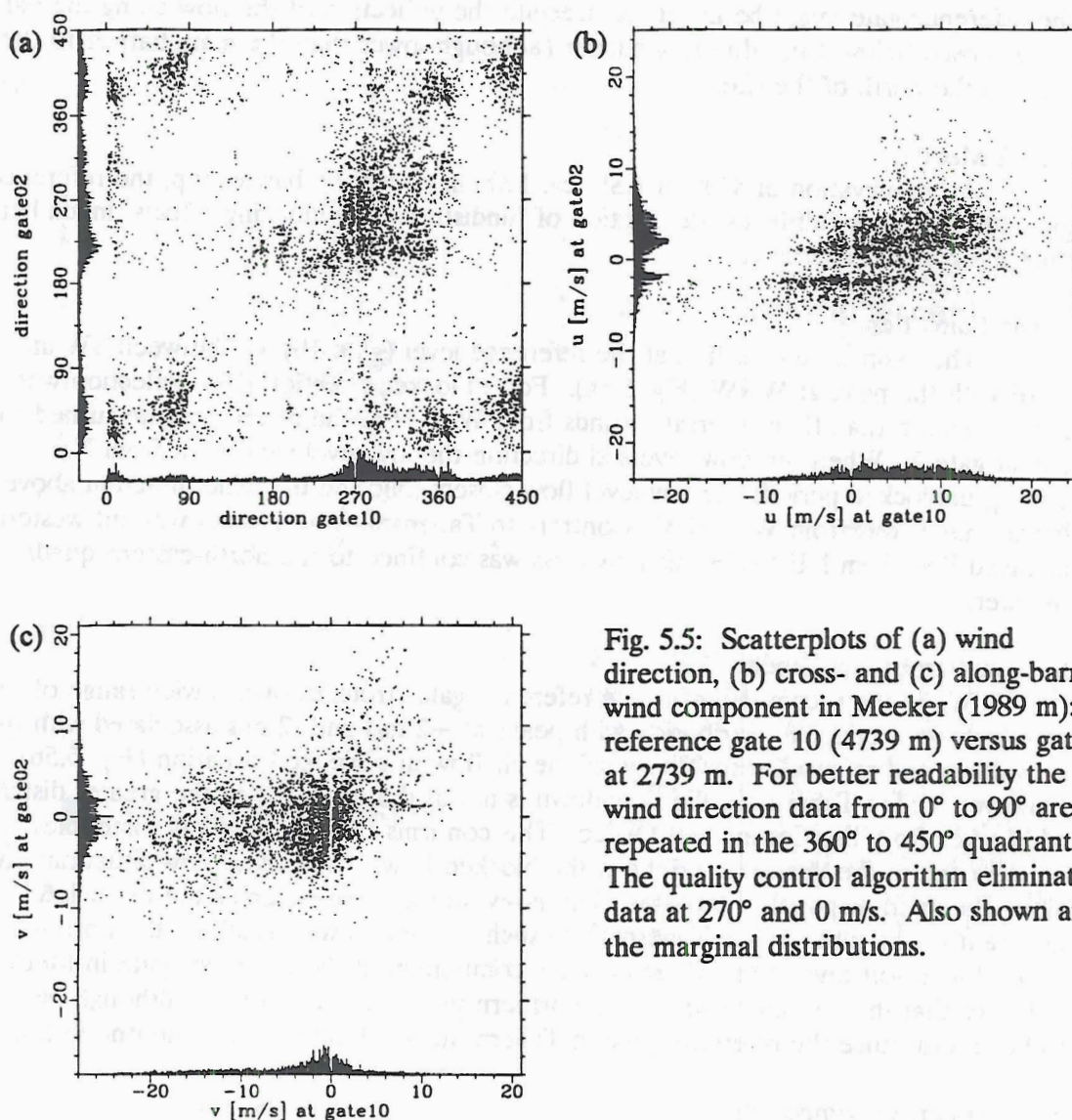


Fig. 5.5: Scatterplots of (a) wind direction, (b) cross- and (c) along-barrier wind component in Meeker (1989 m): reference gate 10 (4739 m) versus gate 2 at 2739 m. For better readability the wind direction data from 0° to 90° are repeated in the 360° to 450° quadrant. The quality control algorithm eliminated data at 270° and 0 m/s. Also shown are the marginal distributions.

proximity to the Wasatch Mountains instigated a sizeable number of blocked flow situations. For gate two the most common wind direction was SSE, i.e. a flow reversal! The second maximum lay at SSW indicative of a deflection of the predominantly westerly flow.

b) cross-barrier component

The scatterplot of the cross-barrier wind component (Fig. 5.6b) resembles the one in Tabernash. For a wide range of positive u at the reference gate the cross-barrier component at gate 2 was either slightly positive (flow deflection) or negative (flow reversal). The second biggest group contained the no-westerly situations and only few data points cluster close to the main diagonal indicating the rarity of unblocked situations.

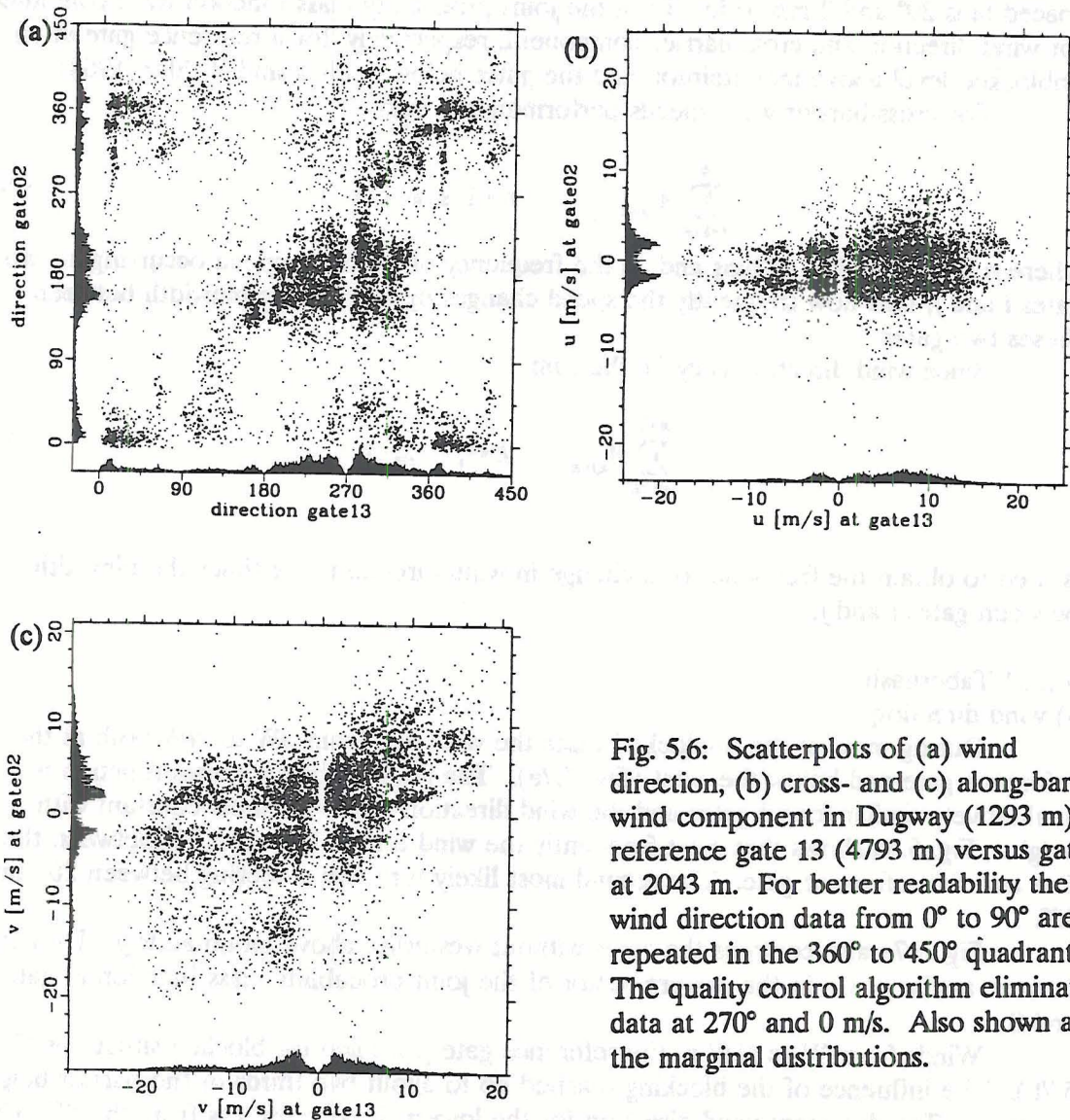


Fig. 5.6: Scatterplots of (a) wind direction, (b) cross- and (c) along-barrier wind component in Dugway (1293 m): reference gate 13 (4793 m) versus gate 2 at 2043 m. For better readability the wind direction data from 0° to 90° are repeated in the 360° to 450° quadrant. The quality control algorithm eliminated data at 270° and 0 m/s. Also shown are the marginal distributions.

c) along-barrier component

Unlike Tabernash and Meeker, the v -components are evenly distributed around zero at the reference gate (Fig 5.6c). At gate 2, however, positive along-barrier flow prevailed even with northerly reference winds, indicating again the northward deflection along the barrier of the incoming flow.

5.2.2 Wind matrices

After looking qualitatively at all the data comprised of blocked, unblocked, and no-westerlies situations by using scatterplots in section 5.2.1, the blocked and unblocked situations will now be examined separately.

Wind directions and cross-barrier speeds were divided, respectively, into equally spaced bins 20° and 2 m/s wide. Then the joint probability mass function were computed for wind direction and cross-barrier component, respectively, for a reference gate at an unblocked level above mountaintop and the gates below (Cehak and Pichler, 1968).

For cross-barrier wind speeds performing the sum

$$\sum_{i=1+k}^n A_{ij-k} \quad -n+1 \leq k \leq n-1 \quad (5.1)$$

where n is the number of bins and A_{ij} the frequency of a certain speed occurring at two gates i and j , tells how frequently the speed changes by k times the binwidth between these two gates

Since wind direction is cyclic the sum

$$\sum_{i=1+k}^{n+k} A_{ij-k} \quad k=1, \dots, n-1 \quad (5.2)$$

is used to obtain the frequency of a change in wind direction by k times the binwidth between gates i and j .

5.2.2.1 Tabernash

a) wind direction

During most of the unblocked cases the wind was from SW to NW both at the reference gate and below the crest (Fig. 5.7a). The joint probability mass function is qualitatively similar for all gates and the wind direction remains almost constant with height. Fig. 5.8a shows that most frequently the wind turned less than 20° between the first and the reference gate. The second most likely turn was a veering between 20° and 40° .

Fig. 5.7a also contains the cases without westerlies above mountaintop. They can be seen as the peaks in the eastern sector of the joint probability mass function at gates 7 and 8.

Winds from W to NW at the reference gate prevailed for blocked situations (Fig. 5.7b). The influence of the blocking reached up to about two thirds of the barrier height to gate 5. The dominant wind direction for the lowest three gates was from the SE, which means that a flow reversal was more likely than a flow deflection. At gate 4 both situations were equally likely and at gate 5 flow deflection occurred more frequently than a reversal. Fig. 5.8b emphasizes these conclusions: The wind generally veered between the lowest four gates and the reference gate with a maximum turning of 160° ! Only from gate 5 upwards was a slight veering of 0° to 40° the most likely scenario.

b) cross-barrier wind speed

The cross-barrier components at the reference and lower gates show an approximately linear relationship for the unblocked cases (Fig. 5.9a). When no westerlies were present above mountaintop the wind speeds were usually slow, so that the simultaneous occurrence of cross-barrier components between 1 and -1 m/s at the reference gate 9 and lower gates was most likely. Easterly flow at all gates also occurred.

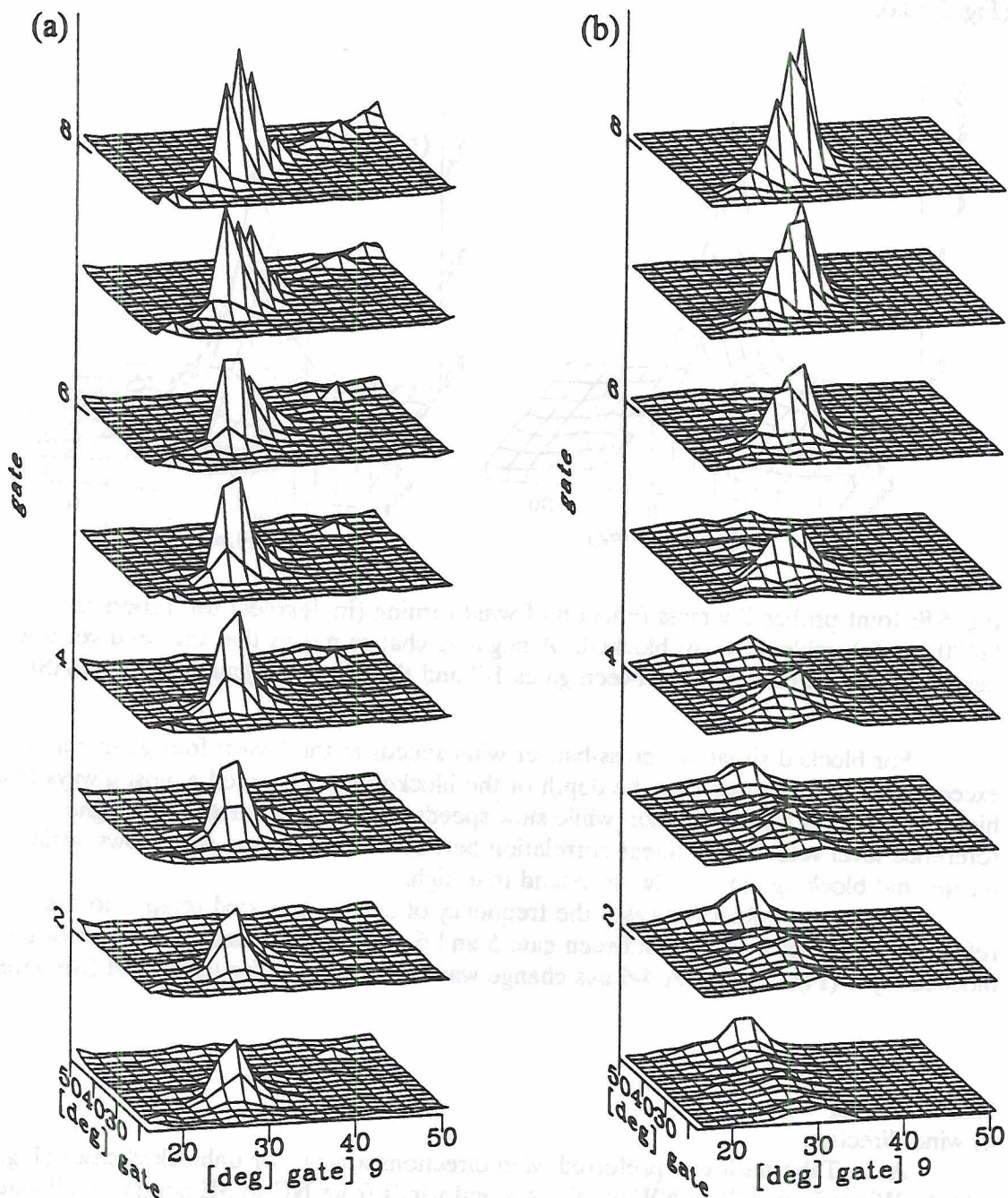


Fig. 5.7: Joint probability mass functions for wind direction at reference gate 9 (3580 m ASL) and lower gates for Tabernash (2620 m): (a) unblocked, (b) blocked. For better readability the wind direction data from 0° to 90° are repeated in the 360° to 450° quadrant; numbers on plot are multiples of 10° . The vertical distance between two gates is equivalent to a joint probability of 15%.

The winds did most frequently not speed up from the lowest to the reference gates (Fig. 5.10a).

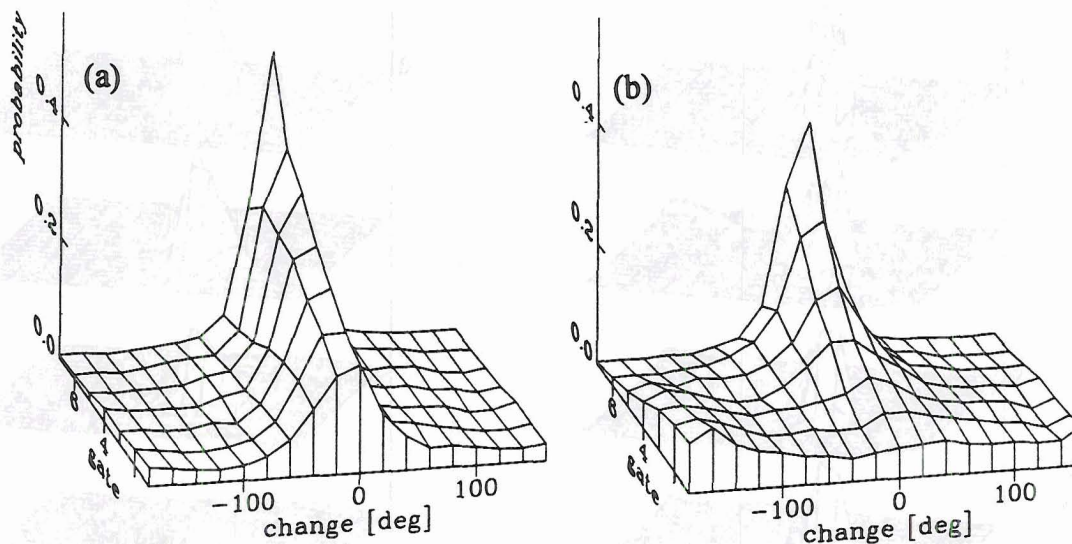


Fig. 5.8: Joint probability mass function of wind turning (in degrees) for Tabernash (2620 m): (a) unblocked, (b) blocked. A negative change means that the wind veers with height (ie rotates clockwise) between gates 1-7 and the reference gate 9 (3580 m ASL).

For blocked situations cross-barrier wind speeds at the lowest four gates rarely exceeded 4 m/s indicating that the depth of the blocked layer reached almost always that high. Gate 5 is a transitory one: while slow speeds there still occurred with higher reference level velocities, a linear correlation between the two gates also shows, which means that blocking did not always extend that high.

Unlike the unblocked cases the frequency of change of speed relative to the reference gate shows a break between gate 5 and 6 marking the maximum extent of the blocked layer (Fig. 5.10b). A 4-6 m/s change was most common for the lowest five gates.

5.2.2.2 Meeker

a) wind direction

As in Tabernash two preferred wind directions appear for unblocked cases (Fig. 5.11a). Winds from SW to NW at all gates and winds from NE to SE appear at all gates, the latter of which were excluded in the definition of blocking. Wind dominantly veered with height between the lowest gates and the reference gate but backing also occurred (Fig. 5.12a). The most common turning angle was 40°.

The predominant wind direction for the blocked cases was NW, which was more northerly than for the unblocked ones. As in Tabernash the depth of the blocked layer reached on the average to two thirds of the barrier depth (gate 4). The joint probability plot (Fig. 5.11b) for gate 1 versus reference gate shows two peaks for a primarily NW wind at the reference gate: SW indicative of low-level flow deflection towards the north,

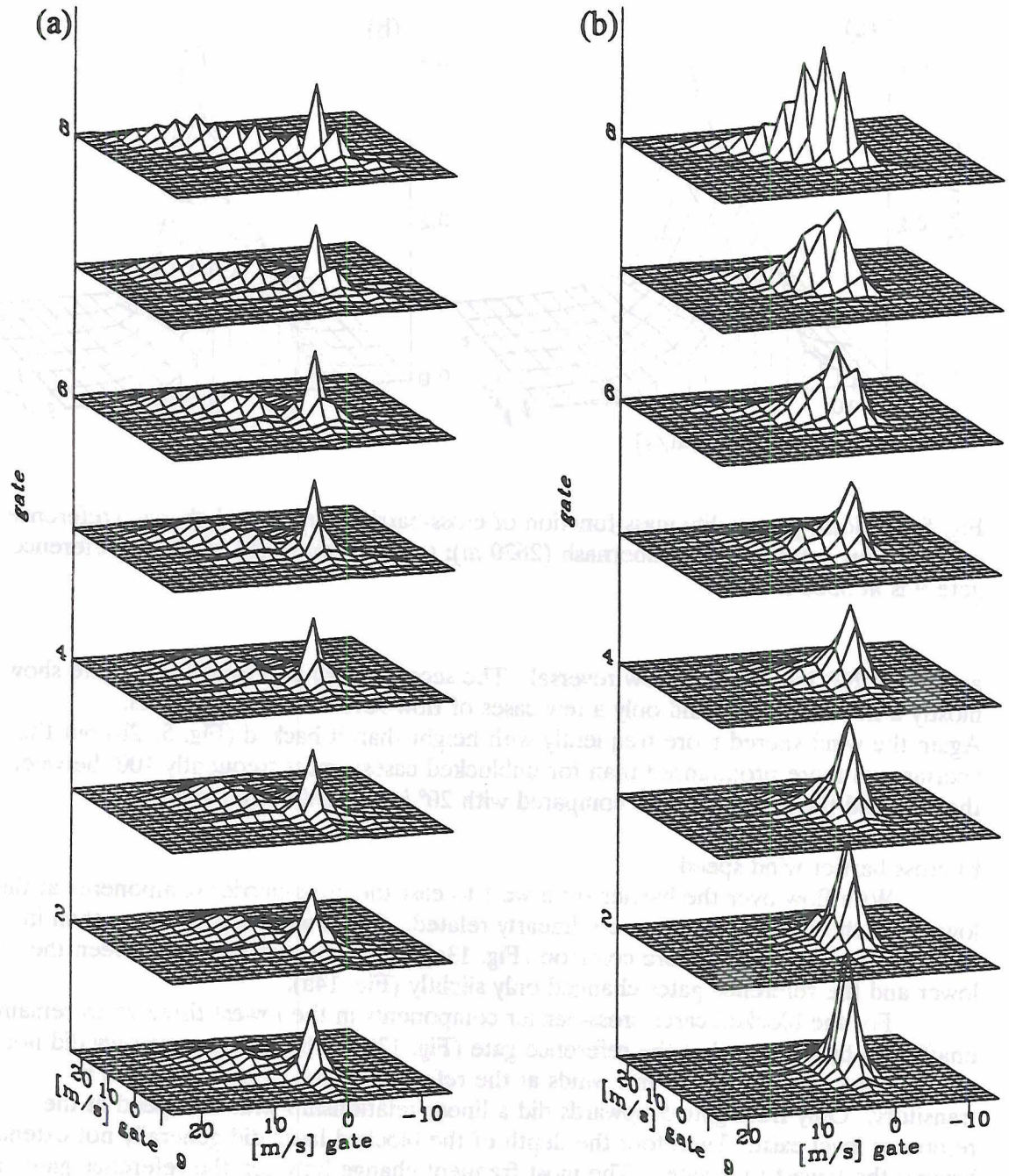


Fig. 5.9: Joint probability mass functions for cross-barrier wind component at reference gate 9 (3580 m ASL) and lower gates for Tabernash (2620 m): (a) unblocked, (b) blocked. The vertical distance between two gates is equivalent to a joint probability of 15%.

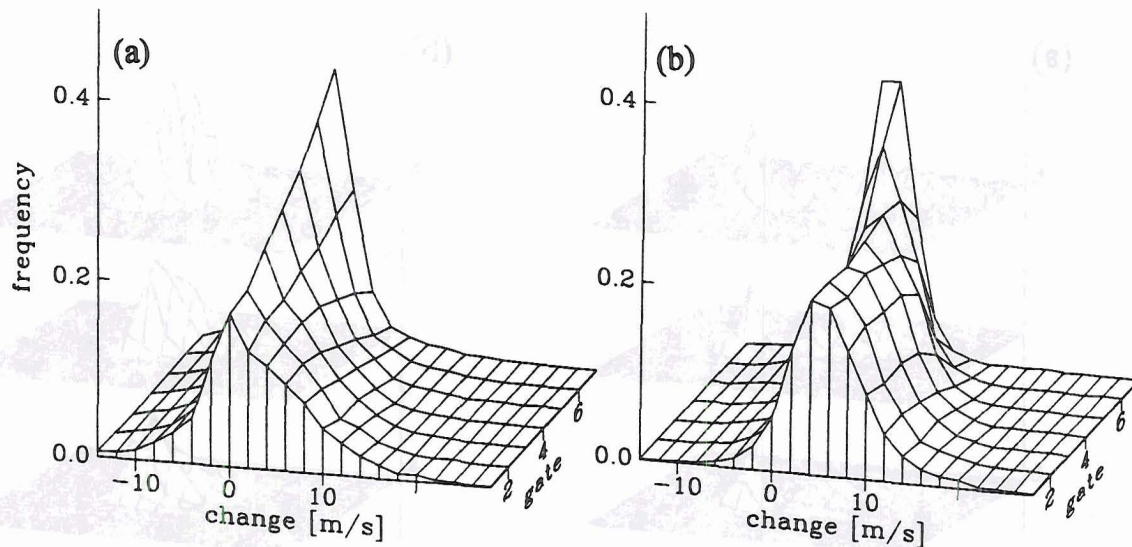


Fig. 5.10: Joint probability mass function of cross-barrier wind speed change (reference gate 9 minus gates 1-7) for Tabernash (2620 m): (a) unblocked, (b) blocked; reference gate 9 is at 3580 m ASL.

and SE to NE indicative of flow reversal. The second, third and fourth third gate show mostly a flow deflection and only a few cases of flow reversal with NE winds. Again the wind veered more frequently with height than it backed (Fig. 5.12b) but the veering was more pronounced than for unblocked cases: most frequently 100° between the first and the reference gate compared with 20° in the unblocked situations.

b) cross-barrier wind speed

With flow over the barrier from west to east the cross-barrier components at the lower and the reference gates were linearly related. Calms were less frequent than in Tabernash but easterlies more common (Fig. 13a). Cross-barrier speeds between the lower and the reference gates changed only slightly (Fig. 14a).

For the blocked cases cross-barrier components in the lowest three gates remained unaffected by the speed at the reference gate (Fig. 13b). They most commonly did not exceed 4 m/s despite 15 - 20 m/s winds at the reference level. The fourth gate is transitory. Only from gate 5 upwards did a linear relationship with the speed at the reference level exist. Therefore the depth of the blocked layer did generally not extend beyond the lowest four gates. The most frequent change between the reference gate and the lowest three was by 8-10 m/s (Fig. 5.14b).

5.2.2.3 Dugway

a) wind direction

With the exception of the lowest gate where winds from the south persisted for winds at reference level from SW to NW, the directions at reference and lower levels were quite similar for the unblocked cases (Fig 5.15a). The probability mass function for the turning of the wind with height (Fig. 5.16a) confirms that conclusion. From gate 3

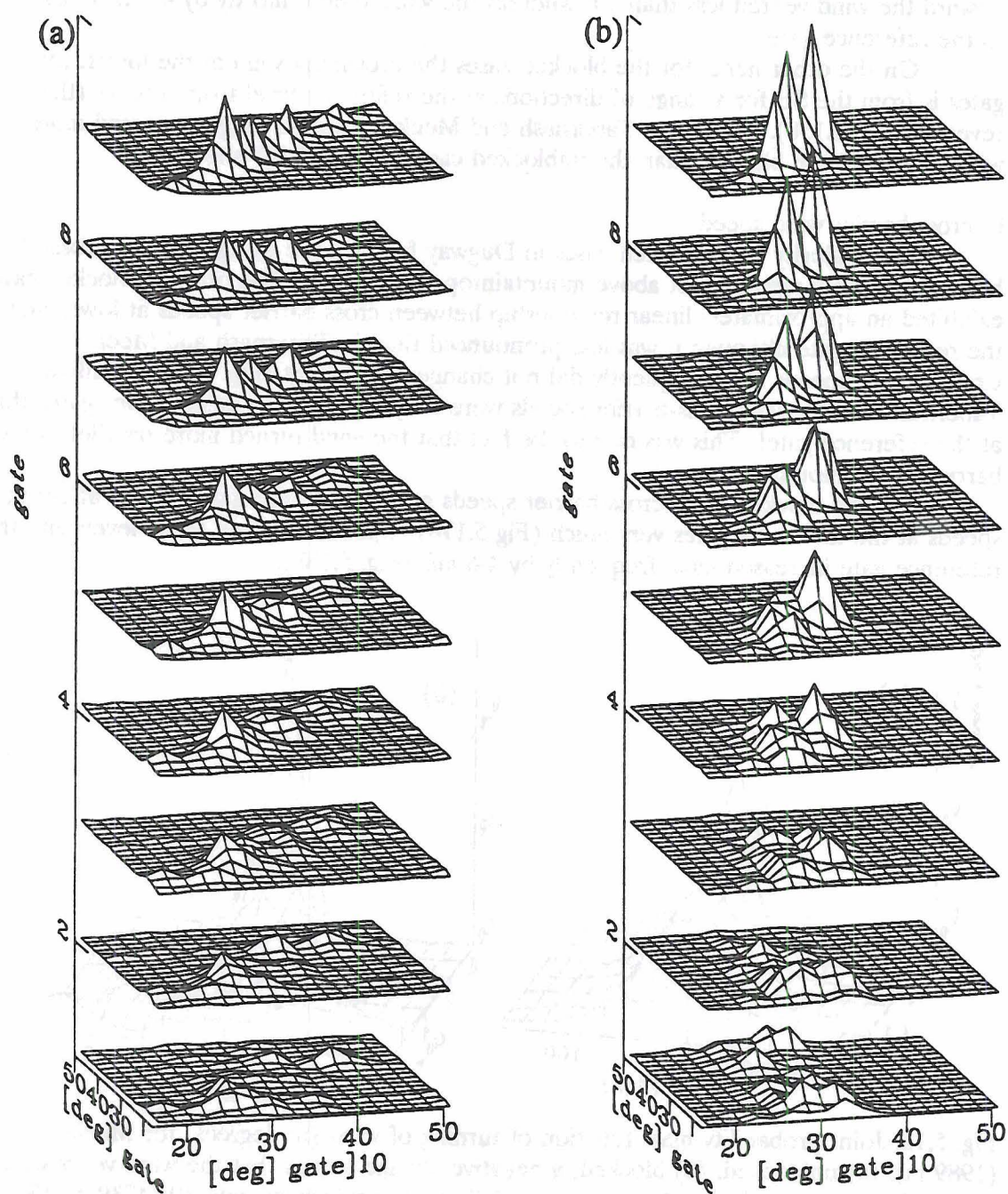


Fig. 5.11: Joint probability mass function for wind direction at reference gate 10 (4739 m ASL) and lower gates for Meeker (1989 m): (a) unblocked, (b) blocked. For better readability the wind direction data from 0° to 90° are repeated in the 360° to 450° quadrant; numbers on plot are multiples of 10° . The vertical distance between two gates is equivalent to a joint probability of 15%.

upward the wind veered less than 20° whereas the wind veered mostly by 40° from gate 1 to the reference gate.

On the other hand, for the blocked cases the prevailing wind at the lowest four gates is from the SE for a range of directions at the reference level from S to W (flow reversal) (Fig 5.15b). Similar to Tabernash and Meeker, wind in Dugway veered more with height for the blocked than the unblocked cases, as Fig. 5.16b shows.

b) cross-barrier wind speed

The majority of unblocked cases in Dugway fell into the category of no cross-barrier flow from west to east above mountaintop (Fig. 5.17a). The other unblocked cases exhibited an approximately linear relationship between cross-barrier speeds at lower and the reference gate although it was less pronounced than in Tabernash and Meeker. Cross-barrier speeds most frequently did not change with height (Fig. 5.18a). Unlike Tabernash and Meeker cross-barrier speeds were frequently higher at the lower gates than at the reference gate! This was due to the fact that the wind turned more parallel to the barrier above mountaintop.

For the blocked cases cross-barrier speeds at the reference gate did not affect the speeds at the lowest six gates very much (Fig 5.17b). Speeds between these levels and the reference gate increased most frequently by 4-6 m/s (Fig. 5.18b).

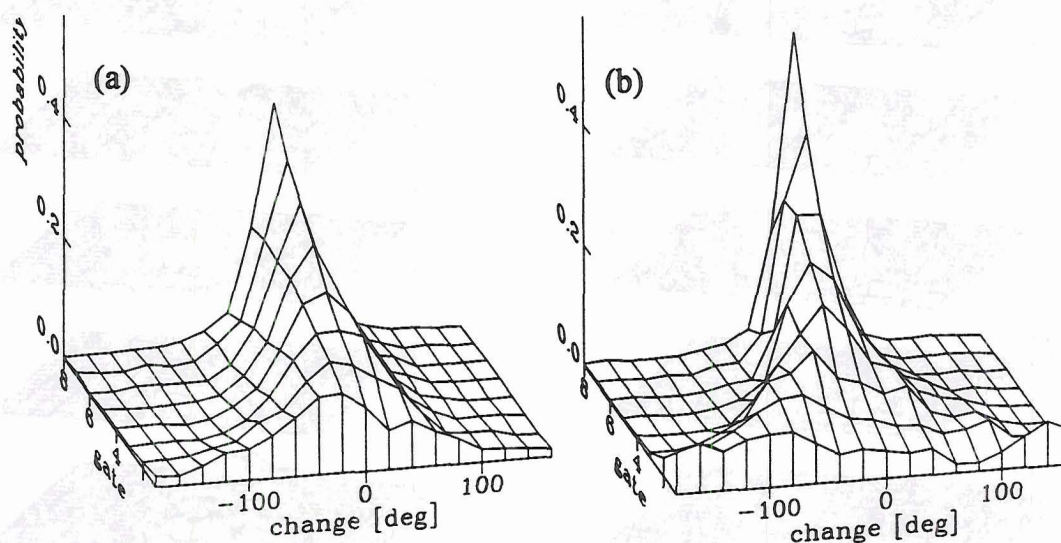


Fig. 5.12: Joint probability mass function of turning of wind (in degrees) for Meeker (1989 m): (a) unblocked, (b) blocked; a negative change means that the wind veers with height (ie rotates clockwise) between gates 1-8 and the reference gate 10 (4739 m ASL).

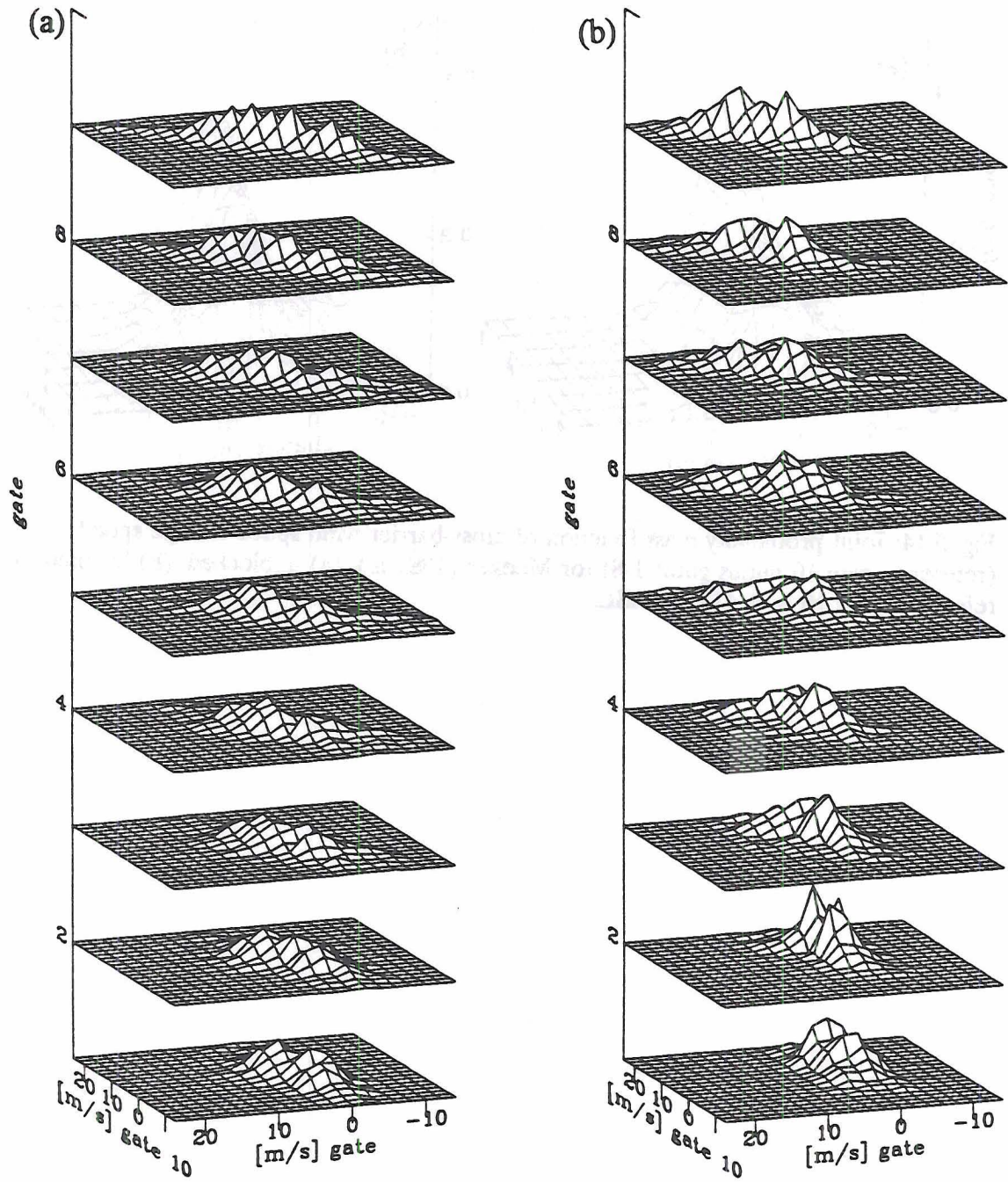


Fig. 5.13: Joint probability mass function for wind speed at reference gate 10 (4739 m ASL) and lower gates for Meeker (1989 m): (a) unblocked, (b) blocked. The vertical distance between two gates is equivalent to a joint probability of 15%.

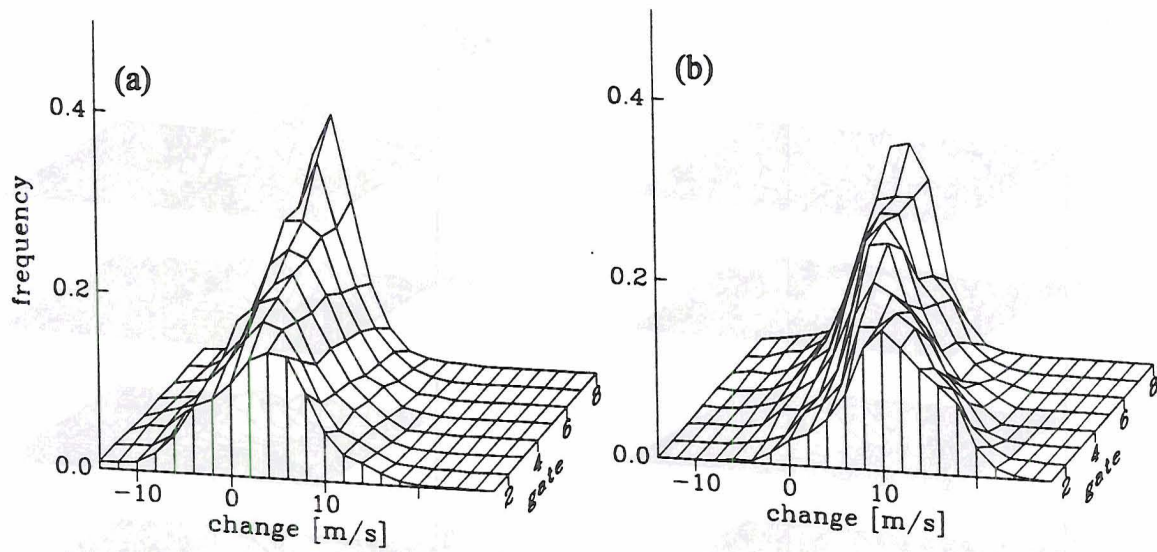


Fig. 5.14: Joint probability mass function of cross-barrier wind speed change speed (reference gate 10 minus gates 1-8) for Meeker (1989 m): (a) unblocked, (b) blocked; the reference gate 10 is at 4739 m ASL.

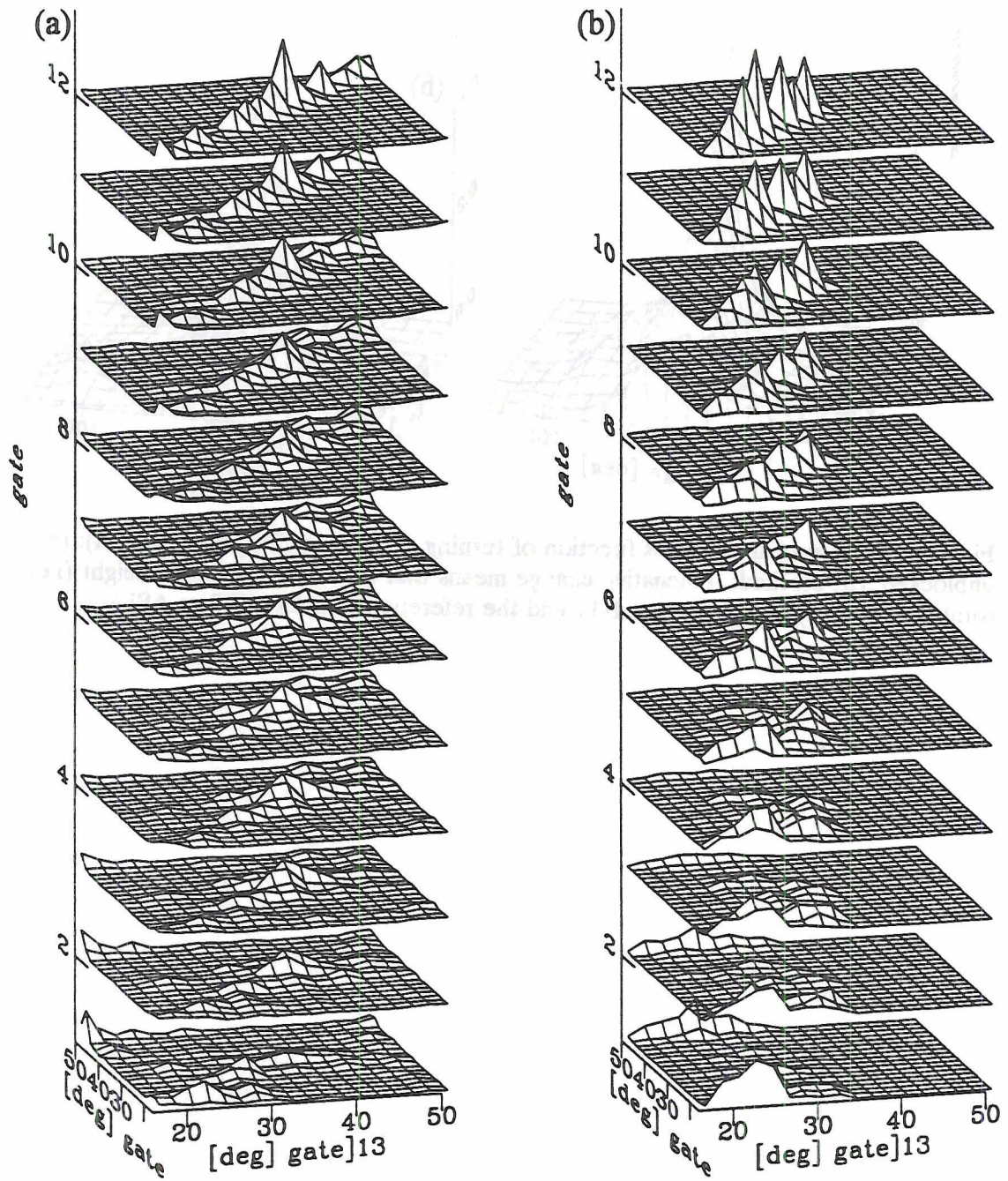


Fig. 5.15: Joint probability mass function for wind direction at reference gate 13 (4793 m ASL) and lower gates for Dugway (1293 m): (a) unblocked, (b) blocked. For better readability the wind direction data from 0° to 90° are repeated in the 360° to 450° quadrant; numbers on plot are multiples of 10° . The vertical distance between two gates is equivalent to a joint probability of 15%.

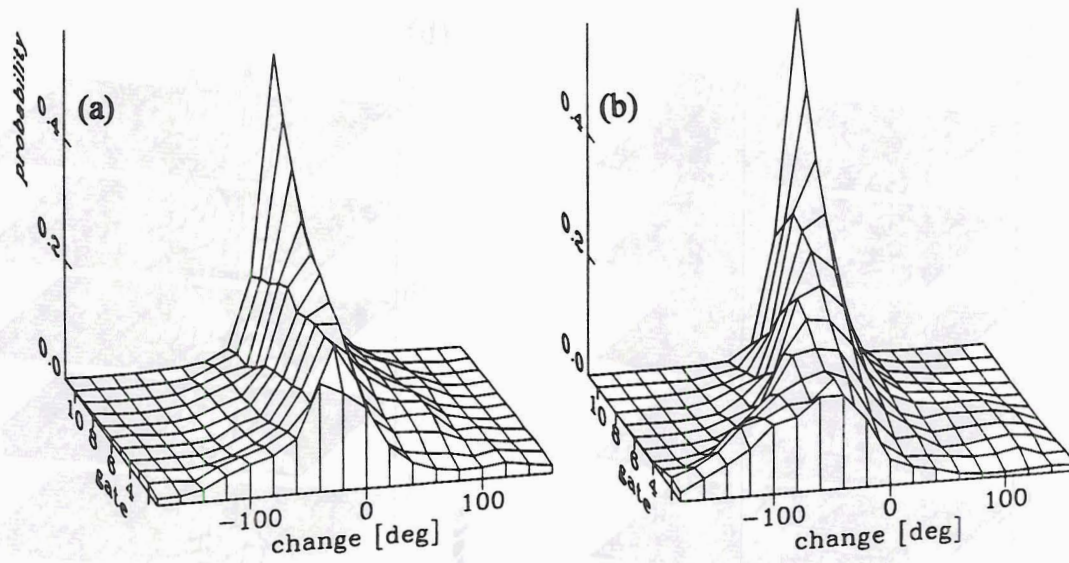


Fig. 5.16: Joint probability mass function of turning of wind for Dugway (1293 m): (a) unblocked, (b) blocked; a negative change means that the wind veers with height (i.e. rotates clockwise) between gates 1-11 and the reference gate 13 (4793 m ASL).

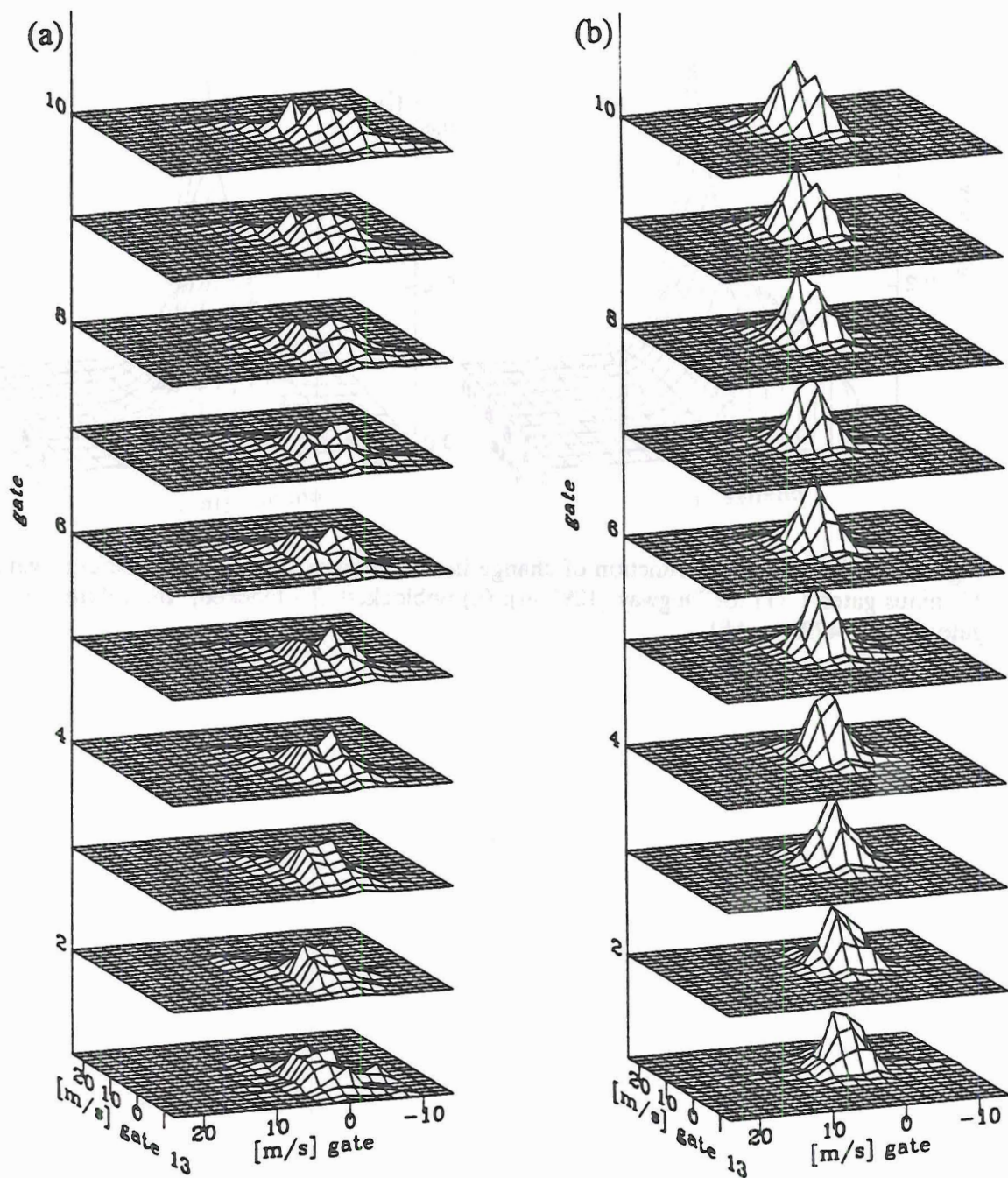


Fig. 5.17: Joint probability mass function for cross-barrier wind speed at reference gate 13 (4793 m ASL) and lower gates for Dugway (1293 m): (a) unblocked, (b) blocked. The vertical distance between two gates is equivalent to a joint probability of 15%.

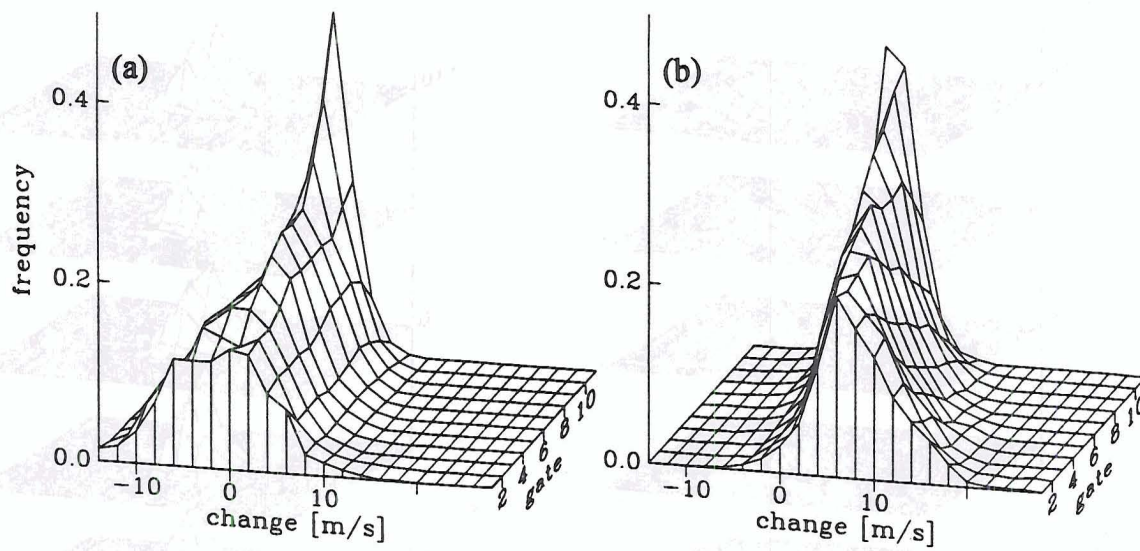


Fig. 5.18: Joint probability function of change in cross-barrier wind speed (reference gate 13 minus gates 1-11) for Dugway (1293 m): (a) unblocked, (b) blocked; the reference gate 13 is at 4793 m ASL.

6

Modeling results

Observation of the wind field at three locations over two months allows some deductions about but not necessarily full understanding of the physical processes underlying the evolution of blocking. Numerical models, on the other hand, provide the possibility to specify boundary and initial conditions, to test the sensitivity of the flow to a change of a certain parameter, and to look at all the variables at any grid point at any time.

Admittedly this case with its steep, highly three-dimensional topography extending over a huge area, stretches present-day models and computer power to the limits, so that for now simplified numerical simulations will be used.

6.1 Model description

Version 2c of Colorado State's Regional Atmospheric Modeling System (RAMS) described by Pielke et al. (1992) was used. The previously mentioned simplifications consisted of neglecting radiation, moist processes and soil processes, and using homogeneous initial fields. A Klemp-Wilhelmson scheme handled the lateral boundary condition. To suppress reflections of gravity waves from the rigid top a Rayleigh friction layer as upper boundary was used for the model. A second order leapfrog scheme calculates horizontal and a second order forward scheme vertical advection. The horizontal subgrid scale turbulence closure is local and of first order (K-theory). The vertical closure is more elaborate and of order 2.5 for decaying and of order 2 for growing turbulence (Helfand and Labraga, 1988). This scheme permits realistic vertical mixing due to shear in stably stratified atmospheres.

6.1.1 Model domain and topography

A total of 67 grid points in the x-direction, 58 in the y-direction, and 37 vertical layers were included. The southwest corner of the grid was at 114.5°W, 36.4°N so that with a horizontal grid point distance of 15 km the grid stretches from southeast Nevada to the plains of Colorado and from the Colorado-New Mexico border to central Wyoming (Fig 3.1). The 37 vertical levels are 175 m apart up to 2100 m above the lowest model elevation; the distance between the levels widens then gradually until it reaches 1430 m at the highest level (16810 m AGL equivalent to 18245 m ASL).

How to best represent the subgrid-scale features of the topography is a difficult question. The silhouette averaging method described by Mesinger et al. (1988) was selected. By averaging elevations of several grid points from a high resolution topography database in a vertical plane one gets the average silhouette that an air parcel approaching from a direction perpendicular to the one of that averaging plane would "see". Since several preferred flow directions exist, averages are formed for differently orientated vertical planes and weighted for the final value.

Fig 6.1 shows the contours of the silhouette-averaged model topography. To avoid problems at the lateral boundaries the average grid elevation at the western and eastern boundaries was made equal and the jagged topography along the western boundary was

smoothed. The main topographic feature in the right half of the modeling domain, the Continental Divide, does not run exactly north-south. A wind from 295° will be perpendicular to it.

In addition to height contours Fig. 6.1 also shows the coordinate system and the bold line at $y = -112.5$ km marks the location of the vertical cross-section referred to in sections 6.2 and 6.3. The box upstream of the Continental Divide marks the horizontal cross-section referred to in section 6.3.

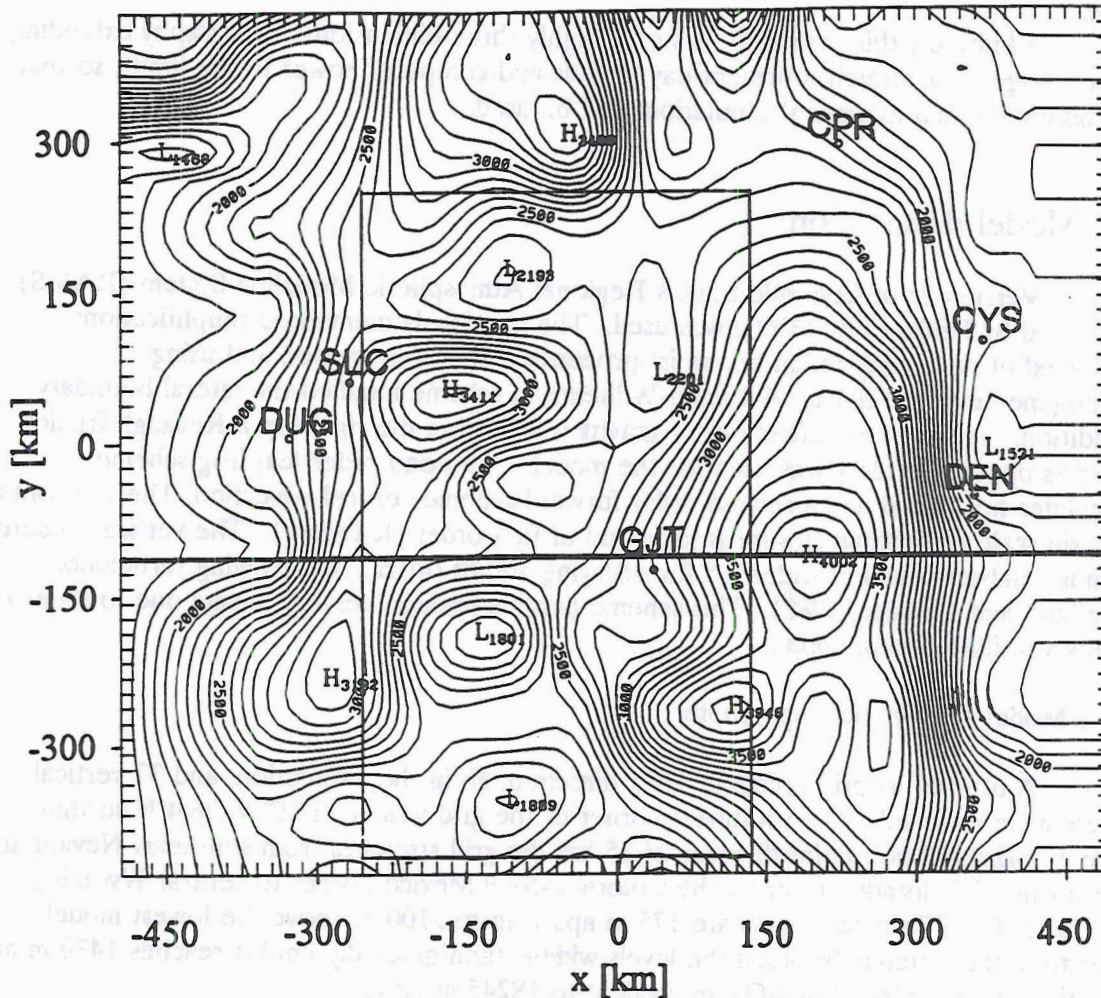


Fig. 6.1: Contours of topography and coordinate system used for the numerical simulations. Contour interval is 100 m; the height is relative to sea level. The vertical cross-section at $y = -112.5$ km referred to in section 6.2 is shown as a bold line as well as the sector of the domain for which horizontal cross-sections of perturbation Exner function are shown in section 6.3. The tick marks pointing inwards from the sides of the graph refer to the horizontal grid increments in the model. Salt Lake City (SLC), Dugway (DUG), Grand Junction (GJT), Denver (DEN), Cheyenne (CYS), and Casper (CPR) provide geographical orientation.

6.1.2 Model initialization

Wind and temperature were initialized to be horizontally homogeneous and the wind and buoyancy frequency to remain constant with height. Blocked ($Ro/Fr=2.3$) and unblocked ($Ro/Fr=0.8$) flow were simulated. Table 6.1 shows the initial values of various parameters.

Table 6.1: Initialization of simulations (U_{cross} is the cross-barrier component, γ the lapse rate $-dT/dz$).

parameter	blocked simulation	unblocked simulation
Ro/Fr	2.3	0.8
Ro	0.7	1.4
Fr	0.3	1.8
N	0.015 s ⁻¹	0.005 s ⁻¹
γ	3.66 K/km	9.1 K/km
speed	9 m/s	18 m/s
direction	270°	270°
U_{cross}	8.2	16.3

6.2 The role of Coriolis force

6.2.1 Non-rotating system

In this section the response of the initially uniform atmospheric flow to the topography in the absence of the Coriolis force is shown: vertical cross sections of potential temperature, u , and v along $y = -112.5$ km depict the evolution of the flow as time progresses from four to eight and 12 hours after model startup. The discussion will focus on the regions upstream of the barriers.

Fig. 6.2a is a cross-section of potential temperature four hours after the start of the numerical simulation. The two barriers, the Continental Divide (CD) and the Wasatch Mountains (WM), each trigger a gravity wave. These waves propagate upwards as can be seen from the upstream phase tilt of the wave troughs in the lee of the two barriers. The mountains also disturb the initially horizontal isentropes below the crest. They slope upwards from approximately the upwind foot of the barrier. Four hours later (Fig. 6.2b) this disturbance has moved upstream and left behind a region of decreased stability. The 282 K isentrope runs now horizontally and the isentropes above it begin their ascent already at $x \approx -200$ km. Another four hours later at $t=12$ hrs (Fig. 6.2c) the disturbance from the Continental Divide has reached the Wasatch Range and all but

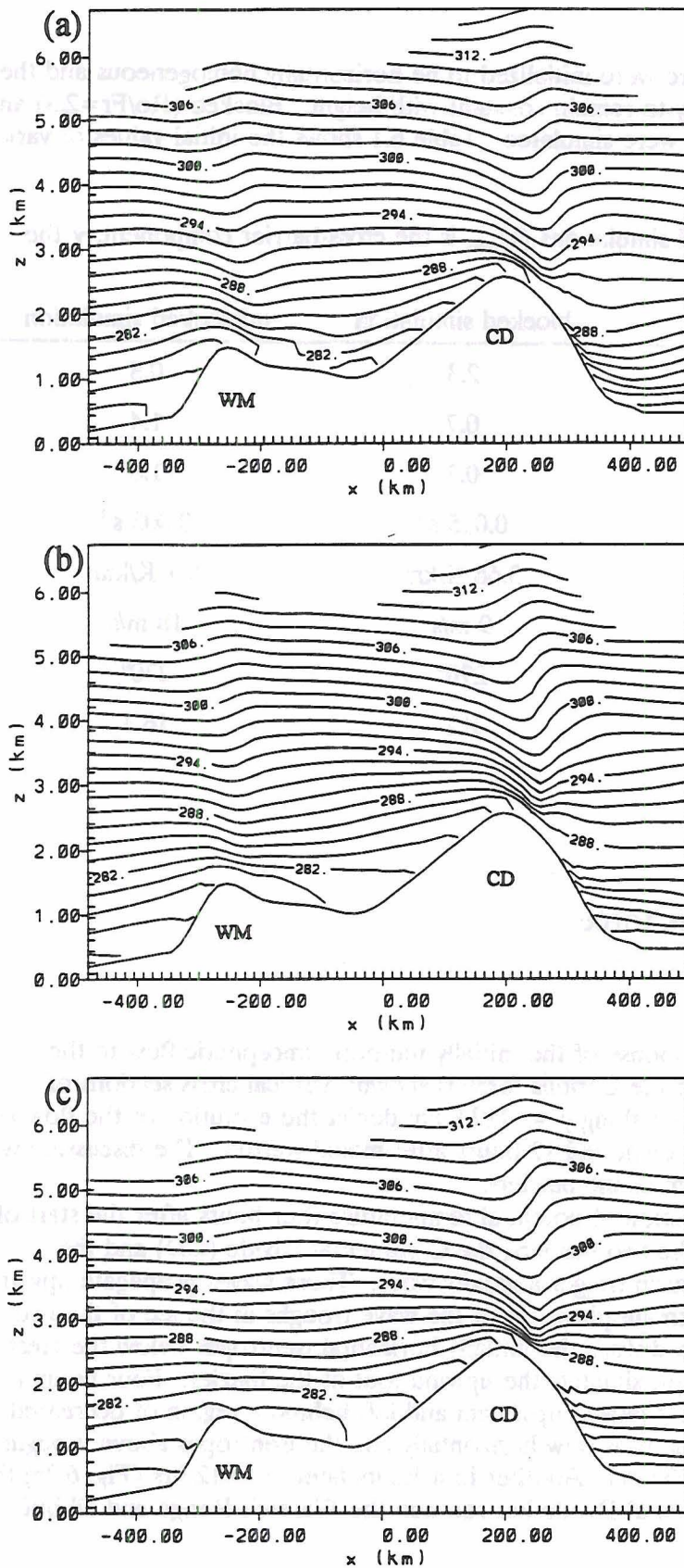


Fig. 6.2: Time series of potential temperature cross sections at $y = -112.5$ km (a) four, (b) eight, and (c) 12 hours after model start. Initialized with uniform flow of $u = 9$ m/s and $N = 0.015$ s $^{-1}$ (Froude number of 0.3, blocked) without Coriolis force.

eliminated the gravity wave there. The isentropes up to half of the height of the Continental Divide run almost horizontal now.

Fig. 6.3 shows how the topography modifies the cross-barrier wind component. Four hours after startup (Fig. 6.3a) a several hundred meter deep layer of decelerated flow (i.e. slower than the initial 9 m/s) follows the terrain from the lee of the Wasatch to the top of the Continental Divide. There is strong shear at the top of the decelerated layer. The air above has sped up since the startup, and the speed maxima are above the barrier tops. The acceleration continues as time progresses to $t=8$ (Fig. 6.3b) and $t=12$ hrs (Fig. 6.3c). Similarly the vertical extent and the magnitude of the deceleration near the surface increase. Like the isentropes in Fig. 6.2 the isotachs upstream of the Continental Divide become more horizontal with time in Fig. 6.3. At $t=12$ hrs (Fig. 6.3c) the decelerated layer (the 9 m/s isotach marks its top) is approximately one kilometer deep.

The steeper slope of the Wasatch Range causes a flow reversal already at $t=8$ hrs (Fig. 6.3b). During the following four hours this reversal increases both in magnitude and vertical extent. The upper boundary of the decelerated layer reaches to crest height (Fig. 6.3c).

As the topography slows down the incoming low-level westerly flow, higher pressure builds up on the upstream side of the two mountain ranges thus adding a southerly component to the flow (Fig. 6.4).

The time series of the v -component shows how the flow deflected by the Continental Divide expands upstream and increases its intensity. At $t=4$ hrs (Fig. 6.4a) that along-barrier flow is confined to the upwind slope of the Continental Divide. At $t=12$ hrs (Fig. 6.4c), however, it has reached the Wasatch Mountains and developed a 7 m/s maximum. The upwind edge of the along-barrier flow propagated upstream at a speed of approximately 11 m/s, as a comparison of Figs. 6.4a and 6.4c shows.

6.2.1 Rotating system

How does rotation alter the response of the flow to the presence of the topography? In this section the wind and potential temperature field of both the rotational and non-rotational case will be compared during the initial adjustment phase (Fig. 6.5) and then the evolution of the flow will be examined under the influence of rotation more closely (Figs 6.6 and 6.7).

The adjustment phase of the initially uniform flow to the topography lasts $O(1/f)$. During this period the Coriolis force slowly starts to modify the flow but at $t=1$ hr the vertical cross-sections of potential temperature, u , and v at $y = -112.5$ km are qualitatively and quantitatively still the same for the case with (Fig. 6.5 a-c) and without (Fig. 6.5 d-f) rotation. The gravity waves and the speed-up of the cross-barrier component above the barrier have already formed and a weak along-barrier flow at the foot of the Continental Divide (CD) and the Wasatch Range (WM) is present.

Three hours later (Fig. 6.6a) the troughs in the isentropes in the lee of the obstacles have deepened and at $t=12$ hrs (Fig. 6.6b) the slope of the isentropes in the lee of the Continental Divide at $z = 3$ km is nearly vertical: the wave is about to overturn. At that time a gravity wave is also visible above the Wasatch. The disturbance traveling upstream from the Continental Divide must have been halted by the Coriolis force since in the non-rotating case (Fig. 6.2c) that disturbance had changed the flow above the

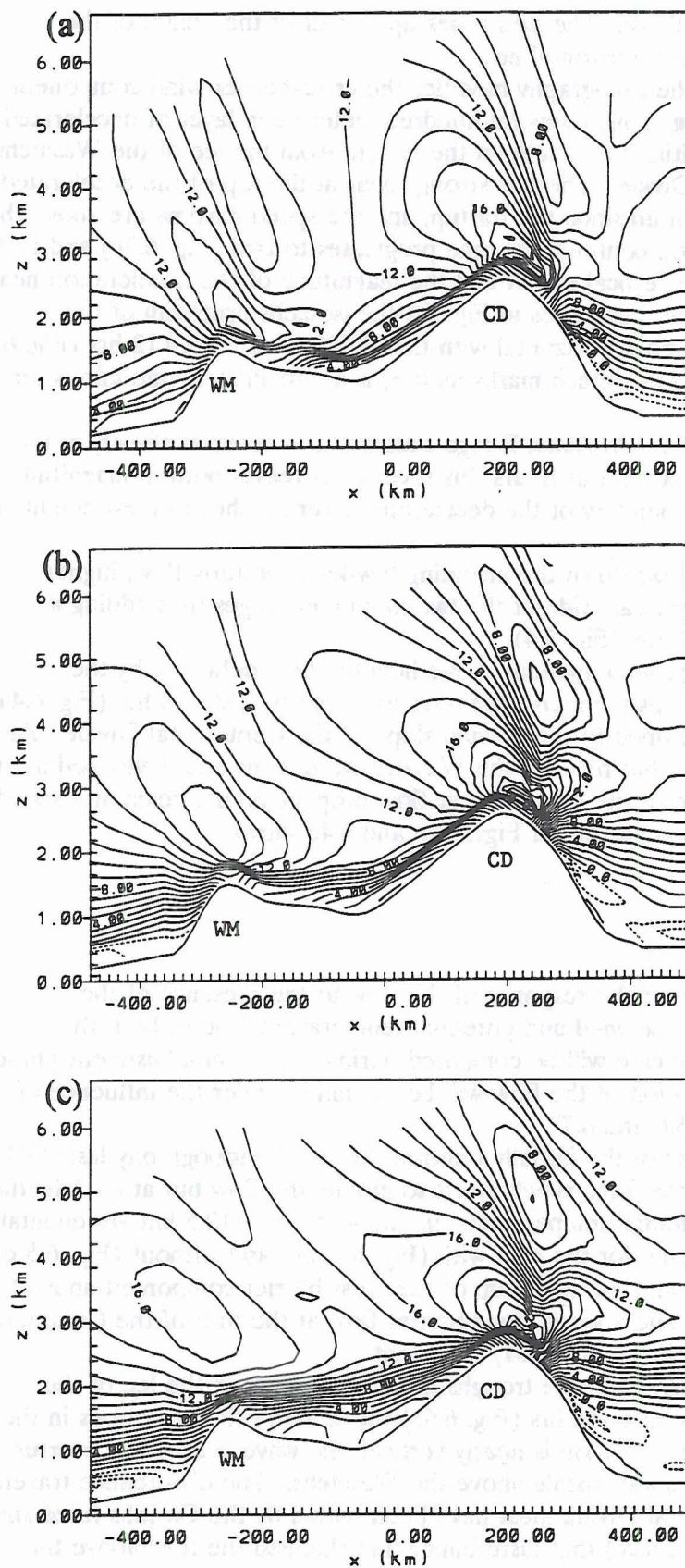


Fig. 6.3: Time series of cross sections of u at $y = -112.5$ km (a) four, (b) eight, and (c) 12 hours after startup. Initialized with uniform flow of $u = 9$ m/s and $N = 0.015$ s⁻¹ (Froude number of 0.3, blocked) without Coriolis force. Contour interval is 1 m/s. Negative contours are dashed.

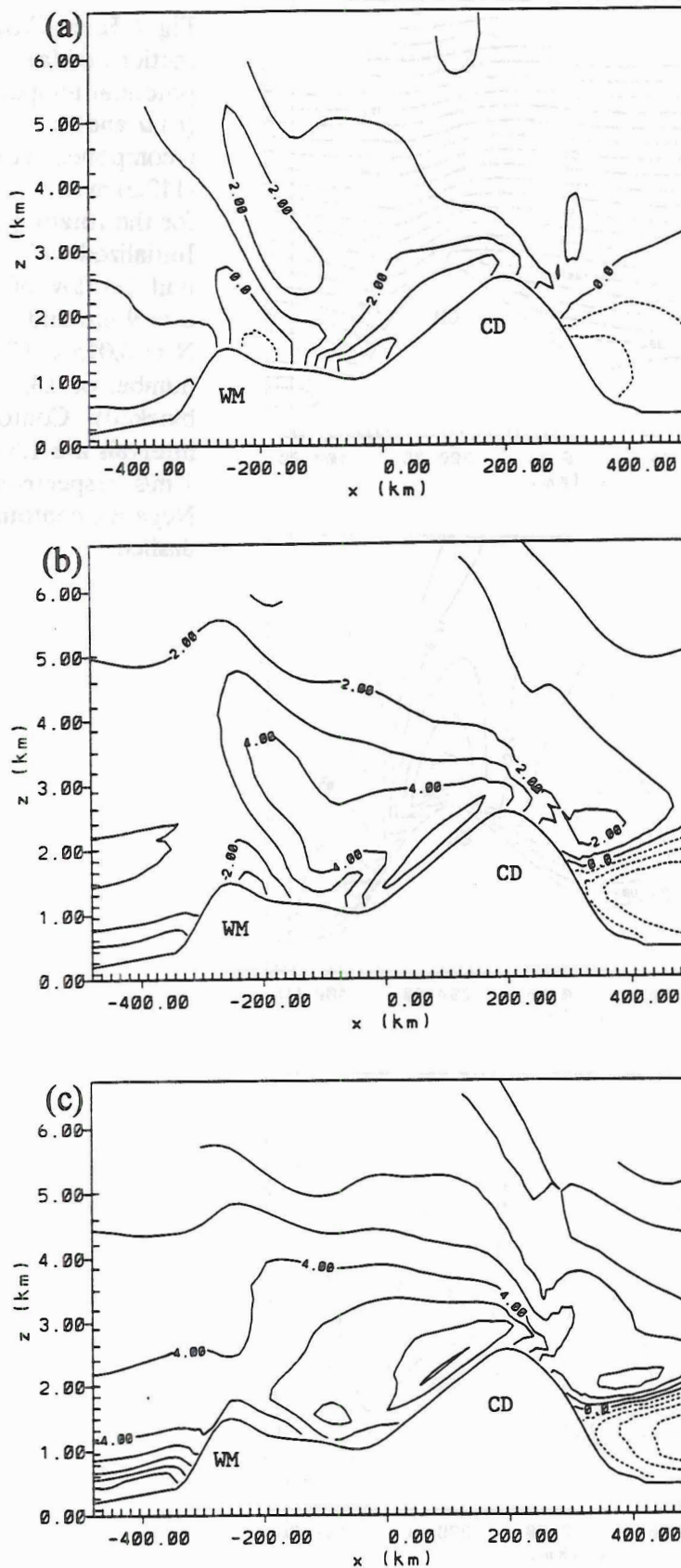


Fig. 6.4: Time series of cross sections of v at $y = -112.5$ km (a) four, (b) eight, and (c) 12 hours after startup. Initialized with uniform flow of $u = 9$ m/s and $N = 0.015$ s $^{-1}$ (Froude number of 0.3, blocked) without Coriolis force. Contour interval is 1 m/s; negative contours are dashed.

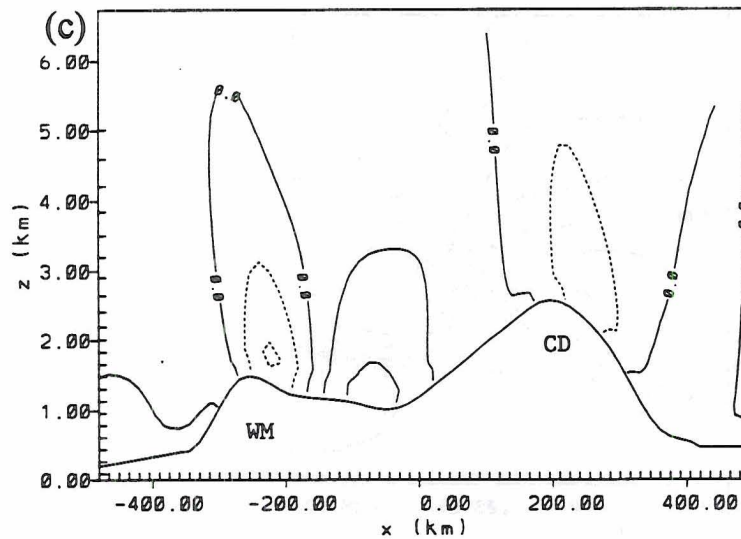
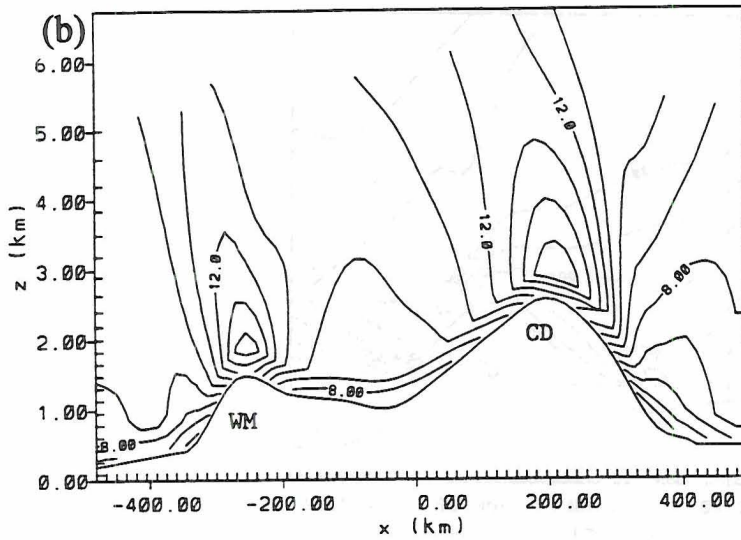
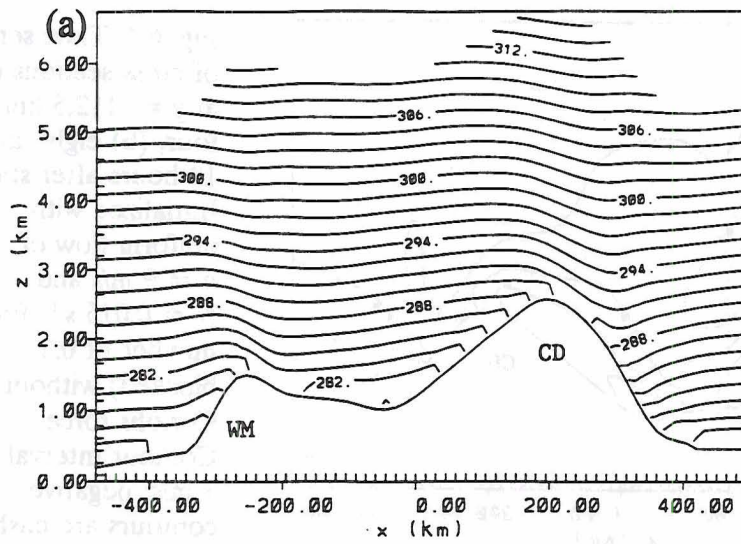


Fig. 6.5a-c: Cross sections of (a) potential temperature, (b) u and (c) v -component at $y = -112.5$ km at $t = 1$ hr for the rotating case. Initialized with uniform flow of $u = 9$ m/s and $N = 0.015$ s $^{-1}$ (Froude number of 0.3, blocked). Contour intervals are 1.5 K and 1 m/s, respectively. Negative contours are dashed.

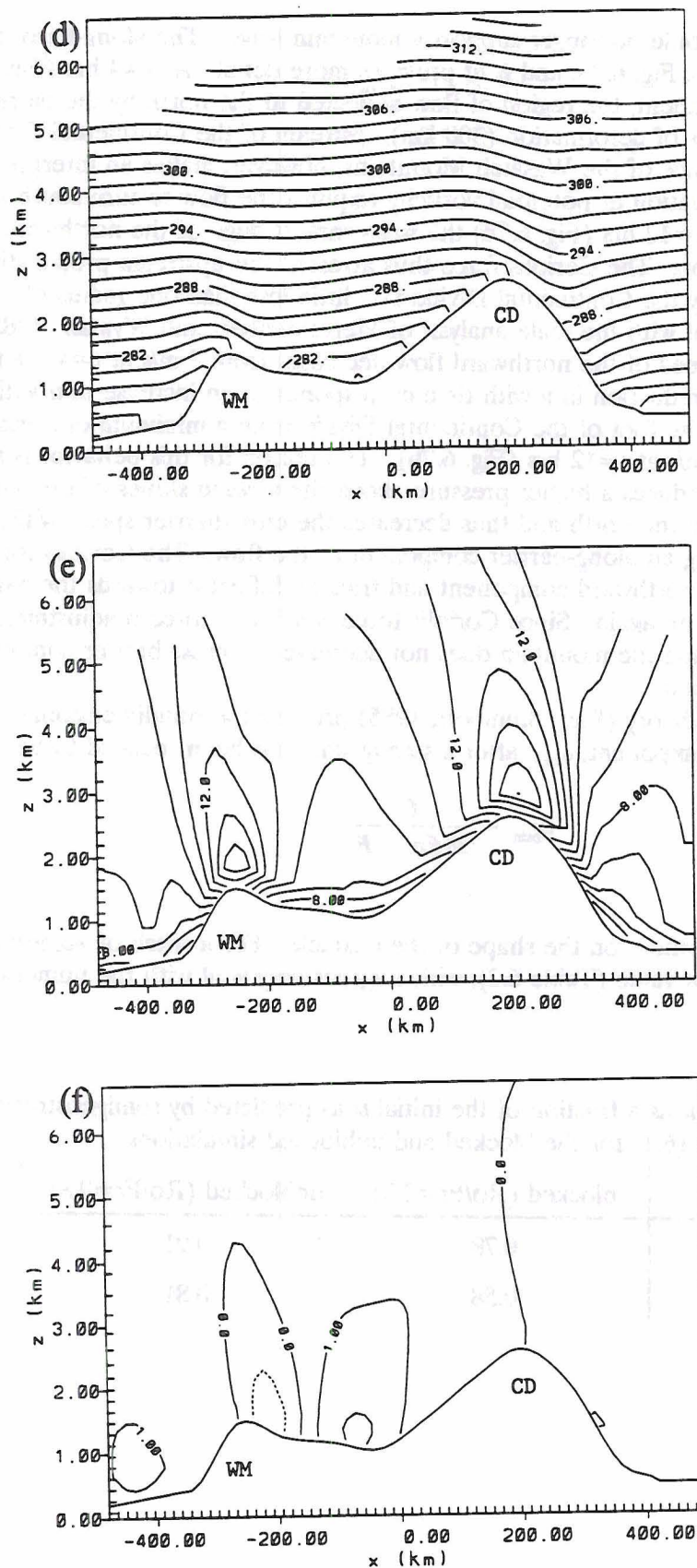


Fig. 6.5d-f: Cross sections of (d) potential temperature, (e) u and (f) v -component at $y = -112.5$ km at $t = 1$ hr for the non-rotating case. Initialized with uniform flow of $u = 9$ m/s and $N = 0.015$ s $^{-1}$ (Froude number of 0.3, blocked). Contour intervals are 1.5 K and 1 m/s, respectively; negative contours are dashed.

Wasatch in a way that could no longer support a mountain wave. The along-barrier wind component at $t=12$ hrs in Fig. 6.7 c and 6.7d provides more detail. At $t=4$ hrs (Fig. 6.7c), i.e. after the initial adjustment, the region of flow deflected to the north by the barrier extends almost one radius of deformation (300 km) upstream of the Continental Divide to $x = -150$ km. The presence of the Wasatch Mountains, however, makes an interpretation difficult since the conservation of potential vorticity requires the flow to turn southward in the lee of a barrier. At $t=12$ hrs (Fig. 6.7d) the westernmost edge of the northward flow is still at the same location. The Coriolis force thus arrested the upstream propagation of the disturbance caused by the Continental Divide at a little less than one radius of deformation in agreement with the scale analysis of Pierrehumbert and Wyman (1985).

The maximum speed of the northward flow decreases from 7 m/s at $t=4$ hrs to 5 m/s at $t=12$ hrs. This reduction in v with time corresponds to an increase in u within the decelerated layer at the foot of the Continental Divide from a minimum of 5 m/s at $t=4$ hrs (Fig. 6.7a) to 7 m/s at $t=12$ hrs (Fig. 6.7b). The reason for this behavior is as follows: The mountain induces a higher pressure above the upwind slopes of the barrier, which deflects the flow to the north and thus decreases the cross-barrier speed while at the same time introducing an along-barrier component of the flow. The Coriolis force starts to act also on that northward component and tries to deflect it towards the barrier: the u -component speeds up again. Since Coriolis force is a "slow" force readjustment of u takes $O(1/f)$. With rotation the mountain does not decrease the cross-barrier component as much as without rotation.

Semigeostrophic theory (Pierrehumbert, 1985) predicts the nondimensional minimum cross-barrier component, u_{min} , after a steady state has been reached to be

$$u_{min} = \frac{F}{MRo + F} \quad (6.1)$$

where M is a factor dependent on the shape of the obstacle. For a witch of Agnesi it is 78% of its initial, uniform value (Table 6.2), which agrees very well with the numerical simulations.

Table. 6.2: Minimum u as a fraction of the initial u as predicted by semigeostrophic theory computed from (6.1) for the blocked and unblocked simulations.

mountain shape	blocked (Ro/Fr=2.3)	unblocked (Ro/Fr=0.8)
witch of Agnesi	0.78	0.91
Gaussian	0.58	0.81

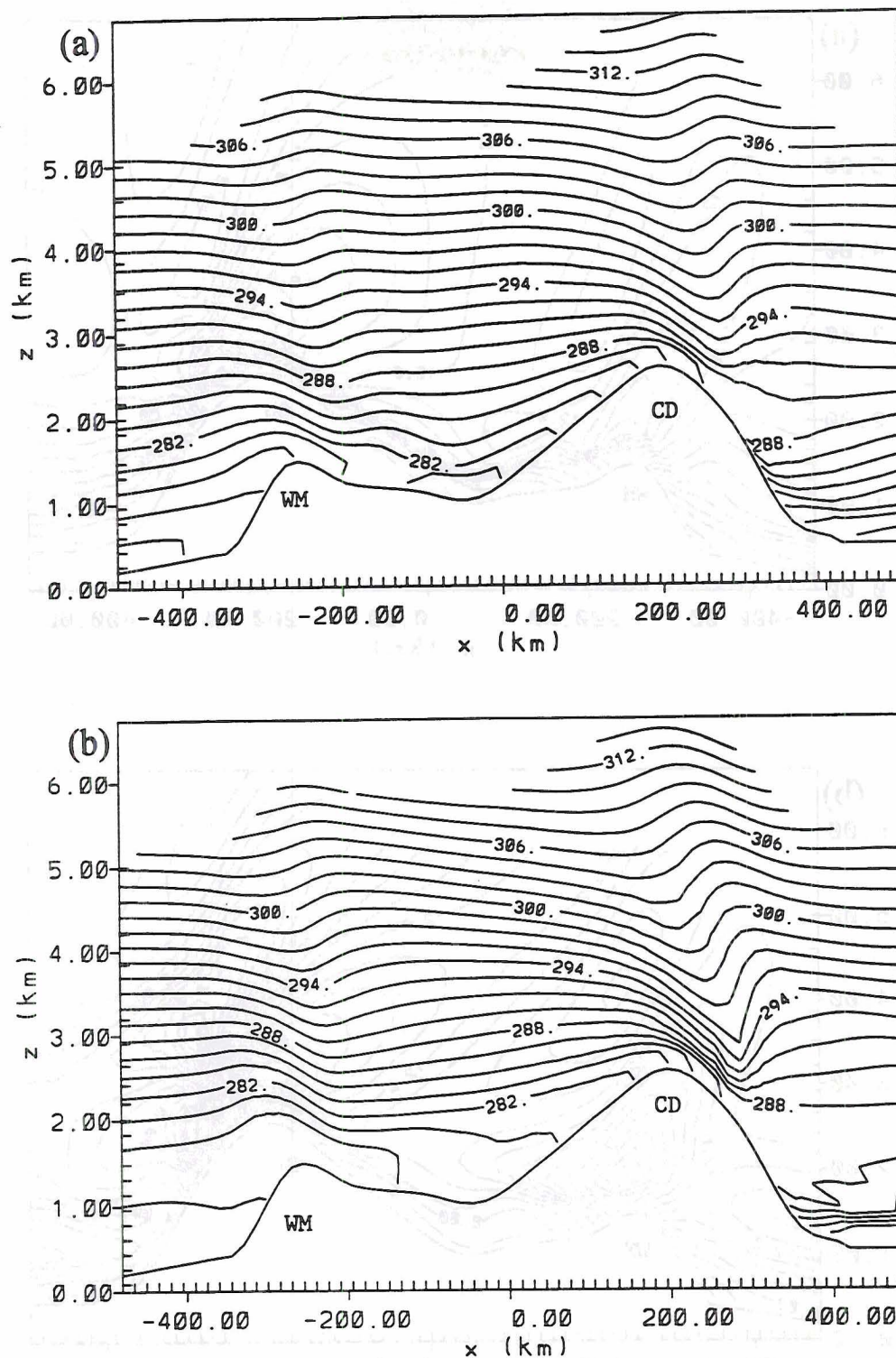


Fig. 6.6: Time series of cross sections at $y = -112.5$ km of potential temperature for the rotating case (a) four, and (b) 12 hours after startup. Initialized with uniform flow of $u = 9$ m/s and $N = 0.015$ s $^{-1}$ (Froude number of 0.3, blocked) with Coriolis force. Contour interval is 1.5 K.

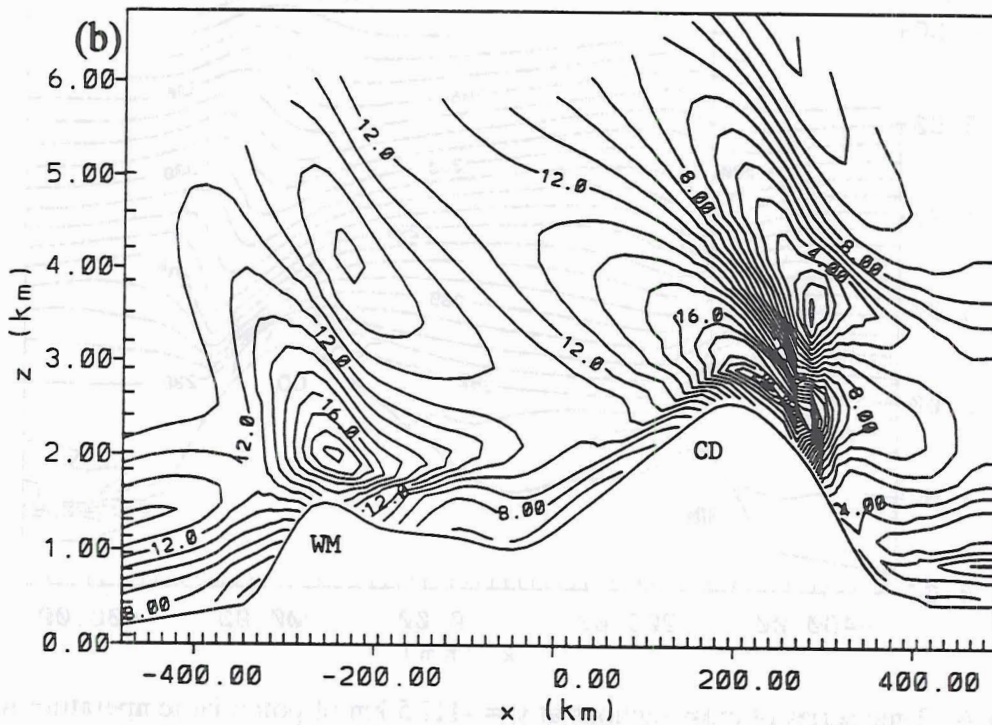
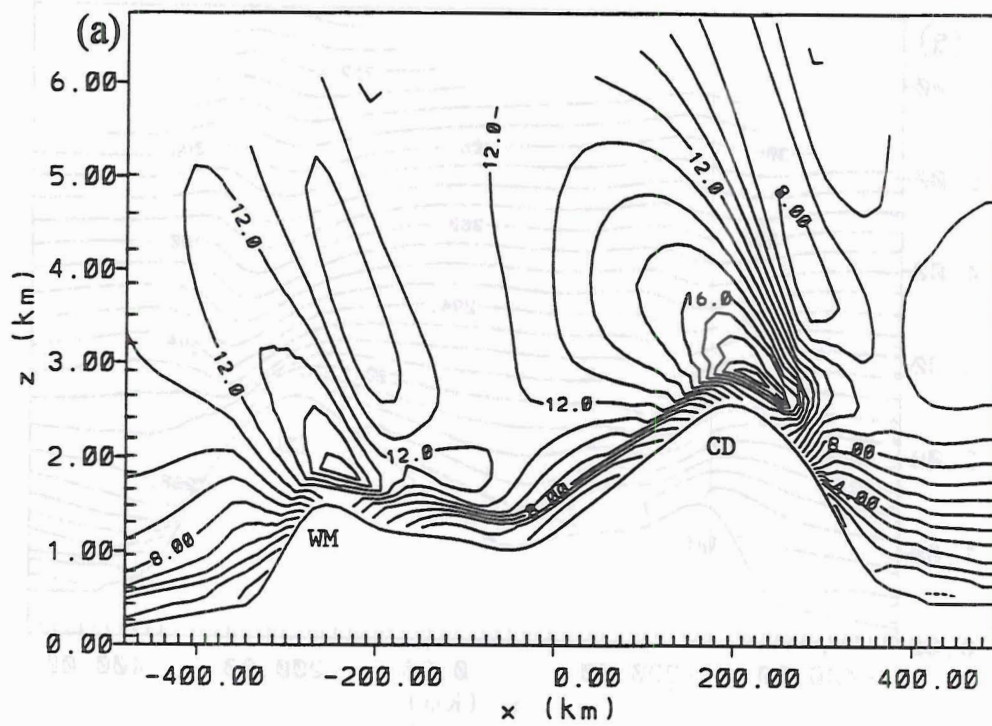


Fig. 6.7a,b: Time series of cross sections of u at $y = -112.5$ km (a) four and (b) 12 hours after model start. Initialized with uniform flow of $u = 9$ m/s and $N = 0.015$ s $^{-1}$ (Froude number of 0.3, blocked) with Coriolis force. Contour interval is 1 m/s.

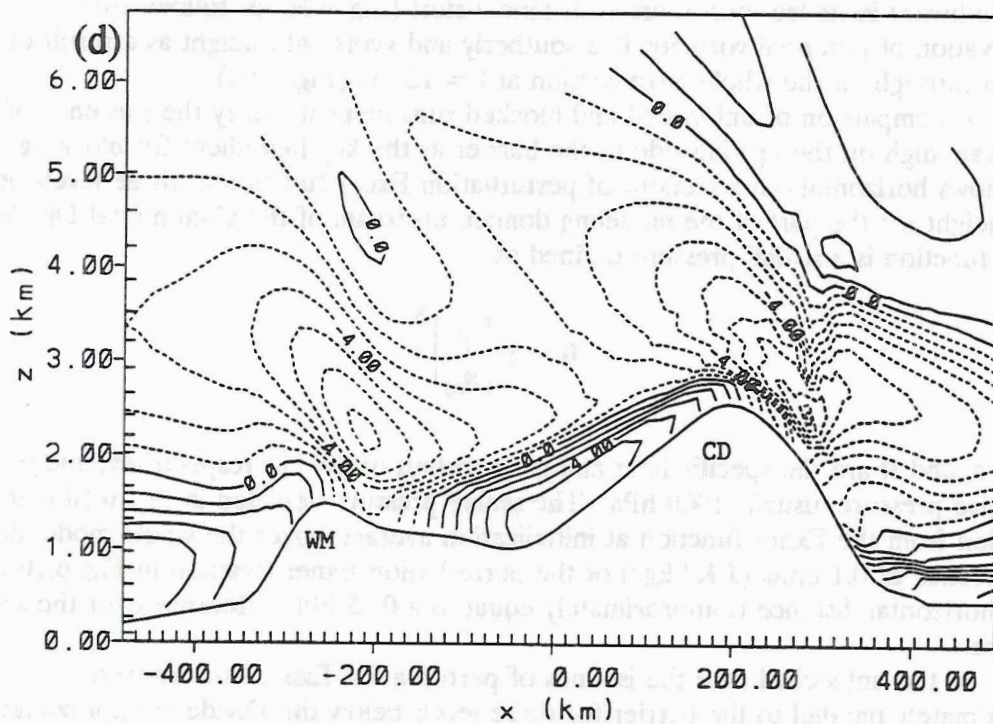
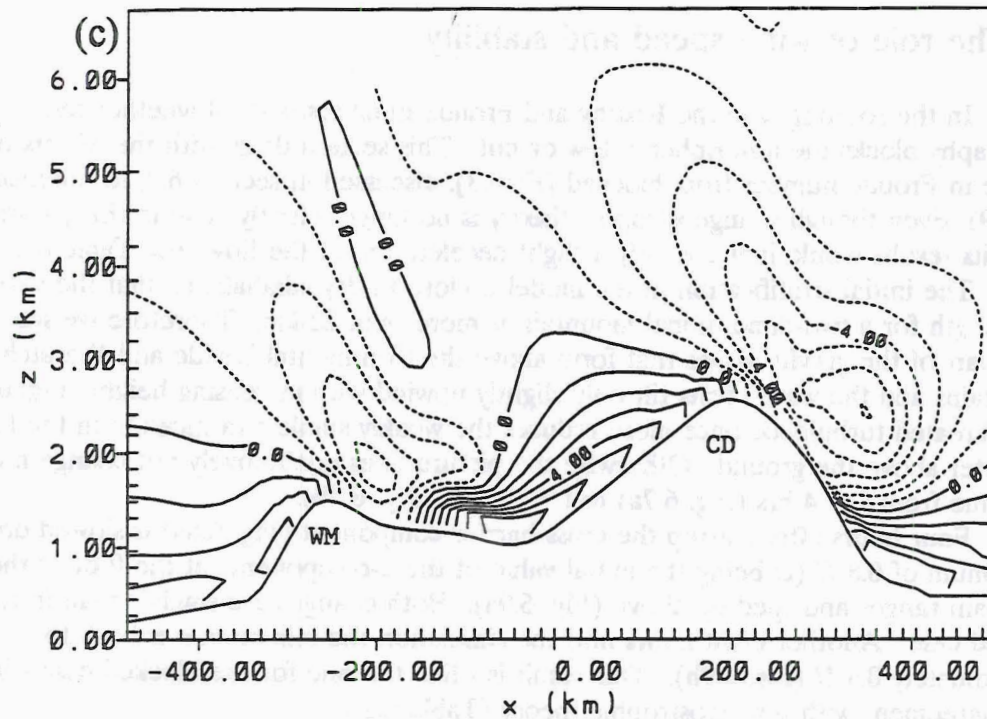


Fig. 6.7c,d: Time series of cross sections of v at $y = -112.5$ km (c) four and (d) 12 hours after model start. Initialized with uniform flow of $u = 9$ m/s, $N = 0.015$ s $^{-1}$, Froude number of 0.3 (blocked); with Coriolis force. Contour interval is 1 m/s; negative contours are dashed.

6.3 The role of wind speed and stability

In the rotating case the Rossby and Froude numbers control whether the topography blocks the atmospheric flow or not. This section deals with the effects of a change in Froude number from blocked ($F=0.3$), discussed in section 6.2, to unblocked ($F=1.9$). Even though semigeostrophic theory is no longer strictly valid in this parameter range its results would indicate only a slight deceleration of the flow (see Table 6.2).

The initial stratification in the model is close to dry adiabatic so that the vertical wavelength for a two-dimensional mountain is more than 22 km. Therefore we see only a small part of the gravity waves that form above the Continental Divide and Wasatch Mountains and the wave crests tilt only slightly upwind with increasing height (Fig. 6.8). Shear-created turbulence once more reduces the weakly stable stratification in the lowest kilometer above the ground. Otherwise the picture does qualitatively not change much with time from $t = 4$ hrs (Fig. 6.7a) to $t = 12$ hrs (Fig. 6.7b).

Four hours after startup the cross-barrier component (Fig. 6.8a) is slowed down to a minimum of $0.8 U$ (U being the initial value of the u -component) at the foot of the mountain ranges and sped up above (Fig. 6.9a). Both changes are smaller than in the blocked case. Another eight hours into the simulation the minimum u is back to approximately $0.9 U$ (Fig. 6.9b). This result is - like the one for the blocked case - in close agreement with semigeostrophic theory (Table 6.2).

While the flow in the lower layers turns northward as it approaches the mountain and southward in its lee four hours after model start (Fig. 6.9c) as follows from conservation of potential vorticity, it is southerly and veers with height as a result of friction throughout the whole cross section at $t = 12$ hrs (Fig. 6.9d).

A comparison of unblocked and blocked runs helps to verify the presence of a mesoscale high on the upwind side of the barrier as the key ingredient for blocking. Fig. 6.10 shows horizontal cross-sections of perturbation Exner function at three levels below crest height for the part of the modeling domain upstream of the Continental Divide. The Exner function is a scaled pressure defined as

$$\Pi = c_p \left[\frac{p}{p_{00}} \right]^{R/c_p} \quad (6.2)$$

where c_p and R are the specific heat and gas constant of dry air, respectively, and p_{00} is a reference pressure, usually 1000 hPa. The scaled pressure depicted in Fig. 6.10 is the deviation from the Exner function at initialization averaged over the whole model domain. A difference of 0.1 units ($\text{J K}^{-1} \text{kg}^{-1}$) of the perturbation Exner function in Fig. 6.10 over a given horizontal distance is approximately equal to a 0.35 hPa difference over the same distance.

In the unblocked case the isolines of perturbation Exner function run approximately parallel to the barrier for three levels below the Divide at approximately 2400 m ASL (Fig. 6.10a), 2750 m ASL (Fig. 6.10b), and 3100 m ASL (Fig. 6.10c). No excess pressure built up on the upwind side of the barrier, on the contrary the pressure is a relative minimum there.

In the blocked case (Fig. 6.10d-f) a pressure nose extends along the upwind side of the barrier for approximately two thirds of the radius of deformation. The excess pressure

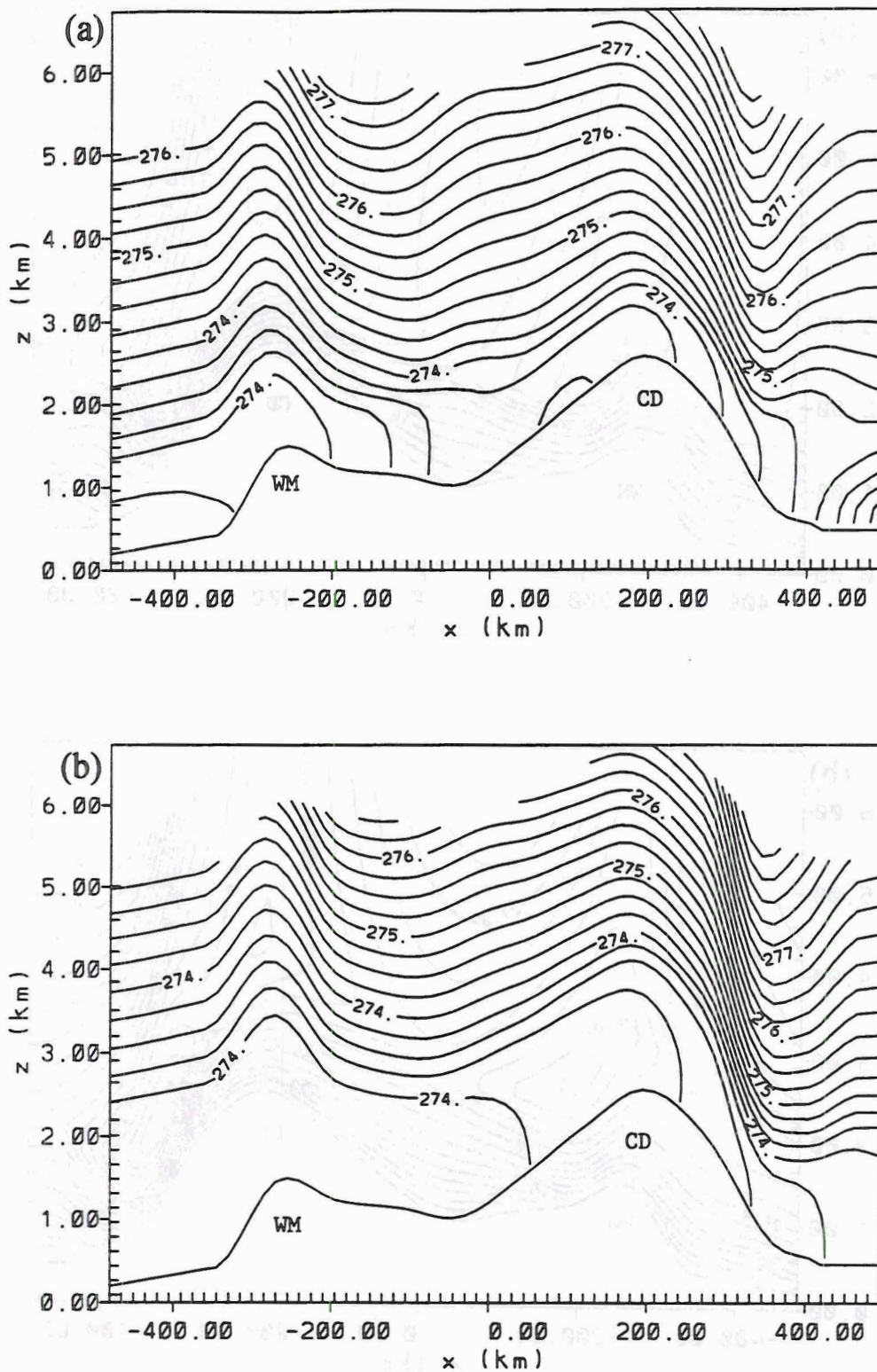


Fig. 6.8: Time series of cross sections of potential temperature at $y = -112.5$ km (a) four and (b) 12 hours after startup. Uniformly initialized with $u = 18$ m/s and $N = 0.005$ s⁻¹ (Froude number of 1.9, unblocked) with Coriolis force.

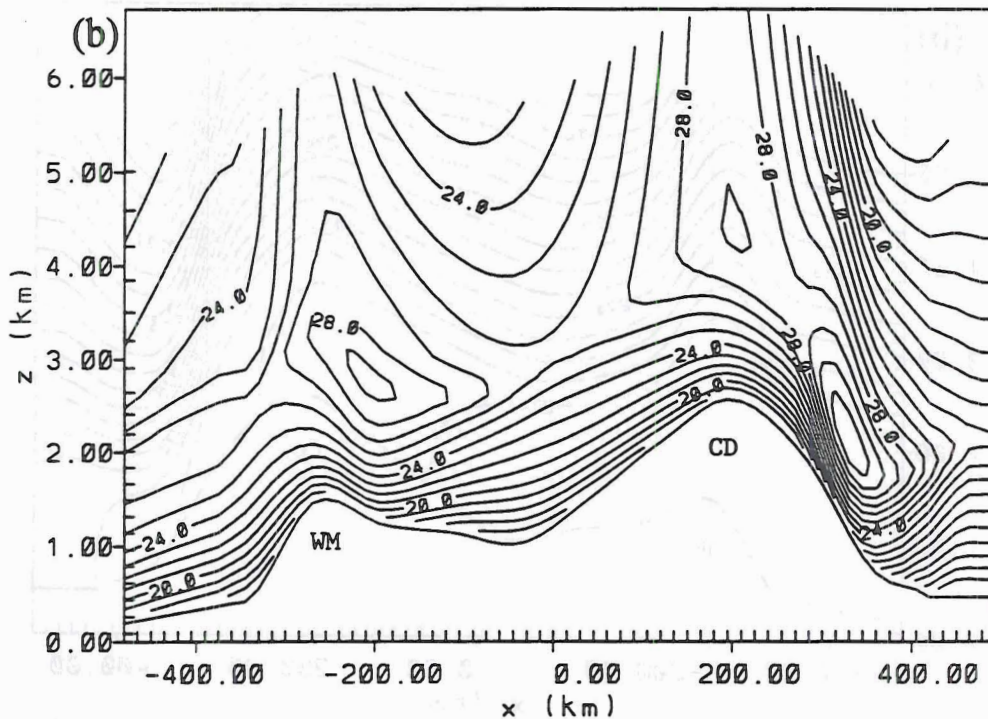
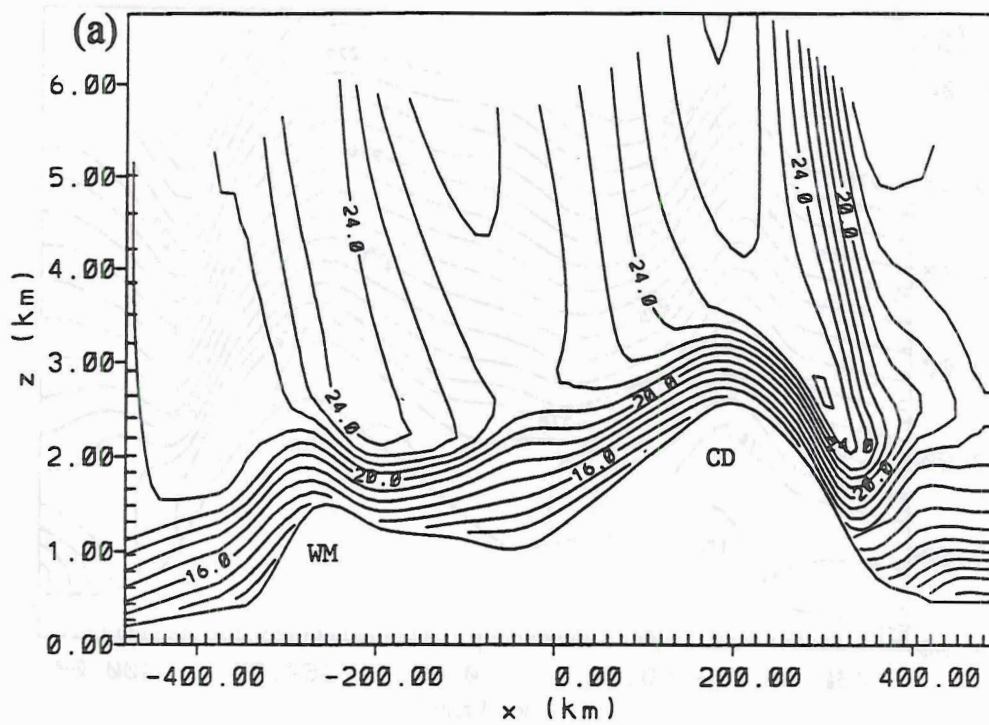


Fig. 6.9a,b: Time series of cross sections of u at $y = -112.5$ km (a) four and (b) 12 hours after startup. Uniformly initialized with $u = 18$ m/s and $N = 0.005$ s $^{-1}$ (Froude number of 1.9, unblocked) with Coriolis force. Contour interval is 1 m/s.

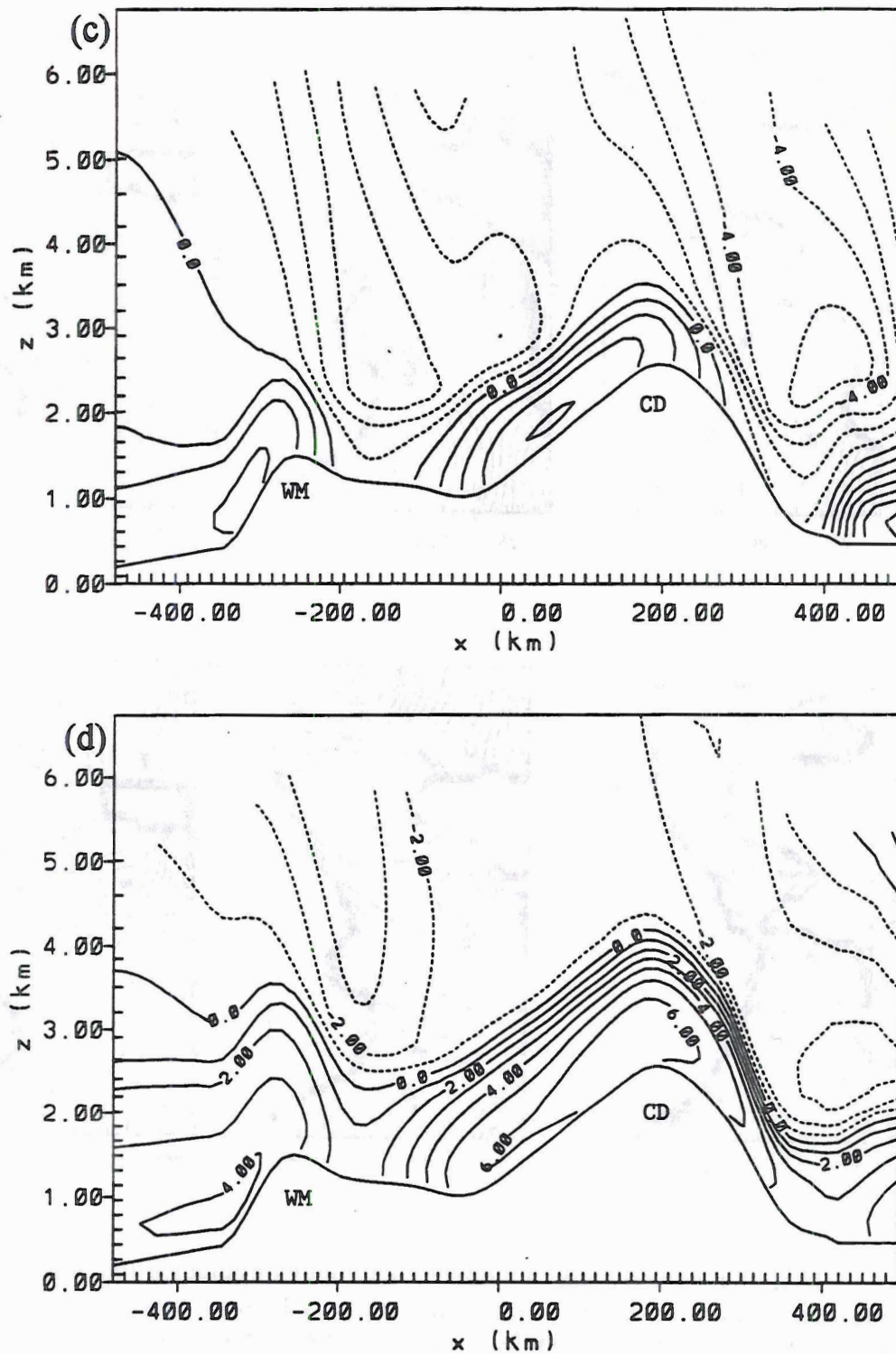


Fig. 6.9c,d: Time series of cross sections of v at $y = -112.5$ km (c) four and (d) 12 hours after startup. Uniformly initialized with $u = 18$ m/s and $N = 0.005$ s $^{-1}$ (Froude number of 1.9, unblocked) with Coriolis force. Contour interval is 1 m/s; negative contours are dashed.

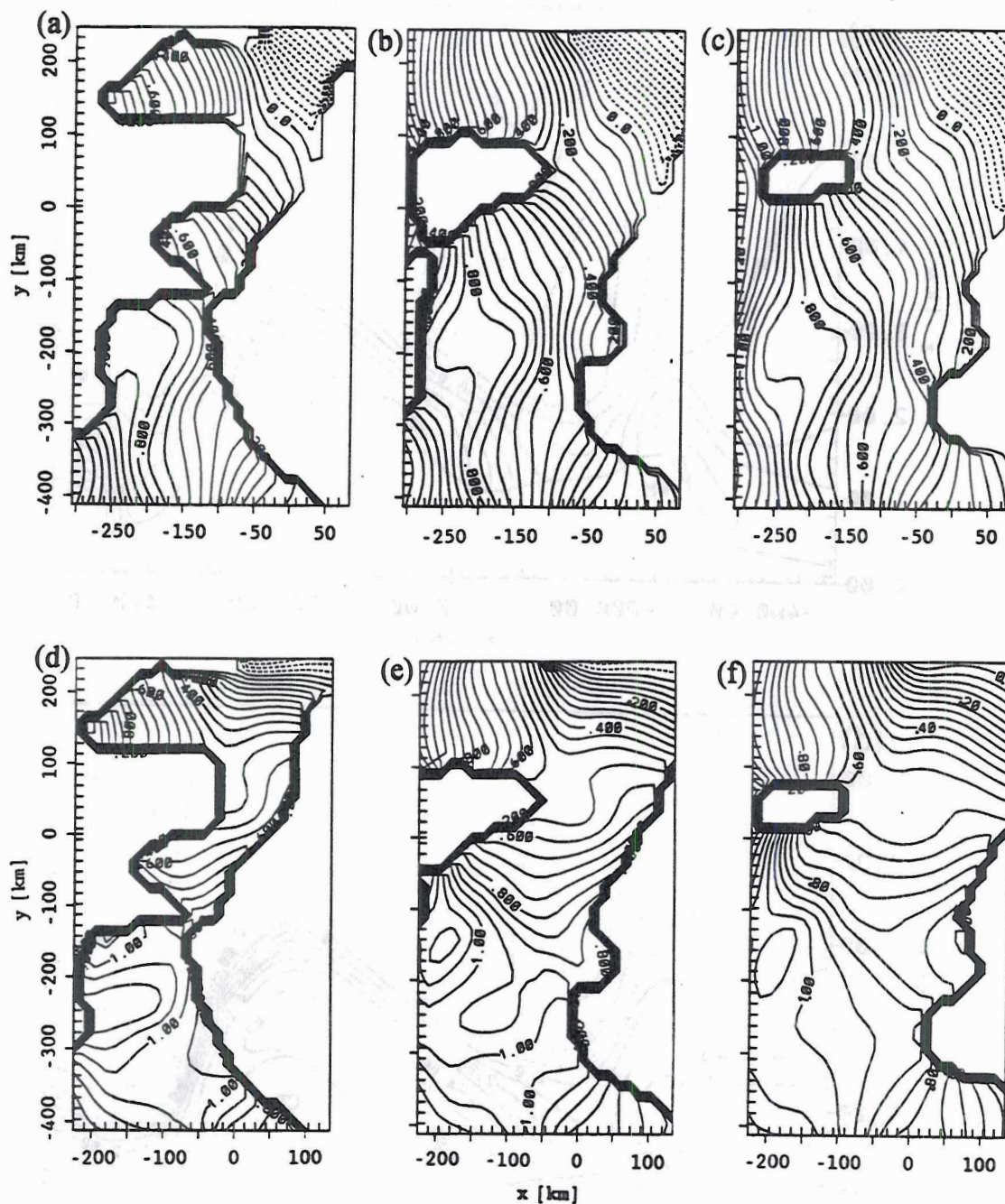


Fig. 6.10: Horizontal cross-sections of perturbation Exner function for the part of the modeling domain upstream of the Continental Divide. Solid lines denote a positive deviation of the Exner function from its initial, domain-averaged value. The three vertical levels are approximately: (a,d) 2400 m ASL, (b,e) 2750 m ASL, and (c,f) 3100 m ASL. The top panel shows an unblocked ($F=1.9$), and the lower panel a blocked ($F=0.3$) case. The parts of the graphs without contour lines are topography extending above the vertical level depicted. The Continental Divide is at the right side of the graph. Contour interval is $0.05 \text{ J K}^{-1} \text{ kg}^{-1}$. Negative contours are dashed.

of the mesoscale high is between 0.2 and 0.3 units of the Exner function, which translates to approximately 1 hPa in terms of unscaled pressure. Although the magnitude of the excess pressure seems very small at first glance, a pressure gradient of one hPa over 200 km (2/3 the radius of deformation) will cause a geostrophic wind of 5 m/s! The pressure distribution, however, deflects the flow towards the north and does not allow the formation of an extended flow reversal zone or stagnant pool.

6.4 The role of initial wind direction

During the observational period the mid-tropospheric winds were mostly from SW to N with blocking occurring at Tabernash and Meeker most frequently with W-NW and at Dugway with SW-W winds. A NW and SW wind were simulated but the cross-barrier component (relative to the Continental Divide) and stability were unchanged to make them comparable with the W-wind cases of the previous sections. These simulations correspond to blocking and include the effects of friction and rotation of the earth.

Table 6.3 summarizes the values of the wind components used.

Table 6.3: Values of the u-component for the NW, W, and SW wind simulations yielding a cross-barrier component (relative to the Continental Divide) of 8.16 m/s.

wind direction	u [m/s]	v [m/s]
NW	6.14	-6.14
W	9	0
SW	16.87	16.87

Horizontal cross sections of wind vectors at various vertical levels at $t=4$ hrs on the region west of the mountain ranges will be presented.

At approximately 2400 m ASL (Fig. 6.11 a-c) the flow splits for NW and W winds but not for SW since that direction is almost parallel to the outlines of the major orographic features. In that case the mountains cannot deflect the wind very much; only the speed increases due to the channeling. Since this holds also for higher levels the plots for SW at these levels are not shown.

The location of the splitting point shifts southward as the wind direction shifts southward: from $y=-180$ km for NW (Fig. 6.11a) to $y=-20$ km for W (Fig. 6.11b) upstream of the Wasatch and from $y=-230$ km to $y=-350$ km upstream of the Continental Divide.

The maximum speed occurs at the Wyoming gap since this is the lowest elevation through which the deflected flow is channeled. Incidentally this area is known as one of the windiest places in the United States (Martner, 1986). Casper, WY, for example has a monthly average wind speed of 7 - 8 m/s during the winter months!

With wind from the northern quadrant the flow at 2400 m ASL is southwesterly at $y=0$ (along which line the three profilers were located) in agreement with the observations.

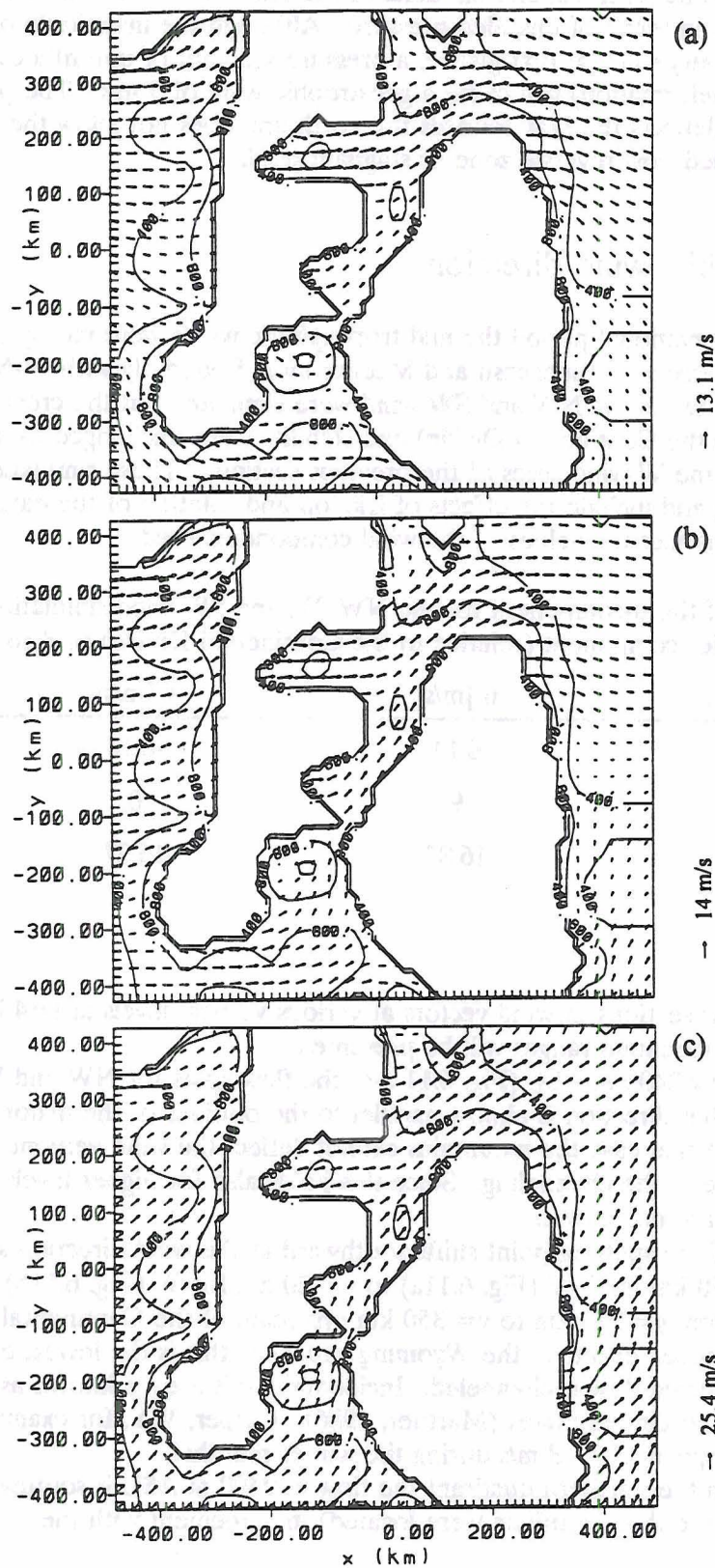


Fig. 6.11:
Wind vectors
at
approximately
2400 m ASL
(962.5m above
the lowest
model
elevation
(1435 m
ASL)) for (a)
NW, (b) W,
and (c) SW
large scale
flow. In all
three cases the
cross-barrier
component is
8.16 m/s and
the buoyancy
frequency
 0.015 s^{-1}
($F=0.3$,
blocked); with
Coriolis force
and friction.

As we move to a higher level in the model to approximately 2750 m ASL the splitting points are farther north (Fig. 6.12). The air finds a gap at $y=-50$ km (Old Woman Plateau) in the Wasatch through which it can flow. This is also the forking point when the large scale wind is from NW: north of it air flows northwards and south of it southwards.

With W winds (Fig. 6.12b), however, the splitting point is much farther south at $y=-260$ km. Upstream of the Continental Divide the flow splits at $y=-180$ km (NW) and $y=-320$ km (W), respectively. At the location of the Dugway profiler the flow is westerly for NW and southwesterly for W. The Continental Divide deflects still effectively enough at that level to make the wind at the Meeker profiler location southwesterly. The maximum wind speed again occurs at the Wyoming gap.

In the model most of the Wasatch Mountains lie below 3100 m ASL. In the northern part, however, the wind direction for large scale NW still is not northwest but rather west because of the channeling through the Wyoming gap (Fig. 6.13a). Only south of $y=-50$ km is the flow from NW. The Continental Divide protrudes above 3100 m and accordingly the flow still splits: at $y=-200$ km for NW and $y=-280$ km for W (Fig. 6.13b).

If we go another 750 m higher to 3850 m ASL (not shown) only two small parts of the orography reach above that level. In the northern half of the modeling domain the flow for large scale northwesterlies still deviates from that direction and is westerly instead. For westerly large scale flow, however, the topographic influence manifests itself mostly in increased speed.

6.5 Summary

According to the numerical simulations blocking forms when denser air piles up above the upwind slopes of the mountains and creates a positive pressure anomaly on the order of one hPa. The disturbance propagates upstream out of the modeling domain without the presence of the Coriolis force. Rotation on the other hand arrests the upstream propagation so that the pressure nose extends over approximately two thirds of the radius of deformation. This mesoscale high decelerates the mountain-normal flow and deflects it northward. If this northward flow is not blocked by another barrier the Coriolis force will also act on the mountain-parallel component and thus speed up the mountain-normal component again.

Without synoptic and radiative forcing the value of Ro/F controls whether the upstream flow is blocked or not. For the simulations performed herein semigeostrophic theory estimates the reduction of the upstream velocity well.

Due to the positive pressure anomaly above the upwind slopes the winds in the lower levels under blocked conditions are always southwesterly whether the large scale wind is SW, W or NW. While for SW the wind does not turn much with height but only speeds up due to channeling, the flow splits for large scale W and NW. The closer to south the large scale wind direction is the farther south in the modeling domain the splitting occurs.

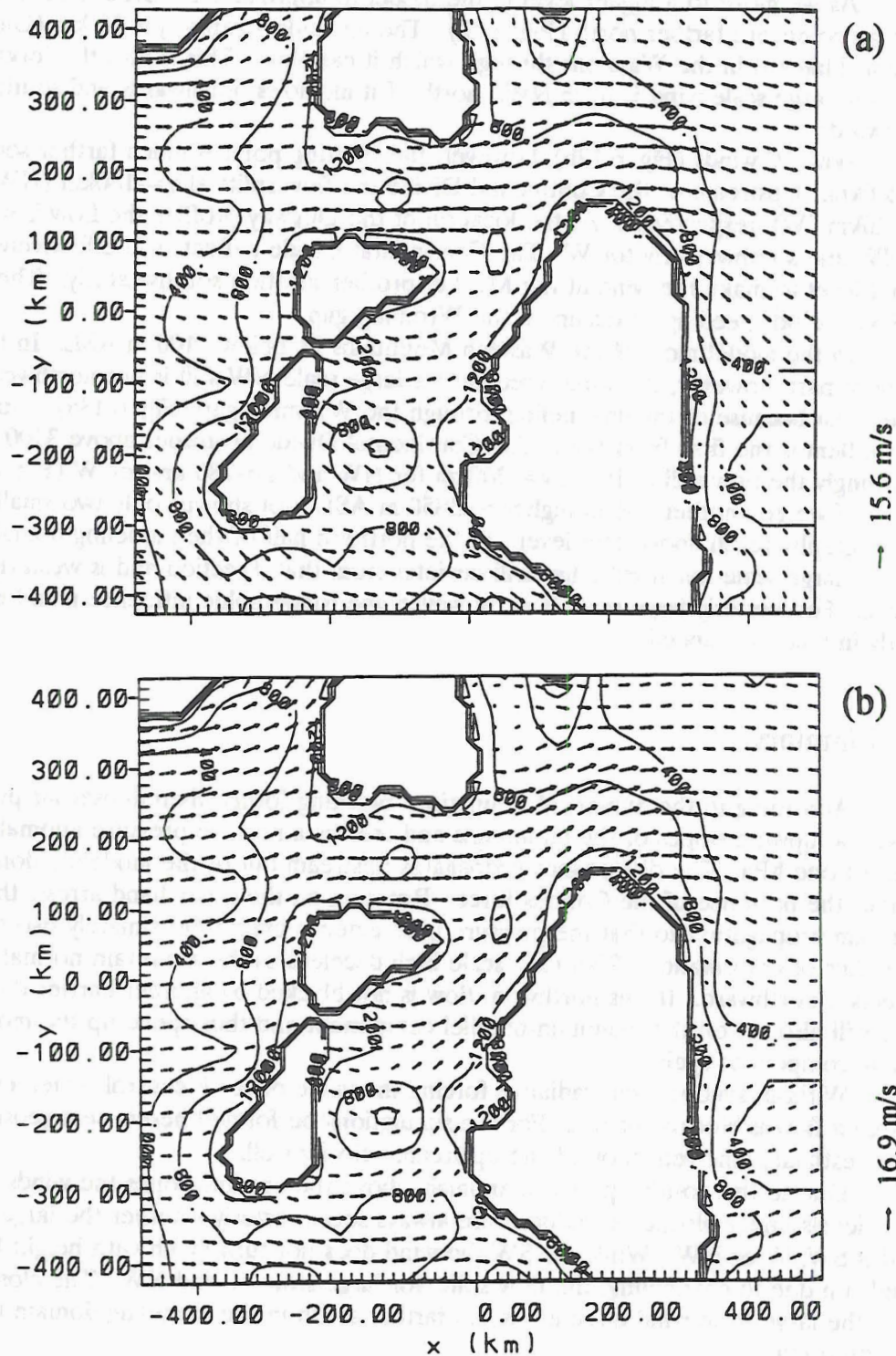


Fig. 6.12: Wind vectors at 2750 m ASL (1312.5 m above the lowest model elevation) for (a) NW and (b) W large scale flow. In both cases the cross-barrier component is 8.16 m/s and the buoyancy frequency 0.015 s^{-1} ($F=0.3$, blocked); with Coriolis force and friction.

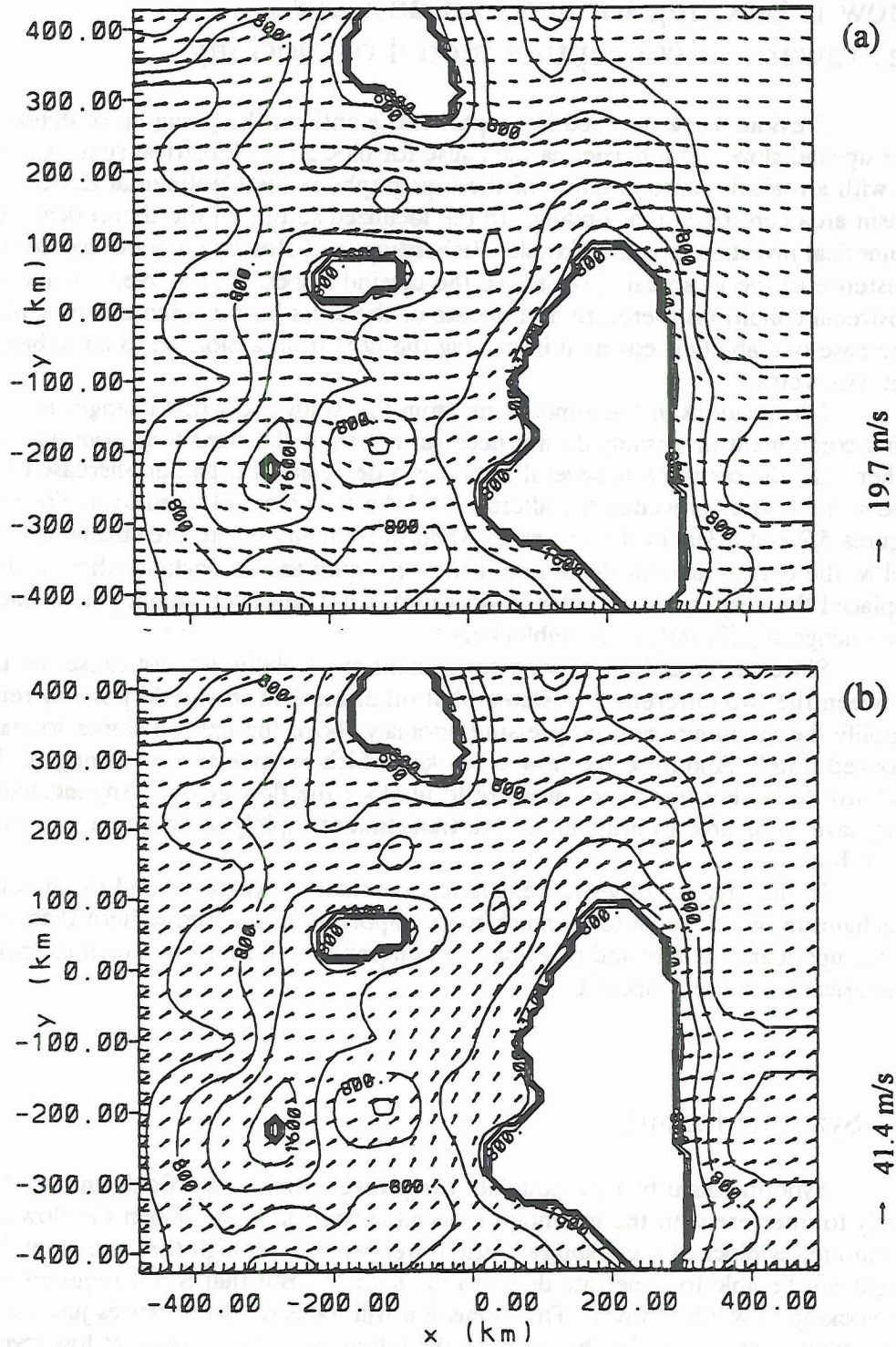


Fig. 6.13: Wind vectors at 3100 m ASL (1662.5 m above the lowest model elevation) for (a) NW and (b) W large scale flow. In both cases the cross-barrier component is 8.16 m/s and the buoyancy frequency 0.015 s^{-1} ($F=0.3$, blocked); with Coriolis force and friction.

How is blocking formed and destroyed or: towards a conceptual model of blocking

Previous work outlined in chapter two identified the piling up of denser air above the upwind slopes of a barrier as the cause for blocking. Numerical simulations (chapter 6) with a realistic representation of the topography in the Continental Divide - Great Basin area confirmed that finding. In the idealized setting of the theoretical and numerical investigations the Froude, Richardson, and Rossby numbers control the existence of the mesoscale high above the upwind slopes. For a given barrier and uniform upstream conditions therefore an increase of the cross-barrier wind component or a decrease of stability is essential in moving the flow from a blocked to an unblocked state and vice versa.

Observations in the atmosphere from this study show that changes in cross-barrier wind component or stability do not necessarily trigger the transition from one state to the other. On the contrary, in several instances a decrease of u and an increase of stability above the barrier preceded the alteration of the flow from blocked to unblocked (compare figures 5.2 and 5.3)! In the few cases when the stability of the previously blocked layer below the barrier actually decreased it was only *after* the unblocking when air from above replaced the very stable air below. Most frequently, however, stability near the surface did not change significantly after unblocking.

Since the cross-barrier wind component and stability did not cause the transition between the two different flow states what other mechanisms could possibly reinforce and amplify the mountain-induced pressure anomaly above the upwind slopes to lead to a blocked state? And once the flow is blocked which mechanisms could negate the excess (relative to farther upstream) pressure to unblock the flow again? Any mechanism would also have to be able to bring about the transition as rapidly as observed, i.e. on the order of an hour.

In this chapter other not commonly considered dynamical and thermodynamical mechanisms, which seem to be much more important in the atmosphere than the change of far upstream stability and cross-barrier component advanced by previous theoretical and numerical work are proposed.

7.1 Synoptic forcing

Synoptic disturbances modulate the pressure and height fields and are therefore likely to interfere with the mountain-induced mesoscale high. When the flow in the Great Basin area is blocked the stability in the lower layers is so high that mid-level disturbances might not be able to penetrate down to the surface. But that is not required for unblocking as will be shown. The discussion will focus on disturbances just above mountaintop at a level that blocking hardly influences. Thus unlike at low levels where the flow has a significant ageostrophic component, a quasigeostrophic framework might still be sufficient to explain at least qualitatively the changes in the height field at that higher level. Since pressure is proportional to the weight of a column of air above a point, lowering the pressure above the blocked layer might be able to unblock the flow, especially since the excess pressure in the mesoscale high is only on the order of one hPa.

The most obvious synoptic feature above mountaintop capable of negating and reversing the mesoscale high below is a trough, a minimum in the mid-level height field. In order to be effective, however, the trough must not be very wide so as to impose a horizontally varying pressure field, which is necessary because of the limited horizontal extent (approximately one radius of deformation) of the mesoscale high. In other words, the synoptic cross-barrier pressure gradient must be directed opposite to the mesoscale pressure gradient and its magnitude greater than the approximately one hPa per 200 km generated by the mountain-induced mesoscale high. Short waves and very intense narrow troughs fulfill these constraints but wide troughs do not since their pressure distribution does not vary enough over one radius of deformation.

Any synoptic pressure gradient in the same direction as the mesoscale one will only augment the mountain-induced mesoscale high so that even when stability and cross-barrier speed of the impinging flow would put the flow into the unblocked parameter space (as determined from undisturbed conditions) a blocked flow can exist.

The quasigeostrophic ω equation evaluated above the blocked layer and the vorticity equation evaluated at the surface or within the blocked layer provide qualitative insight into the mechanisms changing the pressure within the blocked layer. To simplify the discussion the effects of sloped terrain will be included later. If air rises above a level surface, i.e. $\omega < 0$, it follows from the continuity equation that

$$\frac{\partial \omega}{\partial p} = -\delta > 0 \quad (7.1)$$

at the surface (δ is the divergence of the wind on a pressure surface). It follows from the quasigeostrophic vorticity equation that the effect of this convergence at the surface is to make vorticity more cyclonic locally, since

$$\frac{\partial \zeta_g}{\partial t} = -\delta f_0 > 0 \quad (7.2)$$

where ζ_g is the relative geostrophic vorticity, f_0 earth's vorticity and t time. The effects of vorticity advection and friction in (7.2) have been neglected since only convergence is considered. Because

$$\zeta_g = \frac{1}{f_0} \nabla_p^2 \phi \quad (7.3)$$

it follows from (7.2) that

$$\frac{\partial}{\partial t} \nabla_p^2 \phi = \nabla_p^2 \left(\frac{\partial \phi}{\partial t} \right) > 0 \quad (7.4)$$

Therefore the height falls locally, because $\nabla_p^2(\partial\phi/\partial t)$ and $\partial\phi/\partial t$ tend to have opposite signs.

Combining the quasigeostrophic vorticity equation

$$\frac{\partial \zeta_g}{\partial t} = -\mathbf{v}_g \cdot \nabla_p (\zeta_g + f) - \delta f_0 \quad (7.5)$$

with the continuity equation (7.1) and (7.3) yields

$$\nabla_p^2 \left(\frac{1}{\rho} \frac{\partial p_s}{\partial t} \right) = f_0 [-\mathbf{v}_g \cdot \nabla_p (\zeta_g + f)]_{p_0} + f_0^2 \left(\frac{\partial \omega}{\partial p} \right)_{p_0} \quad (7.6)$$

Therefore changes in surface pressure, p_s , are due to vorticity advection (first term on the right side of (7.6)) and divergence (or convergence) associated with vertical motions (second term on right side of (7.6)). The quasigeostrophic ω equation

$$\begin{aligned} \left(\nabla_p^2 + \frac{f_0^2}{\sigma} \frac{\partial^2}{\partial p^2} \right) \omega = & - \frac{f_0}{\sigma} \frac{\partial}{\partial p} [-\mathbf{v}_g \cdot \nabla_p (\zeta_g + f)] - \frac{R}{\sigma p} \nabla_p^2 (-\mathbf{v}_g \cdot \nabla_p T) \\ & - \frac{f_0}{\sigma} \frac{\partial}{\partial p} (-K \zeta_g) - \frac{R}{\sigma p} \nabla_p^2 \left(\frac{1}{c_p} \frac{dQ}{dt} \right) \end{aligned} \quad (7.7)$$

states that a change of vorticity advection with height (first term on right of (7.7)), temperature advection, friction and diabatic heating can force the vertical motions in the second term on the right side of (7.6). A typical wavetrain in the baroclinic westerlies aloft is depicted in Fig. 7.1. There is cyclonic vorticity advection (CVA) downstream of the maximum of absolute vorticity located along the trough axis. Ordinarily vorticity advection aloft is larger in magnitude than at the surface, where pressure systems tend to be more circular. Therefore the vorticity advection is more cyclonic with height, thus air rises and the surface pressure downstream of upper-level troughs falls. Similarly, downstream from a ridge aloft vorticity advection becomes more anticyclonic with height causing sinking motion and thus a rise in surface pressure. Scaling arguments (Carlson, 1991, section 2.1) show that vorticity advection decreases rapidly with increasing wavelength of the wavetrain. Therefore (differential) vorticity advection associated with short waves will cause the strongest falls and rises of the pressure near the surface and be most efficient to facilitate a transition between blocked and unblocked states.

Warm air advection near the surface induces rising motion and thus a fall in surface pressure, whereas cold air advection has the opposite effect.

The effect of friction is generally to weaken the pressure pattern.

Diabatic heating instigates rising motion and thus a fall in surface pressure which might be strong enough to negate the mountain-induced mesoscale high. The effect of radiative heating and cooling will be discussed in the following section.

In the absence of any other than orographic forcing the quasigeostrophic ω equation at the surface is (Bluestein, 1993)

$$\nabla_p^2 \omega_0 = - \frac{f_0^2}{\sigma} \frac{\partial^2 \omega_0}{\partial p^2} \quad (7.8)$$

where σ , the static stability parameter, is

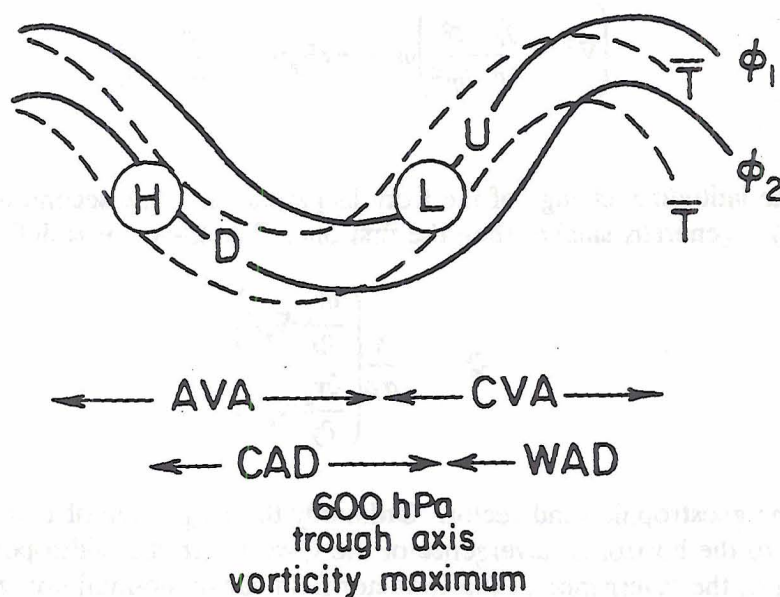


Fig. 7.1: Idealized mid-level disturbance with thickness (dashed) and 600 hPa geopotential height contours (solid). U marks the region of strongest upward and D the region of strongest downward motion. Cyclonic (positive) vorticity advection is denoted by CVA , anticyclonic by AVA , warm air advection by WAD , and cold air advection by CAD . The positions of the surface low and high are marked by a circled L and H , respectively.

$$\sigma = -\frac{RT}{p} \frac{\partial \ln \theta}{\partial p} \quad (7.9)$$

Air near the surface is forced upwards along the upwind slope, i.e. $\omega_0 < 0$, and consequently the left side of (7.8) is positive. Substituting (7.1) into the right side of (7.8) yields the result that

$$-\frac{\partial \delta}{\partial p} > 0 \quad (7.10)$$

that is, divergence increases with height. Hence, if at some level above mountaintop the isentropes are horizontal so that ω and δ are zero there must be divergence ($\delta > 0$) at the surface. This divergence makes the surface vorticity more anticyclonic and increases surface pressure. Thus the quasigeostrophic vorticity and ω equation also contain the mountain-induced mesoscale high!

Although the ω equation in the previously discussed form fosters the understanding of the physical processes involved, it is difficult to use because sometimes the individual

forcing terms partially cancel. Writing the quasigeostrophic ω equation in **Q-vector form** (Hoskins et al., 1978) combines the forcing terms:

$$\left(\nabla_p^2 + \frac{f_0^2}{\sigma} \frac{\partial^2}{\partial p^2} \right) \omega = -2 \nabla_p \cdot \mathbf{Q} - \frac{R}{\sigma p} \beta \frac{\partial T}{\partial x} \quad (7.11)$$

where β is the latitudinal change of the Coriolis parameter. The second term on the right side of (7.11) is generally smaller than the first one. The Q-vector is defined as

$$\mathbf{Q} = -\frac{R}{\sigma p} \begin{pmatrix} \frac{\partial v_g}{\partial x} \cdot \nabla_p T \\ \frac{\partial v_g}{\partial y} \cdot \nabla_p T \end{pmatrix} \quad (7.12)$$

where v_g is the geostrophic wind vector. Ordinarily the magnitude of ω in (7.11) is proportional to the horizontal divergence of the Q-vector in the midtroposphere. Computation of the divergence of the Q-vector field above mountaintop allows therefore qualitative inferences about the vertical velocity field and consequently the surface pressure.

In summary two synoptic mechanisms can oppose the mountain-induced pressure gradient: the height minimum of a short wave trough immediately upstream of the barrier and synoptically induced rising motions caused by cyclonic vorticity advection that increases with height, temperature advection or diabatic heating. Similarly the presence of a ridge upstream of the obstacle and sinking motions will reinforce the mesoscale high.

7.2 Radiative forcing

Sufficient surface heating will build a well-mixed boundary layer that can grow deep enough to recouple with the air above that flows over the mountain. No decrease of stability above barrier top needs to precede the unblocking in that case.

Fewer blocked situations will occur as the net radiation balance becomes more positive and the smaller the barrier is. Outside of the low-sun season the boundary layer upstream of the Continental Divide regularly grows deeper than the barrier due to a high net radiation balance, much of which goes into sensible rather than latent heat flux due to the aridity of that area. In winter, however, with snow present most of the time, the net radiation balance during daytime is small and accordingly the boundary layer only grows a few hundred meters deep. Regions close to the Continental Divide (where the barrier height is small) can become unblocked through surface heating even in winter. Another fact also helps: Snow falls off conifer trees soon after a snow storm so that forested areas have a smaller albedo and thus a more positive net radiation balance than the unforested lands at lower elevations in the Great Basin area.

Radiative cooling of the surface during the night will cool the air above through turbulent mixing and long wave radiative flux divergence. Snow is very close to being a black body. When it covers the ground as was the case during most part of the observational period the energy loss due to infrared emission will therefore be maximized and maximize the cooling of the surface air. The higher stability makes it harder for the air to rise and thus more likely to become blocked.

Clouds usually accompany a short wave disturbance. During daytime they decrease the solar insolation and the radiative heating near cloud bottom changes the stratification below to nearly isothermal thus stabilizing the atmosphere and increasing the likelihood of blocking.

7.3 Classification of blocking events during the observational period

To answer the question which of the mechanisms discussed in sections 7.1 and 7.2 actually lead to the formation and destruction of blocking, bi-daily data from the NWS rawinsonde network were analyzed. Wind and height data at 600 hPa and 700 hPa were gridded by applying two passes of a Barnes objective analysis scheme (Achtmeier, 1987) and calculated advection of absolute vorticity and temperature. The 600 hPa level was chosen since it was always above the top of even the highest mountain in the Rockies. Since the average horizontal distance between rawinsonde stations is more than 200 km only disturbances at least 400 km wide can be reliably resolved. Vorticity and temperature advections are on a smaller scale than the pressure disturbance itself and thus pose even bigger problems. The twelve hour interval from one sounding to the next adds to the difficulty in fixing the exact location of warm and cold advection and cyclonic and anticyclonic vorticity advection regions at the transition time between blocked and unblocked states, which was found from the quasi-continuous profiler measurements. To partially alleviate these problems the turning of the wind above mountaintop was assumed to qualitatively resemble the turning of the geostrophic wind. Then warm air gets advected when the wind turns clockwise with height and cold air when it turns counterclockwise.

Figures 7.2 (for unblocking) and 7.3 (for blocking) summarize the results. They show which of the forcing functions (position of the trough axis, vorticity advection, temperature advection, radiation balance) was favorable and which unfavorable for unblocking and blocking respectively.

7.3.1 Unblocking

a) Tabernash and Meeker

Synoptic forcing played a dominant role in unblocking. Fig. 7.2a depicts the 18 events when blocking did not formally end because of the westerly component above mountaintop ceased. Twelve of these unblocking events occurred when the trough axis was just above the Continental Divide. In these situations the synoptic cross-barrier pressure gradient just upstream of the barrier opposed and overpowered the mesoscale, mountain-induced pressure gradient in the blocked layer above the upwind slope.

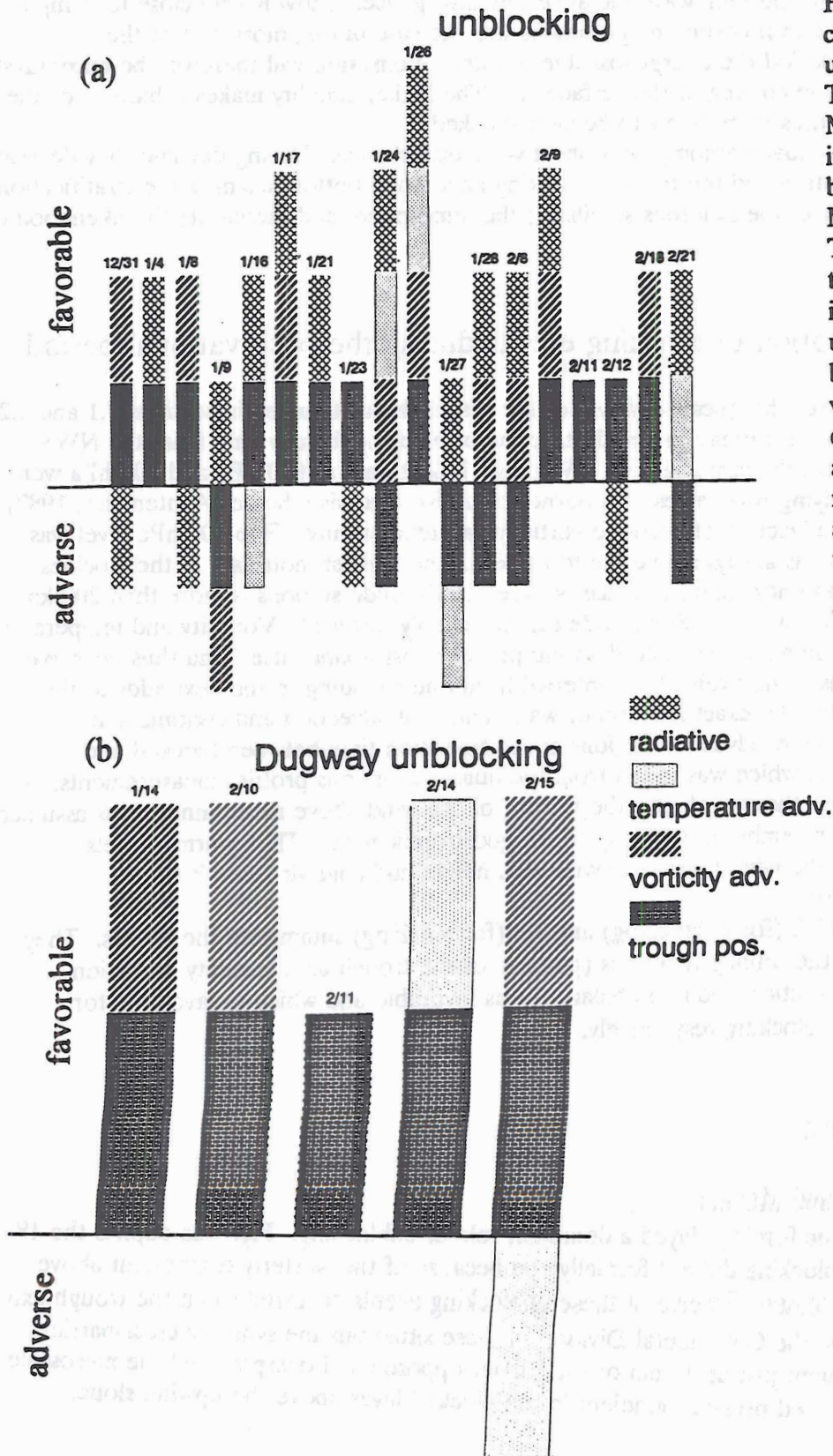


Fig. 7.2: Favorable conditions for unblocking in (a) Tabernash and Meeker, and (b) in Dugway. blocking events in Meeker and Tabernash. A trough axis immediately upstream of the barrier, cyclonic vorticity advection, cold air advection and a positive net radiation budget are favorable for unblocking (compare text). The date above the bars is in months and days relative to LST.

Horizontal pressure contrasts caused by vorticity and temperature advection were only of secondary importance. Nine unblocking events had the favorable pattern of anticyclonic vorticity advection farther upstream (pressure rise, sinking motion aloft) and cyclonic vorticity advection just upstream of the Divide (pressure fall, rising motion aloft). Almost the same number of the events (8) had no significant vorticity advection at all. Only one unblocking, however, happened when the vorticity advection pattern was reinforcing the mesoscale high by causing height rises just upstream of the barrier and height falls farther upstream.

Temperature advection did not significantly contribute to a change in pressure upstream of the barrier: Warm air advection there (favorable for unblocking) occurred only three times and the unfavorable cold air advection twice.

Winds during unblocking blew from W to NW with the exception of December 31, 1991, when it was from SW.

Six unblocking events occurred with the trough axis of the synoptic disturbance already to the east of the barrier so that the synoptic cross-barrier gradient reinforced the mesoscale one. Although four of these cases had favorable vorticity or temperature advection patterns to decrease the geopotential height above the upwind slope, radiative forcing seems to have dominated these cases. All of these unblocking events happened in the afternoon when the positive net radiation balance had been feeding into a sensible heat flux long enough to form a deep boundary layer. In January, when the net radiation balance during daytime was only slightly positive all the radiatively forced unblockings took place in Tabernash. The barrier there is 600 m shallower than in Meeker and additionally the tree coverage is higher, which increases the sensible heat flux into the atmosphere during daytime and decreases the nightly cooling as outlined in section 7.2.

The last unblocking event in February without a low at 600 hPa just upstream of the Divide occurred in Meeker in the afternoon. By that time the solar insolation was already stronger and not all the ground was snow-covered so that the sensible heat flux was obviously strong enough to grow the boundary layer deep enough to reconnect the blocked layer with the flow above and bring so the unblocking about. Since the third SOP coincided with that event data are available to substantiate that statement. Surface radiation, temperature, humidity and wind measurements were used to calculate the sensible and latent heat fluxes applying the Penman-Monteith method (Stull, 1988) assuming wet ground. The sensible heat flux between 09 and 15 LST provided enough energy to form an 1100 m deep (i.e. three fourths of the barrier depth) neutral layer.

Of course synoptic and radiative forcings did not only work separately but in some cases hand in hand. Six unblockings in Tabernash happened with a 600 hPa low just upstream of the Continental Divide and in the afternoon so that a deep enough boundary was present to assist in recoupling the blocked layer to the flow above mountaintop.

b) Dugway

Fig. 7.2b depicts the synoptic conditions for the five transitions of the flow from blocked to unblocked during the observational period. All cases had the 600 hPa low just upstream of the Wasatch Range so that the synoptic cross-barrier pressure gradient opposed and overpowered the mountain-induced mesoscale pressure gradient. Cyclonic vorticity advection over the Wasatchs destabilized the lower atmosphere, caused heights to fall further and air aloft to rise while at the same time anticyclonic vorticity advection farther upstream stabilized the lower atmosphere and caused height rises in three additional cases.

The temperature advection did not play a crucial role in changing the surface pressure. There was one case each of favorable and unfavorable temperature advection. Three cases had no significant temperature advection at all.

Unlike Tabernash and Meeker unblocking took place for the whole possible range of wind directions at 600 hPa: from SW to NNW.

Of all the three profiler sites Dugway faces the highest barrier. None of the unblocking events occurred in the afternoons, which means that a boundary layer could not grow deep enough to cause or assist the unblocking by reconnecting the blocked layer with the flow above mountaintop.

7.3.2 Blocking

a) Tabernash and Meeker

Synoptic forcing was even more dominant than for unblocking: it played a role in all 21 events shown in Fig. 7.3a when a westerly flow above mountaintop occurred. The position of the 600 hPa low (trough) was east (downwind) of the barrier so that the region just upstream of the Continental Divide lay under a ridge, which supported the formation of a mesoscale high there in lower levels.

An unusual situation happened on February 23, 1992, in Meeker. The trough axis of a short wave approached the profiler site from the west thus causing a fall in the height of the 600 hPa pressure surface farther upstream, which made the height just upstream of the barrier relatively high enough to bring about a blocking. Since the short wave swept swiftly across western Colorado that particular blocked situation lasted only the few hours it took the trough to reach the vicinity of the Continental Divide and thus reverse the pressure gradient.

In 12 cases was the vorticity advection more anticyclonic just upstream of the barrier than farther upstream, which lowered the 600 hPa height there relative to the region close to the barrier and instigated rising motion above mountaintop. Seven blocking events occurred without any significant vorticity advection and only two with an advection pattern unfavorable to blocking. As in unblocking, vorticity advection was second to the presence of a 600 hPa height extremum just upstream of the barrier as a synoptic forcing mechanism leading to blocking.

Warm air advection above the upwind slopes assisted blocking in seven instances. Only one case with unfavorable cold air advection occurred. The remaining 13 cases did not have any significant temperature advection at all.

The wind direction at 600 hPa at the time of unblocking was from W to NNW, similar as for blocking. Wind direction was thus no indicator for an impending transition between the two states of the flow.

Radiative forcing never sufficed to trigger blocking by itself. However, in 17 instances the nocturnal cooling and stabilization of the low-level air assisted the synoptic forcing upon the flow to become blocked. As with unblocking the radiative forcing was most effective in Tabernash where the barrier is relatively shallow.

b) Dugway

Dugway encountered only five transitions from an unblocked flow with a westerly component above to a blocked flow (Fig. 7.3b). The trough was downstream of the Wasatch Range in all five instances so that once more the synoptic cross-barrier pressure

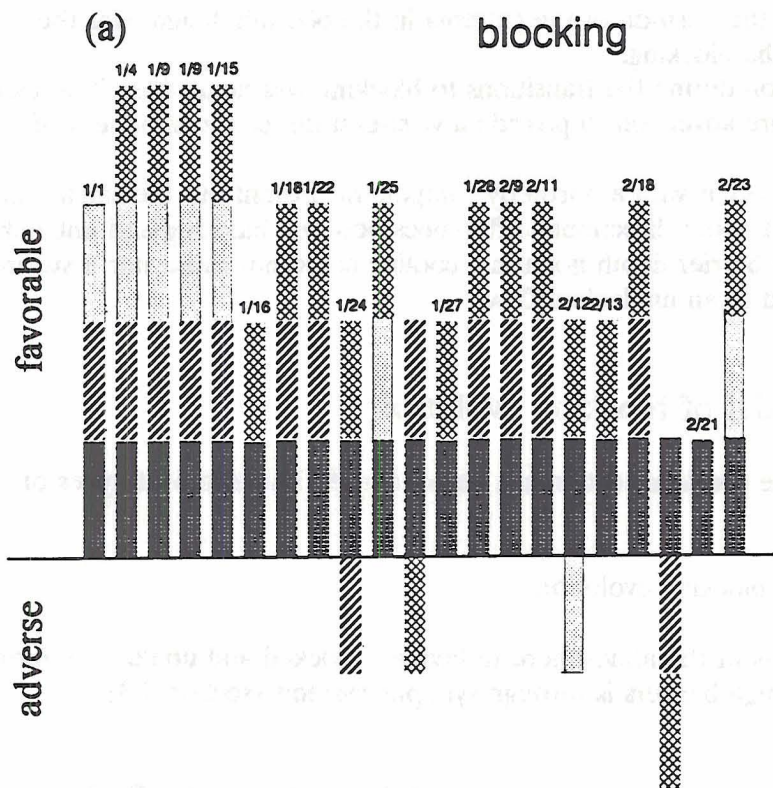
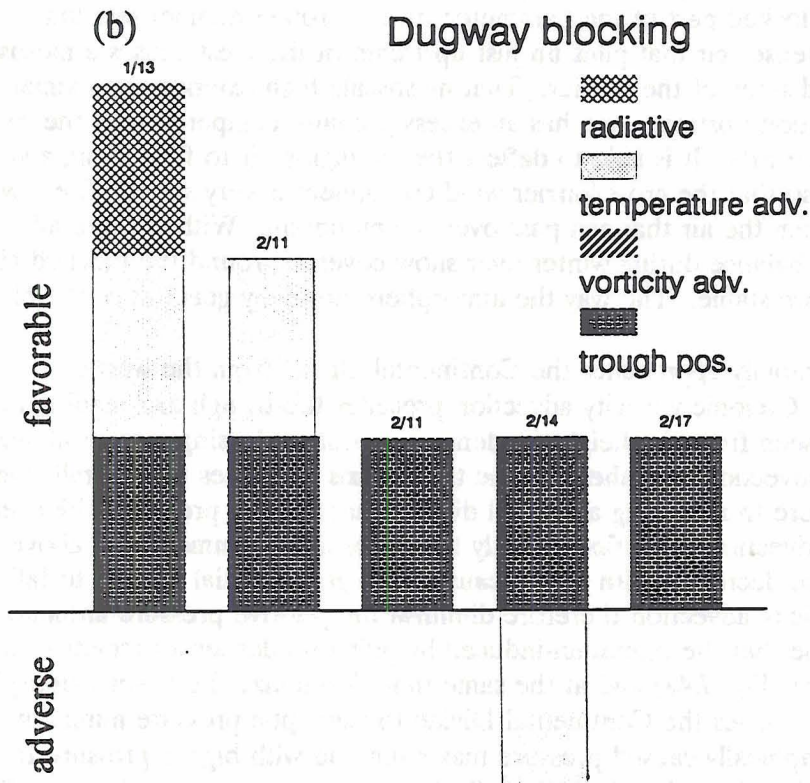






Fig. 7.3: Favorable conditions for blocking in (a) Tabernash and Meeker, and (b) in Dugway. A trough axis downstream of the barrier, anticyclonic vorticity advection, warm air advection and a negative net radiation balance can reinforce the mountain-induced mesoscale high (compare text). The dates above the bars are in months and days relative to LST.



 radiative
 temperature adv.
 vorticity adv.
 trough pos.

gradient associated with the position of the extrema in the 600 hPa height was the dominant force behind the blocking.

Vorticity advection during the transitions to blocking was negligible. Two cases had favorable temperature advection to provide a west-east directed component of the synoptic pressure gradient.

Blocking did not occur with a northerly component present but the small sample size prohibits conclusions about directional differences between blocking and unblocking.

Due to the great barrier depth nocturnal cooling could not cause nor assist in the transition from a blocked to an unblocked flow.

7.4 Conceptual model of blocking evolution

The results of the previous section can be condensed into two prototypes of blocking evolution.

7.4.1 Synoptically driven blocking evolution

The preferred way of the atmosphere to become blocked and unblocked during low-sun season and for high barriers is through synoptic systems (section 7.3).

a) unblocking

During winter the cross-barrier component of the wind above the Rocky Mountains in Colorado is usually small enough and the stability strong enough to put the atmosphere into the blocked part of the parameter space (Froude number less than approximately 2/3). Denser air that piles up just upstream of the crest causes a mesoscale high above the upwind slope of the barrier. That mesoscale high extends approximately one radius of deformation upstream and has an excess pressure compared with the region farther upstream of one hPa. It is able to deflect the impinging air to flow along and around the mountain so that the cross-barrier wind component is very small. The low-level flow separates from the air that can pass over the mountain. With the overall negative net radiation balance during winter over snow covered ground the blocked air cools and becomes more stable. The way the atmosphere normally gets out of the blocked state is as follows:

A short wave rapidly approaches the Continental Divide from the west or northwest (Fig. 7.4b). Cyclonic vorticity advection precedes the trough axis leading to height falls as can be seen from the height tendency equation and rising motion above the mountains. Cold air advection also ahead of the trough axis decreases the overall stability of the lower troposphere thus making a vertical displacement of the previously blocked air easier. The cold air advection is confined mostly to a layer at and immediately above the mountaintop and hence decreases with height causing the geopotential heights to fall. Temperature and vorticity advection therefore diminish the positive pressure anomaly above the upwind slope that the mountain-induced by piling up denser air (relative to farther upstream) there (Fig. 7.4a) and at the same time destabilize the lower troposphere. When the trough axis reaches the Continental Divide the synoptic pressure minimum overwhelms the orographically caused pressure maximum and with higher pressure farther upstream in the following ridge the blocked air flushes out over the mountains (Fig. 7.4c).

Winds pick up in the lower levels to a cross-barrier speed similar to the flow above the mountains. Vertical mixing decreases the stability of the previously blocked air. A short wave unblocks more likely than a wide trough because vorticity advection increases as the wavelength of a disturbance decreases and the pressure minimum at the trough axis extends over a horizontal distance comparable to the one of the mountain-induced mesoscale high.

b) blocking

As the trough moves farther east towards the Great Plains anticyclonic vorticity advection and warm air advection appear upstream of the Continental Divide (Fig. 7.4d). Anticyclonic vorticity advection causes the geopotential height to rise and also brings potentially warmer air down from the mid- and upper troposphere thus increasing the overall stability of the lower atmosphere which makes a vertical displacement of an air parcel more difficult. Warm air advection does the same and since it usually decreases with height it also contributes to the geopotential height rise. This time the synoptic forcings work together with the orographic forcing in building the positive pressure anomaly above the upwind slope of the Continental Divide. As the height maximum of the flow aloft (ridge axis) approaches the barrier the air below the mountaintop becomes blocked again.

7.4.2 Radiatively driven blocking evolution

a) unblocking

Even if a synoptic high pressure system (ridge) reinforces the mountain-induced positive pressure anomaly the air near the ground can become coupled to the flow above mountaintop and thus unblock when at least one of the following conditions is fulfilled: the sensible heat flux is strong and directed from the ground to the air above or the barrier is shallow. Unblocking occurs then like this:

After sunrise the net radiation balance turns positive so that the sensible heat flux will be away from the ground (Fig. 7.5b). With snow on the ground the surface albedo is high and the radiation surplus small. Therefore little energy is available for the sensible heat flux and only a very shallow boundary layer forms. Unless the barrier itself is also very shallow the boundary layer will not reach high enough to reconnect to the flow above. Forested areas, however, have a lower albedo even with snow on the ground and more energy will be available for the growth of the boundary layer. With continuing solar insolation the nocturnal surface inversion decreases and finally - with sufficiently large sensible heat flux - gets destroyed. Now the boundary layer grows much faster and might come close to barrier top so that the winds from higher up can come down close to the ground - unblocking (Fig. 7.5c)! The barrier in Tabernash was low enough to make this unblocking mechanism work even during the time of minimum solar insolation. Towards the end of the observations, in February, an increase in solar insolation and the fact that not the whole surface was snow-covered provided a strong enough sensible heat flux to grow a boundary layer deep enough to unblock even at Meeker where the barrier is 700 m higher than in Tabernash.

b) blocking

Around sunset without solar insolation the net radiation balance is negative, the surface cools radiatively, the sensible heat flux will reverse direction and the air above the

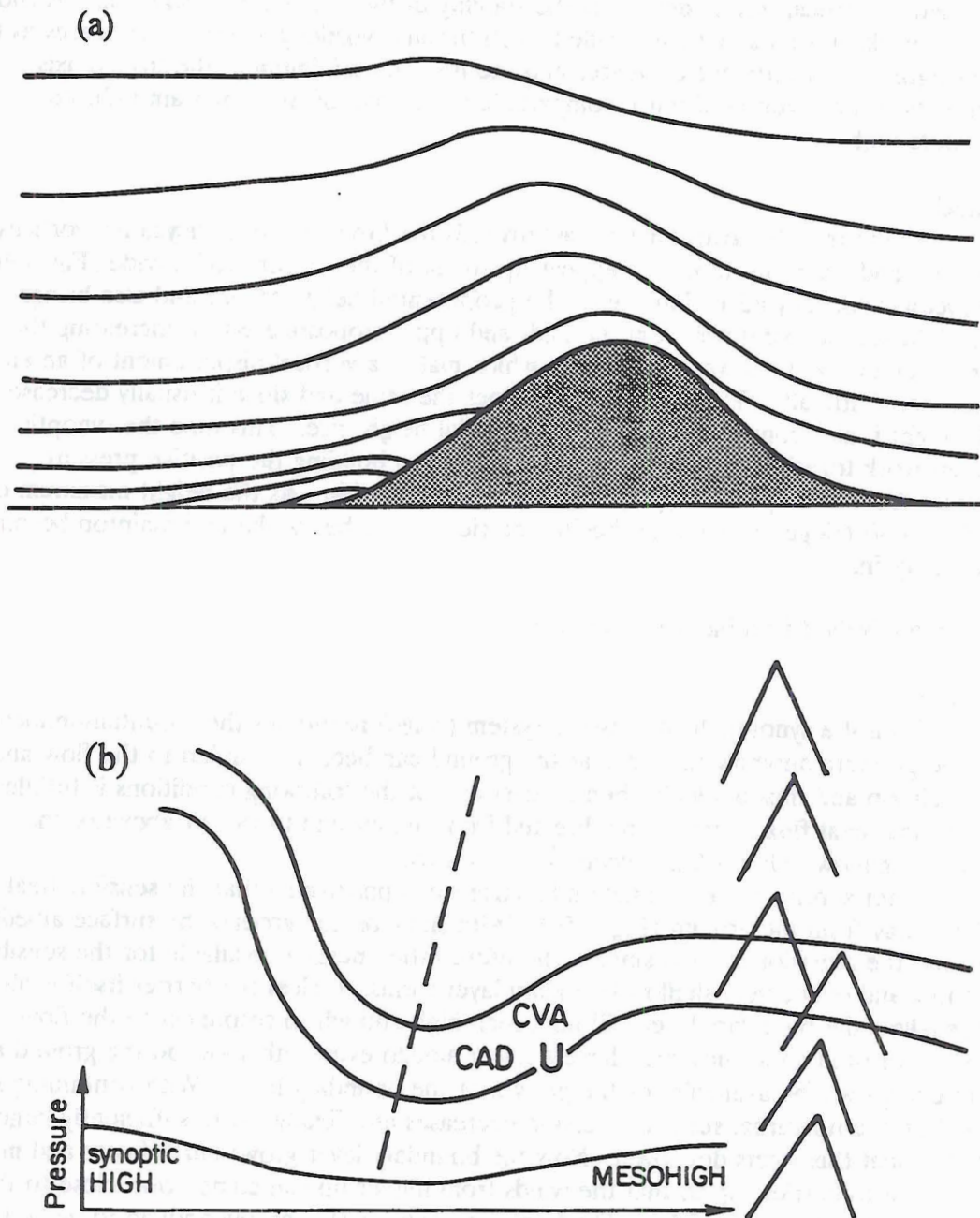


Fig. 7.4a,b: Conceptual model of synoptically driven blocking evolution: (a) isentropic cross section for the initially blocked state (note the air just upstream of the crest is denser than at the same elevation farther upstream). (b) Cyclonic vorticity advection (CVA) and cold air advection (CAD) ahead of an approaching short wave instigate pressure falls at the surface. The mountain-induced mesoscale high is weakened. Cross-section (perpendicular to barrier) of pressure at the surface is at the bottom.

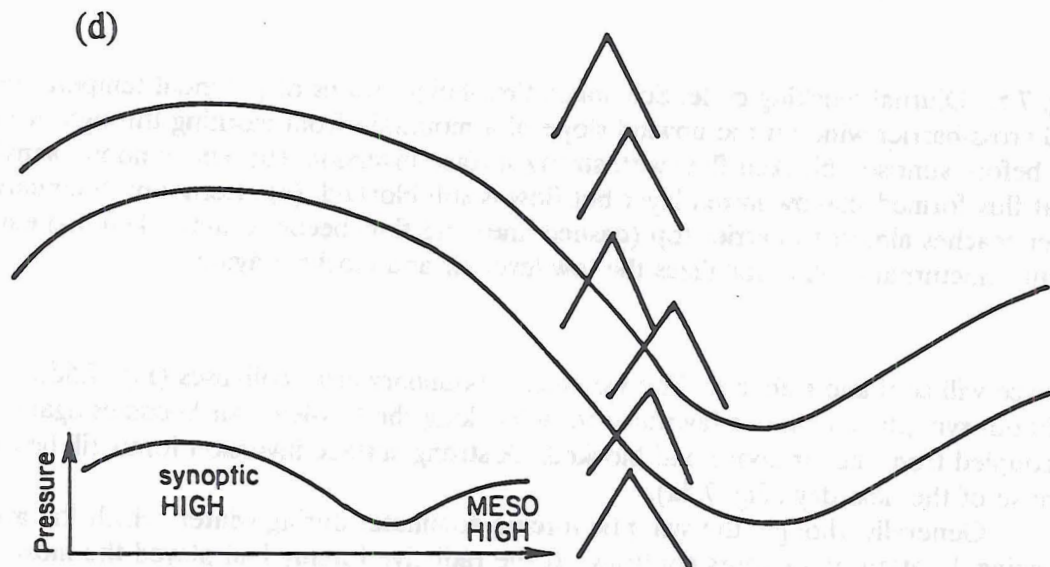
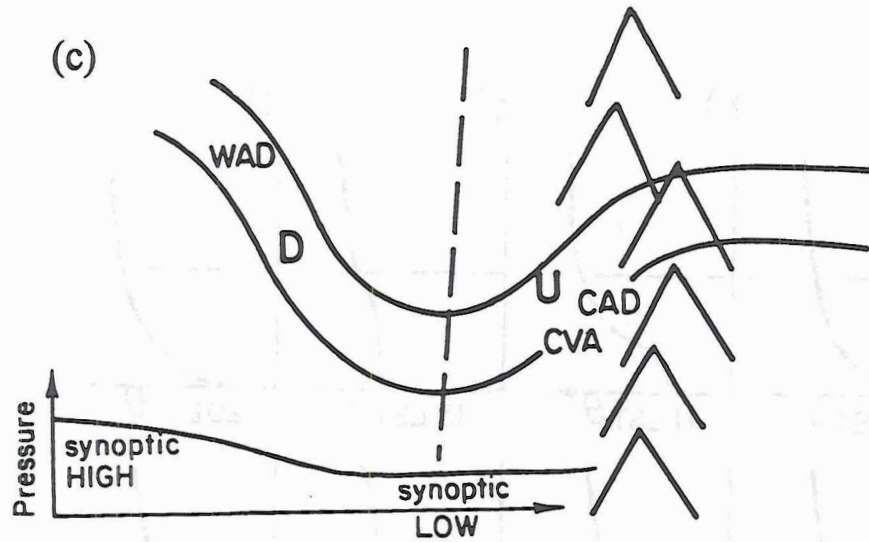


Fig. 7.4c,d: Conceptual model of synoptically driven blocking evolution: (c) Unblocking as the trough axis reaches the Continental Divide and overpowers the mountain-induced mesoscale high above the upwind slopes. (d) Re-blocking as a ridge moves over the Continental Divide. A cross-section (perpendicular to the barrier) of surface pressure is at the bottom of each graph.

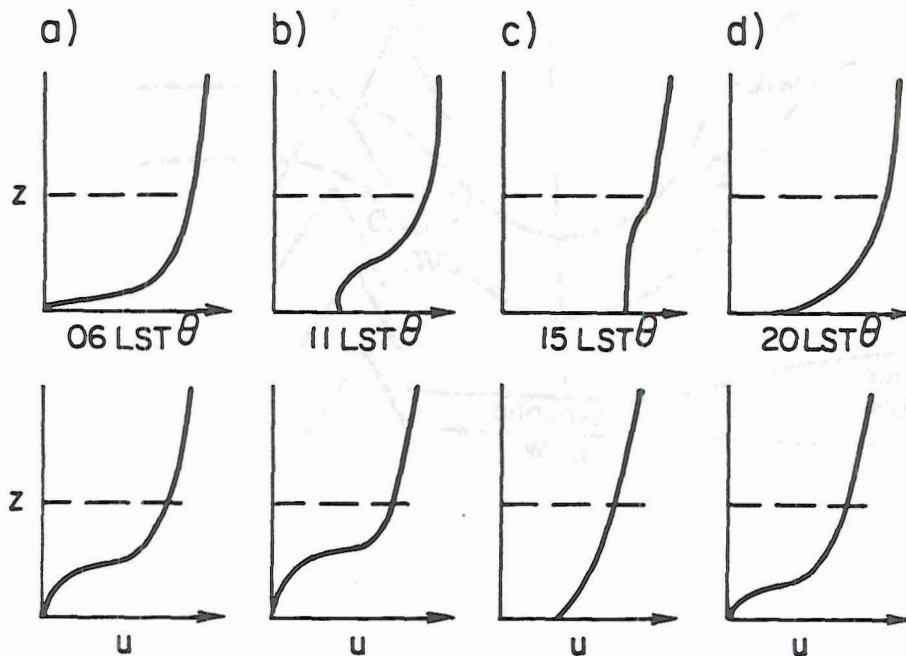


Fig. 7.5: Diurnal blocking cycle: Schematic time-height series of potential temperature and cross-barrier wind on the upwind slope of a mountain from morning through evening: (a) before sunrise: blocked flow with strong surface inversion, (b) before noon: sensible heat flux formed shallow mixed layer but flow is still blocked, (c) afternoon: boundary layer reaches almost to barrier top (dashed line) and flow becomes unblocked, (d) early night: nocturnal cooling stabilizes the low level air and blocks it again.

surface will cool and stabilize. The well-mixed boundary layer collapses (Fig. 7.5d). Without synoptic conditions favorable to unblocking the low-level air becomes again decoupled from the air above and blocked. A strong surface inversion forms till before sunrise of the next day (Fig. 7.5a).

Generally, though, the synoptic forcing dominates during winter, which the average blocking duration of 36 hours confirms. If the radiative forcing had played the most important role that time should have been around 12 hours instead.

8.1 Synoptically driven blocking evolution

On January 24, 1992, at 05 LST a weak short wave embedded into strong northwesterly flow was close to the Continental Divide. The rawinsonde network barely resolves the trough (Fig. 8.1a); the time-height series from the wind profilers (Figs 8.2 and 8.3) show it better.

At the same time cyclonic vorticity advection occurred just upstream of the Continental Divide still causing the height to fall and through its rising vertical motion field somewhat destabilizing the air. Farther upstream at the border between Colorado and Utah anticyclonic vorticity was advected causing isentropes to descend and heights to rise assisting in the reversal of the mountain-induced positive mesoscale pressure gradient. Cold air is advected upstream of the Continental Divide. The region where it decreased strongest with height (i.e. caused the strongest height rises) coincided with the area where anticyclonic vorticity was advected. While the pressure was still falling over the Continental Divide it was rising farther upstream thus eliminating the mountain-induced positive pressure anomaly. And indeed, the flow became unblocked in Tabernash (Fig. 8.2a,b) at 1258 LST and in Meeker at 1344 LST (Fig. 8.3). Fig. 8.2b captures the transition from a blocked to an unblocked state in Tabernash in detail: Initially the blocked layer extended to 3200 m ASL but at 1854 LST blocked air reached up to 3400 m ASL. Eleven minutes later that depth had decreased to 3100 m ASL and another 22 minutes later, at 1227 LST, the strong winds reached down to the first gate of the profiler (152 m AGL), which means that the transition from blocked to unblocked state took only half an hour!

Unlike Tabernash, where very weak winds from various directions marked the blocked period, SSW (i.e. along-barrier) winds of up to 5 m/s blew at the lowest two gates in Meeker (Fig. 8.3) before the wind turned more westerly and stronger at unblocking.

At the next observation time for the rawinsonde network at 17 LST the trough axis was just moving away from the Continental Divide (Fig. 8.1b). Vorticity advection upstream from it was very weak as was the temperature advection. Cold air, however, was advected over southern Colorado and destabilized the air below. This advection decreased strongly with height between 700 hPa and 600 hPa thus causing the geopotential heights to rise there. Both profiler sites showed the flow unblocked.

The trough moved eastward quickly so that 12 hours later the region upstream of the Continental Divide lay under a ridge (Fig. 8.1c). Vorticity advection there was insignificant but cold air was advected with the advection decreasing strongest with height just upstream of the Continental Divide thus adding to the mountain-induced positive pressure anomaly. Accordingly both profilers showed blocked conditions (Figs 8.2a and 8.3). Tabernash returned to being blocked at 02 LST on January 25, 1992 and Meeker at 2030 LST of the previous day. A close-up of the period during which the flow switched from unblocked to blocked in Tabernash (Fig. 8.2c) reveals that this transition took only approximately 20 minutes! The flow in the lowest 500 m AGL was southeasterly despite westerly winds above the mountains (flow reversal)! The low-level air in Meeker also flowed approximately opposite to the higher level winds with easterly flow of up to 4 m/s.

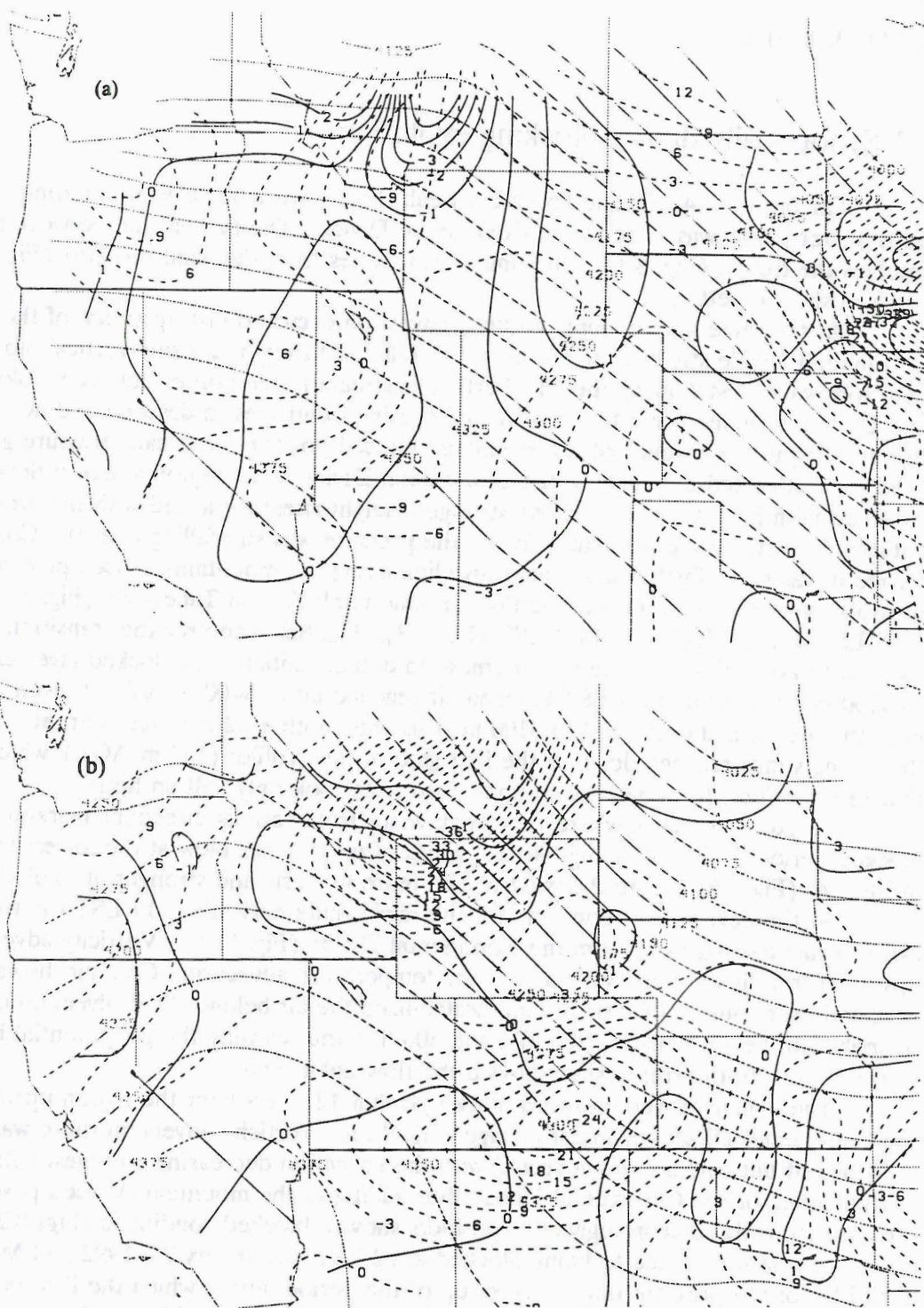


Fig. 8.1a,b: 600 hPa height (dotted) and advection of absolute vorticity (solid) and temperature (dashed) on (a) January 24, 1992, 05 LST, and (b) 17 LST. Contours are 10^{-9} s^{-2} for vorticity advection and 10^{-5} K/s for temperature advection.

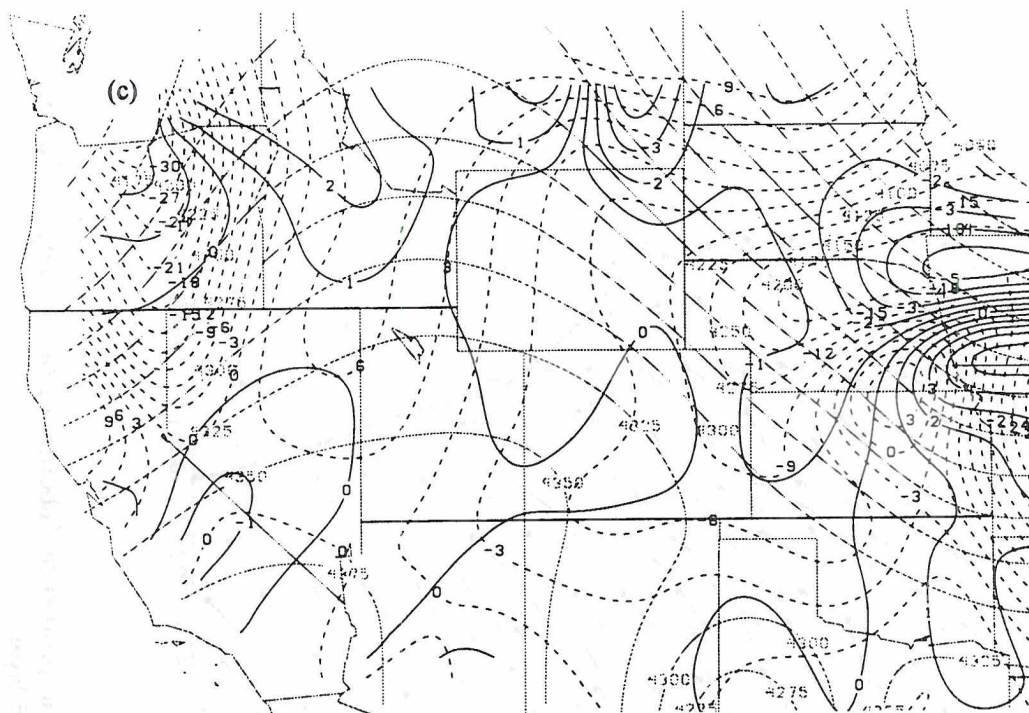


Fig. 8.1c: 600 hPa height (dotted) and advection of absolute vorticity (solid) and temperature (dashed) on January 25, 1992, 05 LST. Contours are 10^{-9} s^{-2} for vorticity advection and 10^{-5} K/s for temperature advection.

8.2 Radiatively driven blocking evolution

On January 28, 1992, synoptic conditions favored a blocking of the low-level air: the region upstream of the Continental Divide was under a ridge for the whole day (Fig. 8.4). The trough axis lay over Kansas. At 5 LST (Fig. 8.4a) anticyclonic vorticity was advected over Meeker and Tabernash. The temperature advection at 600 hPa was very small.

While Meeker was indeed blocked Tabernash was only initially. Fig. 8.5 shows that the layer up to 3400 m ASL was blocked until the early afternoon at 13 LST. Less than an hour later at 1357 LST the boundary layer had grown deep enough to mix the higher cross-barrier winds from above mountaintop down to the ground. Even though snow covered the ground on this day the many conifer trees in the area created a strong enough sensible heat flux to form a several hundred meter deep boundary layer thus connecting it to the air flowing over the Continental Divide. Although temperature soundings for that particular day to give an exact depth of the boundary layer are not available, the observation two weeks later during a special observation period of a boundary layer that grew under clear conditions to approximately 3800 m ASL (i.e. above the average barrier height!) supports this explanation.

At sunset around 17 LST the flow was still unblocked. An hour later, however, after the deep, well-mixed boundary layer had collapsed, the lowest layer up to 3000 m ASL became blocked again. The winds remained very weak and the last sounding in Fig. 8.5 at 21 LST even shows weak flow reversal: southeasterly flow in the blocked layer with

Tabernash January 24–25, 1992

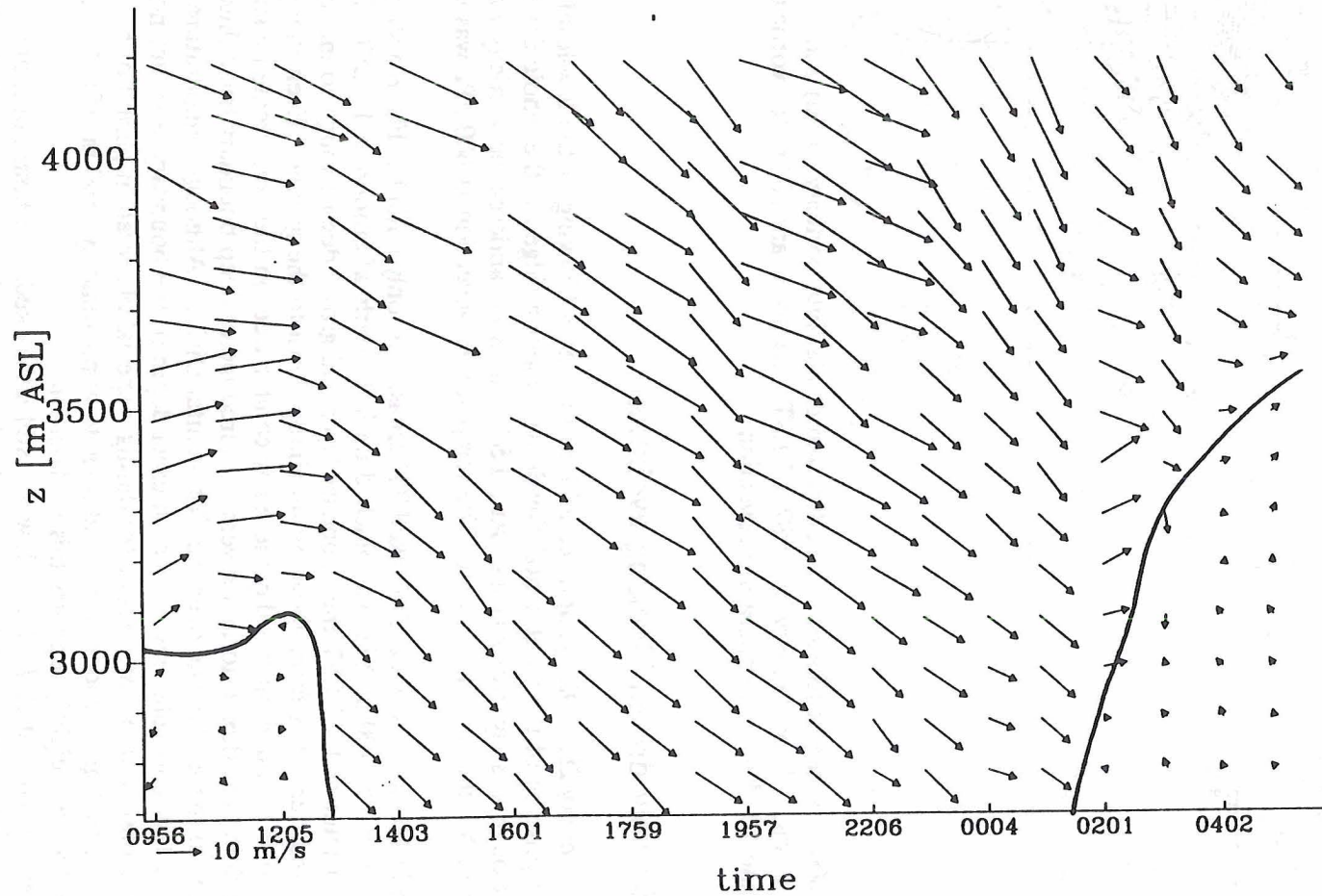


Fig. 8.2a: Horizontal wind vectors averaged over approximately 20 minutes from profiler in Tabernash from January 24, 12 LST through January 25, 1992, 0420 LST. A bold line marks the top of the blocked layer.

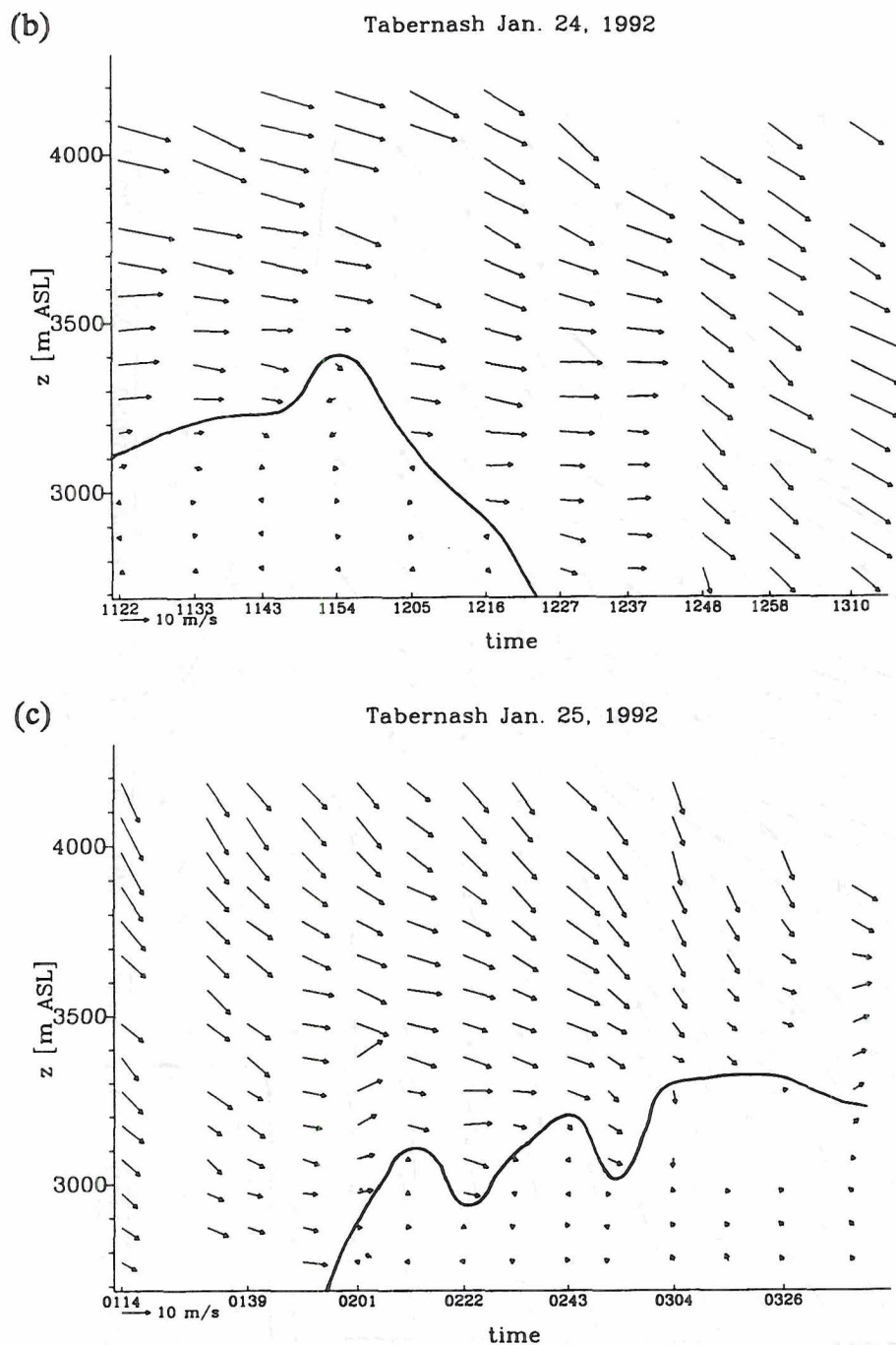


Fig. 8.2b,c: Winds every 10 minutes show details of the transition from (b) blocked to unblocked and (c) unblocked to blocked in Tabernash on January 24 and 25, respectively. Time is hours and minutes [LST]. A bold line marks the top of the blocked layer.

Meeker January 24-25, 1992

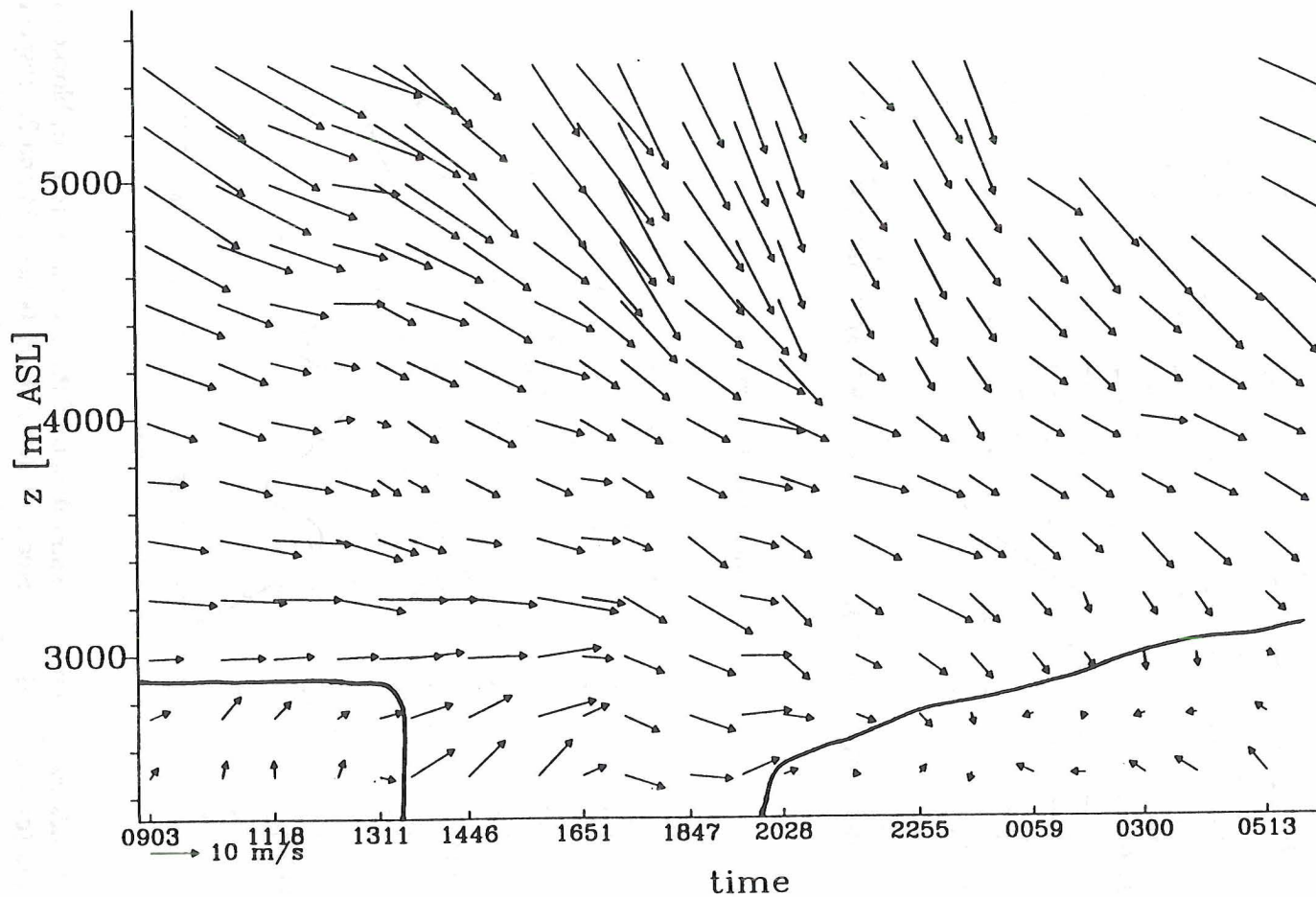


Fig. 8.3: Horizontal wind vectors averaged over approximately 30 minutes from profiler in Meeker from January 23, 1730 LST through January 25, 1992, 0230 LST. A bold line marks the top of the blocked layer.

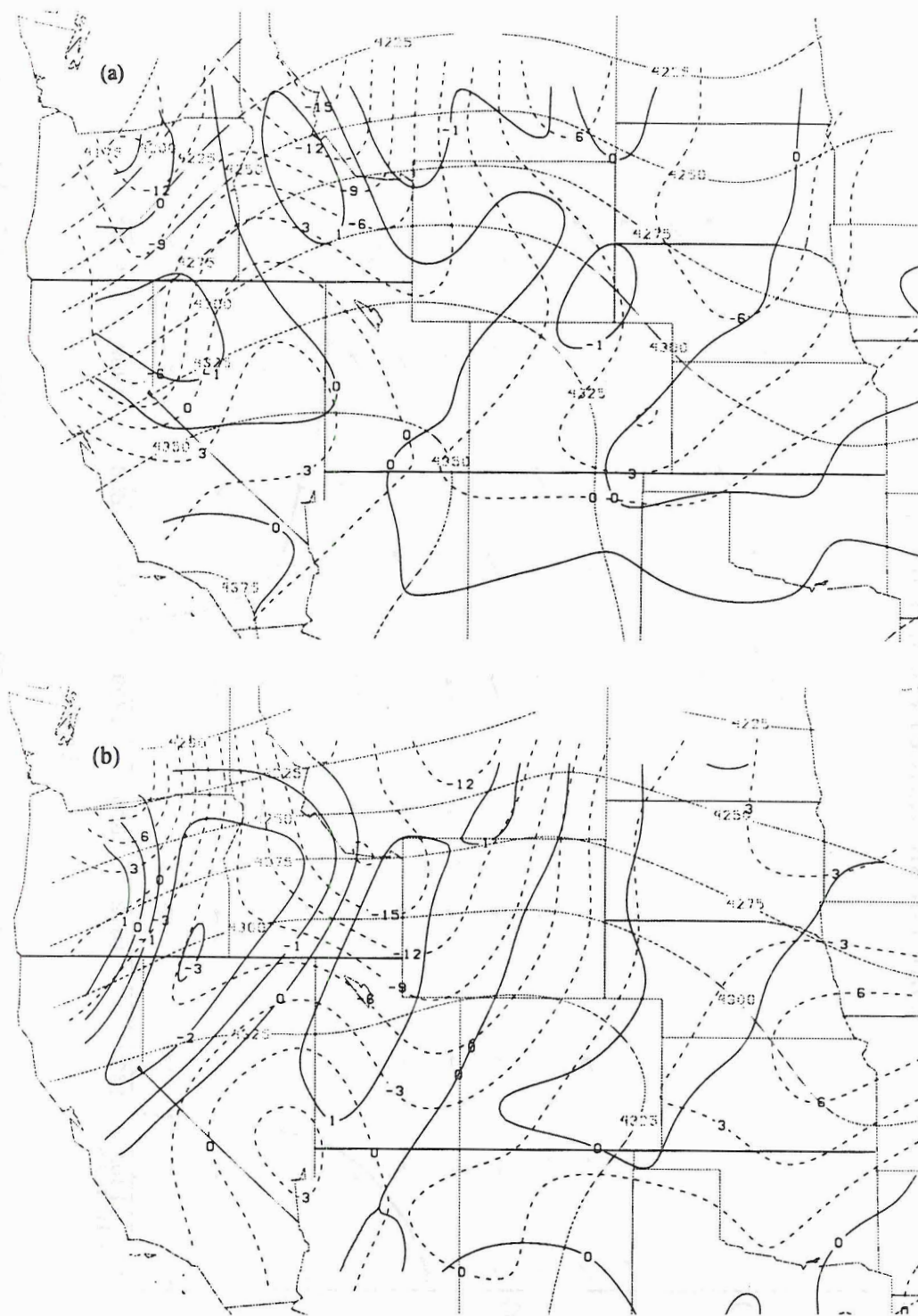


Fig. 8.4: Height (dense dots), advection of absolute vorticity (solid) and temperature (dashed) at 600 hPa on January 28, 1992. Contours are 10^{-9} s^{-2} for vorticity advection and 10^5 K/s for temperature advection. (a) 05 LST, and (b) 17 MST January 29, 1992.

Tabernash January 28, 1992 [LST]

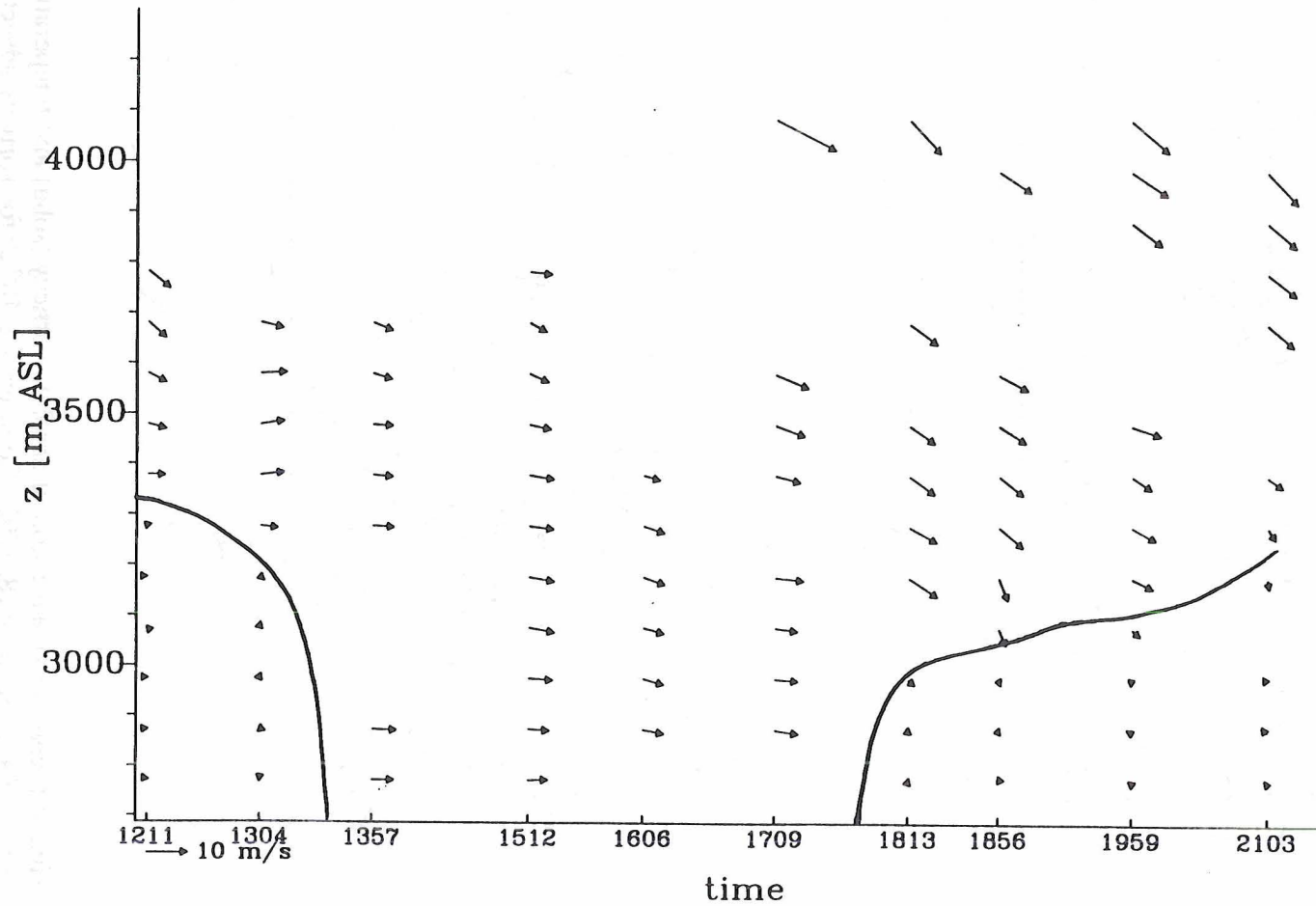


Fig. 8.5: Wind vectors from the NOAA profiler in Tabernash on January 28, 1992, from 12 MST through 21 MST. Local time (MST) is 7 hours behind UTC. A bold line marks the top of the blocked layer.

northwesterly winds above. The synoptic conditions had remained unchanged (Fig. 8.4b):
Tabernash stayed under a ridge with very weak vorticity and temperature advections at
600 hPa.

9.1 Conclusions

The evolution of low-level flow upstream of the Continental Divide and the Wasatch Range in the Rocky Mountains from being blocked, i.e. unable to surmount the barrier, to becoming unblocked and blocked again was studied observationally and numerically. During two months in the winter of 1991/92 a transect of three wind profilers measured the wind field every few minutes. Frequent radiosonde launches during three special observation periods supplemented these measurements. Three-dimensional numerical simulations with the Colorado State Regional Atmospheric Modeling System (RAMS) using realistic topography augmented the observations with details of the blocked and unblocked flow.

The results confirm the theory that a mountain-induced mesoscale high above the upwind slopes causes the blocking. While previous research of idealized situations focused on changes of the cross-barrier wind component and stability as determining variables to build that mesoscale high, this study found different mechanisms at work in the real atmosphere.

Synoptic and radiative forcings instead of changes in stability and cross-barrier wind speed controlled the transitions between blocked and unblocked flow states. The prototypical synoptic forcing is as follows:

When the low-level flow is blocked by the mountain-induced mesoscale high a synoptic cross-barrier pressure gradient can negate the mesoscale gradient if it points in the opposite direction and has a comparable magnitude. The mesoscale high exceeds the pressure farther upstream by approximately one hPa and extends up to one radius of deformation from the barrier. Unblocking happens most frequently when the trough axis of a short wave is immediately upstream of the barrier, but synoptic cross-barrier pressure gradients caused by contrasts in vorticity and temperature advection on occasions are also strong enough to overpower the mesoscale pressure gradient. The flow returns to its blocked state when the ridge behind the trough approaches the barrier so that the synoptic cross-barrier pressure gradient reinforces the mesoscale one.

The radiative forcing works for low barriers or with strong solar insolation:

Under these conditions a well-mixed boundary layer can grow almost to the height of the barrier by afternoon and reconnect the blocked layer with the higher winds above the barrier and thus unblock it. Around sunset the net radiation balance turns negative, the sensible heat flux reverses, and the radiatively forced cooling stabilizes the lower atmosphere again and the transition back to blocked occurs.

The transition between the two states happened rapidly on the order of an hour with a minimum of 20 minutes and a maximum of four hours. No previous observations with such a high temporal resolution had been available to capture the transition periods. A blocked flow event lasted on the average one and a half days but the duration varied widely from a few hours to eight days. The depth of the blocked layer even during one

blocking episode fluctuated considerably. It extended on the average up to between one half and two thirds of the barrier height and never exceeded the height of the barrier.

Numerical simulations confirmed that the Coriolis force limits the upstream extent of the layer deflected around the barrier to about one radius of deformation. The profiler farthest away from a barrier at approximately one radius of deformation actually observed the least amount of blocking. With a westerly wind above mountain top the low-level flow was blocked between 50% and 85% of the time depending on the location of the profiler.

The flow in the numerical simulations was deflected northward and channeled with high speeds through a gap in southern Wyoming, which is known as one of the windiest places in the United States.

9.2 Future research

Answers always seem to lead to new questions. After the completion of this study, several avenues need further exploration:

- a) Include radiative and surface fluxes in the numerical simulations to study the diurnally forced blocking cycle in more detail, especially the coupling between the boundary layer and air above.
- b) Numerically simulate an observed synoptically forced blocking cycle to provide a more complete picture of the flow field.
- c) Compile a climatology of blocked periods in the Great Basin area using the bidaily standard rawinsondings and the vertical cross-barrier component of kinetic energy method to determine blocking depths.
- d) Evaluate accuracy of various local blocking determination methods with trajectories generated from numerical simulations.
- e) Compare the blocking evolution by the Rocky Mountains with the one by the Alps.
- f) Investigate the connection between flow upstream of the barrier that had become unblocked as a short wave moved over that area and downslope windstorms on the lee side that can occur after that short wave moved to the downwind side of the barrier.

Appendix A: Launch times and highest pressure reached for the special observations periods in Tabernash and Meeker.

Table A1: Special observation periods in Tabernash

SOP 1			SOP 2			SOP 3		
date	time [LST]	lowest pressure [hPa]	date	time [LST]	lowest pressure [hPa]	date	time [UTC]	lowest pressure [hPa]
2/8	10:20	330	2/10	16:40	296	2/20	17:45	179
2/8	15:42	371	2/10	18:45	321	2/20	21:15	218
2/8	16:20	300	2/11	08:15	426	2/21	07:00	184
2/8	18:15	296	2/11	11:00	220	2/21	09:00	181
2/8	21:00	495	2/11	15:00	227	2/21	12:45	207
2/9	07:00	221	2/11	19:00	418	2/21	15:00	229
			2/11	22:00	270	2/21	17:30	170
			2/12	07:15	224			

Table A2: Special observation periods in Meeker

SOP 1			SOP 2			SOP 3		
date	time [LST]	lowest pressure [hPa]	date	time [LST]	lowest pressure [hPa]	date	time [LST]	lowest pressure [hPa]
2/8	07:32	102	2/10	10:00	169	2/20	17:27	452
2/8	09:17	168	2/10	11:07	188	2/20	21:15	234
2/8	13:31	148	2/10	16:36	157	2/21	07:03	257
2/8	15:37	141	2/10	21:05	249	2/21	09:05	249
2/8	18:35	171	2/11	08:06	176	2/21	13:08	386
2/8	21:08	272	2/11	11:02	168	2/21	14:56	331
2/9	08:51	198	2/11	15:01	171	2/21	17:30	299
			2/11	19:15	171			
			2/11	22:07	177			
			2/12	07:13	163			

References:

- Achtemeier, G.L., 1987: On the concept of varying influence radii for a successive corrections objective analysis. *Mon. Wea. Rev.*, **115**, 1760-1771.
- Bacmeister, J.T., and R.T. Pierrehumbert, 1988: On high-drag states of nonlinear stratified flow over an obstacle. *J. Atmos. Sci.*, **45**, 63-80.
- Bacmeister, J.T., M.R. Schoeberl, L.R. Lait, and P.A. Newman, 1990: ER-2 mountain wave encounter over Antarctica: evidence for blocking. *Geophys. Res. Lett.*, **17**, 81-84.
- Bader, D.C., and T.B. McKee, 1992: Mesoscale boundary-layer evolution over complex terrain. Part II: Factors controlling nocturnal boundary-layer structure. *Mon. Wea. Rev.*, **120**, 802-816.
- Baines, P.G., 1979: Observations of stratified flow past three-dimensional barriers. *J. Geophys. Res.*, **84**, 7834-7838.
- Baines, P.G., and K.P. Hoinka, 1985: Stratified flow over two-dimensional topography in fluid of infinite depth: A laboratory simulation. *J. Atmos. Sci.*, **42**, 1614-1630.
- Baines, P.G., 1987: Upstream blocking and airflow over mountains. *Ann. Rev. Fluid Mech.*, **19**, 75-97.
- Bell, G.D., and L.F. Bosart, 1988: Appalachian cold-air damming. *Mon. Wea. Rev.*, **116**, 137-161.
- Betts, A.K., 1982: Saturation point analysis of moist convective overturning. *J. Atmos. Sci.*, **39**, 1484-1505.
- Betts, A.K., and B.A. Albrecht, 1987: Conserved variable analysis of the convective boundary layer thermodynamic structure over the tropical oceans. *J. Atmos. Sci.*, **44**, 83-99.
- Binder, P., H.C. Davies, and J. Horn, 1989: Free atmosphere kinematics above the northern Alpine foreland during the ALPEX SOP. *Contrib. Atmos. Phys.*, **62**, 30-45.
- Bluestein, H.B., 1993: *Synoptic-dynamic meteorology in midlatitudes. Volume 2.* Oxford University Press, 594 pp.
- Bossert, J., 1990: Regional-scale flows in complex terrain: an observational and numerical investigation. *CSU Atmos. Sci. Paper # 472*, 254 pp.
- Brewster, K.A., 1989: *Profiler training manual #2: Quality control of wind profiler data.* Program for Regional Observing and Forecasting Services (PROFS), Boulder, 39 pp.

- Carlson, T.N., 1991: *Midlatitude weather systems*. HarperCollins, 507 pp.
- Castro, I.P., W.H. Snyder, and G.L. Marsh, 1983: Stratified flow over three-dimensional ridges. *J. Fluid Mech.*, **135**, 261-282.
- Cehak, K., and H. Pichler, 1968: Beschreibung des Stromfeldes im Alpenbereich mittels Windmatrizen. *Arch. Met. Geoph. Biokl.*, **17A**, 61-77.
- Chen, W., and R.B. Smith, 1987: Blocking and deflection of airflow by the Alps. *Mon. Wea. Rev.*, **115**, 2578-2597.
- Collins, W.C., and L.S. Gandin, 1990: Comprehensive quality control at the National Meteorological Center. *Mon. Wea. Rev.*, **118**, 2752-2768.
- Daley, R., 1991: *Atmospheric Data Analysis*. Cambridge University Press, Cambridge, 457 pp.
- Ecklund, W.L., D.A. Carter, B.B. Balsley, P.E. Currier, and J.L. Green, 1990: Field tests of a lower tropospheric wind profiler. *Radio Sci.*, **25**, 899-906.
- Fairall, C.W., 1991: The humidity and temperature sensitivity of clear-air radars in the convective boundary layer. *J. Appl. Meteor.*, **30**, 1064-1074.
- Fischler, M.A., and R.C. Bolles, 1981: Random sample consensus: a paradigm for model fitting with applications to image analysis and automated cartography. *Commun. ACM*, **24**, 381-395.
- Furger, M., 1992: The radiosoundings of Payerne: aspects of the synoptic-dynamic climatology of the wind field near mountain ranges. *Theor. Appl. Climatol.*, **45**, 3-17.
- Hayden, C.M., and R.J. Purser, 1988: Three-dimensional recursive filter objective analysis of meteorological fields. *Preprints 8th Conference on Numerical Weather Prediction*, Baltimore, MD, Feb. 20-26, AMS, Boston, Mass., 185-190.
- Hoskins, B.J., I. Draghici, and H.C. Davies, 1978: A new look at the ω -equation. *Quart. J. Roy. Meteor. Soc.*, **104**, 31-38.
- Helfand, H.M., and J.C. Labraga, 1988: Design of nonsingular level 2.5 second-order closure model for the prediction of atmospheric turbulence. *J. Atmos. Sci.*, **43**, 113-132.
- Kropfli, R.A., I. Katz, T.G. Konrad, and E.B. Dobson, 1968: Simultaneous radar reflectivity measurements and refractive index spectra in the clear atmosphere. *Radio Sci.*, **3**, 991-994.
- Lackmann, G.M., and J.E. Overland, 1989: Atmospheric structure and momentum balance during a gap wind event in Shelikof Strait, Alaska. *Mon. Wea. Rev.*, **117**, 1817-1833.

- Lee, T.J., R.A. Pielke, R.C. Kessler, J. Weaver, 1989: Influence of cold pools downstream of mountain barriers on downslope winds and flushing. *Mon. Wea. Rev.*, **117**, 2041-2058.
- Martner, B.E., 1986: *Wyoming Climate Atlas*. University of Nebraska Press, Lincoln, 432 pp.
- Marwitz, J., and J. Toth, 1993: The Front Range blizzard of 1990: Part I: Synoptic and mesoscale structure. *Mon. Wea. Rev.*, **121**, 402-415.
- Mass, C.F., and G.K. Ferber, 1990: Surface pressure perturbations produced by an isolated mesoscale topographic barrier. Part I: General characteristics and dynamics. *Mon. Wea. Rev.*, **118**, 2579-2796.
- Mayr, G.J., and T.B. McKee, 1990: Flow blocking in the Rockies. *Preprints 5th Conf. Mountain Meteorology*, Boulder, CO. American Meteorological Society, Boston. 39-41.
- Mesinger, F., Z.I. Janjic, S. Nickovic, D. Gavrilov, and D.G. Deaven, 1988: The step-mountain coordinate: model description and performance for cases of Alpine lee cyclogenesis and for a case of Appalachian redevelopment. *Mon. Wea. Rev.*, **116**, 1493-1518.
- Nastrom, G.D., K.S. Gage, and W.L. Ecklund, 1990: Uncertainties in estimates of the mean vertical velocity from MST radar observations. *Radio Sci.*, **25**, 933-940.
- Nathanson, F.E., 1991: *Radar design principles*. McGraw-Hill, New York, 720 pp.
- Parish, T.R., 1981: Barrier winds along the Sierra Nevada Mountains. *J. Appl. Meteor.*, **21**, 925-930.
- Peppler, W., 1928: Nördliche Winde und Stauwirkungen über dem Alpenvorland. *Beitr. Phys. d. freien Atmos.*, **14**, 138-146.
- Pielke, R.A., W.R. Cotton, R.L. Walko, C.J. Tremback, M.E. Nicholls, M.D. Moran, D.A. Wesley, T.J. Lee, and J.H. Copeland, 1992: A comprehensive meteorological modeling system - RAMS. *Meteor. Atmos. Phys.* (accepted for publication).
- Pierrehumbert, R.T., 1985: Stratified semigeostrophic flow over two-dimensional topography in an unbounded atmosphere. *J. Atmos. Sci.*, **42**, 523-526.
- Pierrehumbert, R.T., and B. Wyman, 1985: Upstream effects of mesoscale mountains. *J. Atmos. Sci.*, **42**, 977-1003.
- Richter, J.H., 1969: High-resolution tropospheric radar sounding. *Radio Sci.*, **4**, 1261-1268.
- Rogers, R.R., and M.K. Yau, 1989: *A short course in cloud physics*. Pergamon Press, Oxford, 293 pp.

- Rolph, G.D., and R.R. Draxler, 1990: Sensitivity of three-dimensional trajectories to the spatial and temporal densities of the wind field. *J. Appl. Meteor.*, **29**, 1043-1054.
- Rousseeuw, P.J., and A.M. Leroy, 1987: *Robust regression and outlier detection*. John Wiley & Sons, New York, 329 pp.
- Schwerdtfeger, W., 1988: The effect of the Antarctic Peninsula on the temperature regime of the Weddell Sea. *Mon. Wea. Rev.*, **103**, 45-51.
- Sheppard, P.A., 1956: Airflow over mountains. *Quart. J. Roy. Meteor. Soc.*, **82**, 528-529.
- Smith, R.B., 1985: On severe downslope winds. *J. Atmos. Sci.*, **42**, 2597-2603.
- Smith, R.B., 1988: Linear theory of stratified flow past an isolated mountain in isosteric coordinates. *J. Atmos. Sci.*, **45**, 3889-3896.
- Smith, R.B., 1989a: Hydrostatic airflow over mountains. *Advances in Geophys.*, **31**, 1-42.
- Smith, R.B., 1989b: Mountain-induced stagnation points in hydrostatic flow. *Tellus*, **41A**, 270-274.
- Smolarkiewicz, P.K., and R. Rotunno, 1990: Low Froude number flow past three-dimensional obstacles. Part II: Upwind flow reversal zone. *J. Atmos. Sci.*, **47**, 1498-1511.
- Snyder, W.H., R.S. Thompson, R.E. Eskridge, R.E. Lawson, I.P. Castro, J.T. Lee, J.C. Hurt, and Y. Ogawa, 1985: The structure of strongly stratified flow over hills: dividing streamline concept. *J. Fluid Mech.*, **152**, 249-288.
- Steinacker, R., 1984: The isentropic vorticity and the flow over and around the Alps. *Riv. Meteor. Aeronaut.*, **44**, 79-83.
- Stull, R.B., 1988: *An Introduction to Boundary Layer Meteorology*. Kluwer Academic Publishers, Dordrecht, 666 pp.
- Strauch, R.G., B.L. Weber, A.S. Frisch, C.G. Little, D.A. Merritt, and D.C. Welsh, 1987: The precision and relative accuracy of profiler wind measurements. *J. Atmos. Oceanic Technol.*, **4**, 563-571.
- Wesley, D.A., 1991: *An investigation of the effects of topography on Colorado Front Range winter storms*. Atmospheric Science Paper No. 489, Colorado State University, Fort Collins, 197 pp.
- Whiteman, C.D., and J.C. Doran, 1993: On the relationship between overlying synoptic-scale flows and winds within a valley. *J. Appl. Meteor.* (accepted).

Winston, H.A., D. Eagles, and C. Hayenga, 1990: High temporal resolution, real-time data processing and display capability for clear air Doppler wind profiling radars. *Vaisala News*, 121, 12-16.

Woodman, R.F., and A. Guillen, 1974: Radar observations of wind and turbulence in the stratosphere and mesosphere. *J. Atmos. Sci.*, 31, 493-505.

Wuertz, D.B., B.L. Weber, R.G. Strauch, A.S. Frisch, C.G. Little, D.A. Merritt, K.P. Moran, and D.C. Welsh, 1988: Effects of precipitation on UHF wind profiler measurements. *J. Atmos. Oceanic Technol.*, 5, 450-465.

Xu, Q., 1990: A theoretical study of cold air damming. *J. Atmos. Sci.*, 47, 2969-2985.

